MRI CHARACTERIZATION OF BROWN ADIPOSE TISSUE IN ADULT HUMANS WITH VALIDATION BY PET-CT

By

Aliya Gifford

Dissertation

Submitted to the Faculty of the

Graduate School of Vanderbilt University

in partial fulfillment of the requirements

for the degree of

DOCTOR OF PHILOSOPHY

in

Chemical and Physical Biology

May, 2016

Nashville, Tennessee

Approved:

E. Brian Welch, Ph.D.

Malcolm J. Avison, Ph.D.

Bruce M. Damon, Ph.D.

Seth A. Smith, Ph.D.

Alan D. Cherrington, Ph.D.

DEDICATION

To my family, by blood and by choice

ACKNOWLEDGEMENTS

To begin, this work would not be possible without the support from the following multiple funding sources: pilot funding from the Vanderbilt Institute for Obesity and Metabolism, a grant from the Vanderbilt Institute for Clinical and Translational Research: NCATS/NIH UL1 RR024975, as well as the following grants from the National Institutes of Health: UL1 TR000445 from NCATS/NIH, & R21DK096282 from NIDDK/NIH, & R25CA136440 from NCI/NIH, & T32EB014841 from NIBIB/NIH, & R01 DK105371 from NIDDK/NIH.

I would like to thank all the women and men who volunteered to participate in this study. Without their time and willingness to complete a difficult study, none of this would have been possible.

I am thankful to the many people at the Vanderbilt University Institute of Imaging Science (VUIIS) with whom I have had the pleasure of working during these past years. I especially thank my advisor Professor E. Brian Welch for being an excellent tutor, and for his unending patience and encouragement. I could not have asked for a more knowledgeable, supportive, or approachable mentor. I would also like to thank all my dissertation committee members, Professors Calum Avison, Bruce Damon, and Alan Cherrington for their support, helpful critiques, and informative conversations. I am particularly grateful to my committee member Professor Seth Smith for his individualized tutoring and for pushing me to overcome my own limitations.

Thanks goes also to my colleagues and office mates for their technical and moral support. Thanks especially to Pooja and Brendan for accompanying me on numerous coffee runs, filling the daily tank with fuel and great ideas.

Finally, a special word of appreciation goes to my family: my mother and father for believing in me and for always supporting my decisions; to my brother Hameed, thanks for being the best "little" brother ever; to my Grandpa Ernst for always encouraging me to pursue my dreams I'll be forever grateful to you. To my friends by chance, sisters by choice: Maryam, Hana and Amina, you mean the world to me. Last, but most certainly not least, I am especially grateful to my partner, Weston, for your unwavering love and encouragement through everything. You are an inspiration to me to always do my best, never settle, and to keep exploring and learning, always. Thank you for being by my side.

"There is a theory which states that if ever anyone discovers exactly what the Universe is for and why it is here, it will instantly disappear and be replaced by something even more bizarre and inexplicable. There is another theory which states that this has already happened."

~Douglas Adams,
The Hitchhiker's Guide to the Galaxy

TABLE OF CONTENTS

DEDICATION ..... **ii**
ACKNOWLEDGEMENTS ..... **iii**
LIST OF TABLES ..... **viii**
LIST OF FIGURES ..... **ix**
LIST OF ABBREVIATIONS ..... **xii**

PREFACE **1**

CHAPTER 1

INTRODUCTION **3**
1.1 MOTIVATION AND SPECIFIC AIMS 3
1.2 EXPLORING ADIPOSE TISSUE 5
1.2.1 Physical Characteristics of WAT and BAT 5
1.2.2 Cell Lineage 8
1.2.3 BAT Thermogenesis 10
1.2.4 Endocrine Function and Hormonal Signaling 14
1.3 BAT IN HUMANS 17
1.3.1 A Brief History 17
1.3.2 The Re-"Discovery" of BAT in Humans 19
1.3.3 Is FDG Indicative of Active BAT? 21
1.3.4 Is Human BAT Brown or Beige? 22
1.3.5 Prevalence and Significance of BAT in Adult Humans 23
1.3.6 Where Is the Field Now? 24
1.4 IMAGING METHODS USED IN THIS RESEARCH 27
1.4.1 Positron Emission Tomography 27
1.4.2 Computed Tomography 33
1.4.3 Magnetic Resonance Imaging 38
1.5 SUMMARY 54

CHAPTER 2

STUDY DESIGN **55**
2.1 SUBJECT ENROLLMENT 56
2.2 STUDY SET-UP 57
2.3 DATA ACQUISITION 59
2.3.1 PET-CT Acquisition 59
2.3.2 MRI Acquisition 60
2.4 IMAGE PROCESSING 63
2.4.1 MRI Fat-Water Separation Methods 63

2.4.2 Image Registration 68
2.5 SUMMARY 68

CHAPTER 3

WAT – SEGMENTATION AND MRI VERSUS CT CORRELATION 69
3.1 INTRODUCTION 69
3.2 MATERIALS AND METHODS 72
3.2.1 Subjects 72
3.2.2 Sequences Applied 72
3.2.3 Mask Generation Method 72
3.3 RESULTS 76
3.3.1 Intra-Modality Correlation 76
3.3.2 Inter-Modality Correlation 80
3.3.3 Testing Additional Fat-Water Separation Models 83
3.4 DISCUSSION 85
3.5 CONCLUSION 88

CHAPTER 4

BAT – SEGMENTATION AND CHARACTERIZATION 89
4.1 INTRODUCTION 89
4.2 SUBJECTS AND IMAGE ACQUISITION 91
4.3 BAT MASK GENERATION METHOD 93
4.4 RESULTS 97
4.4.1 Data Analysis 97
4.4.2 BAT Properties 98
4.4.3 BAT Compared to WAT 105
4.4.4 Clavicular Adipose Tissue in PET-Negative Subjects 106
4.5 DISCUSSION 107

CHAPTER 5

PROGRESS TOWARDS AUTOMATIC CLASSIFICATION 113
5.1 INTRODUCTION 113
5.2 SUBJECTS AND IMAGE ACQUISITION 113
5.3 RANDOM FOREST MACHINE LEARNING 114
5.3.1 Random Forest Algorithm 114
5.3.2 Training Data 115
5.4 RESULTS 116
5.4.1 Predictions 117
5.4.2 Anatomically Difficult Regions 118
5.5 CONCLUSION 121

CHAPTER 6

ADDITIONAL MRI PROPERTIES OF BAT 123
6.1 TRIGLYCERIDE MAPPING 123
6.1.1 Phantom and Subject Setup 125
6.1.2 Processing Methods 125
6.1.3 Initial Results 126
6.1.4 Discussion and Conclusion 130
6.2 TEMPERATURE MAPPING 131
6.2.1 Processing Methods 132
6.2.2 Initial Results 133
6.2.3 Results and Discussion 137

CHAPTER 7

CONCLUSION AND FUTURE WORK 138

REFERENCES 149

LIST OF TABLES

Table 1.2-1. Markers and characteristics of white, beige and brown adipocytes. 10

Table 1.3-1. Methods utilized in recent studies on human BAT 26

Table 1.4-1. SUV levels of healthy tissue measured by ^{18}F-FDG PET scans. 30

Table 1.4-2. Hounsfield Units of healthy tissue. 36

Table 2.1-1. Subject demographics. 57

Table 2.3-1. MRI Scan sequences acquired. 63

Table 2.4-1. Fat-spectral information for the 6- and 9-peak models. 65

Table 3.3-1. The slope and y-intercept values for WAT results. 83

Table 3.3-2. Parameters for three fat-water MRI separation models. 84

Table 4.2-1. PET-positive subject characteristics. 92

Table 5.3-1. Random forest data combinations. 115

Table 6.2-1. Results from the warm and cold FWMRI temperature maps. 136

Table 7-1. Imaging modalities for characterizing BAT 145

LIST OF FIGURES

Figure 1.2-1. Schematic of the typical morphology of white and brown adipocytes. 6

Figure 1.2-2. BAT depot locations in rodents, human infants, and adults. 7

Figure 1.2-3. Cell lineage of white, beige and brown adipocytes..... 9

Figure 1.2-4. Schematic of cold-induced thermogenesis in activated BAT 12

Figure 1.2-5. Brown adipose tissue endocrine signaling factors. 16

Figure 1.4-1. Positron Emission Tomography schematic. 28

Figure 1.4-2. Three factors influencing the resolution capability of PET imaging 31

Figure 1.4-3. Coronal PET maximum intensity projection images 33

Figure 1.4-4. Computed tomography imaging schematic. 34

Figure 1.4-5. Coronal CT slice through the head and abdomen of an adult. 37

Figure 1.4-6. MR properties of ^{1}H nuclei. 39

Figure 1.4-7. Application of RF pulse. 41

Figure 1.4-8. Longitudinal and transverse relaxation 42

Figure 1.4-9. Chemical shift in frequency of fat to water at 3 Tesla. 43

Figure 1.4-10. Magnetic Resonance fat-water separated coronal images of a Canine. 46

Figure 1.4-11. 9-peak fat spectrum model. 48

Figure 1.4-12. Coronal FSF and R_2* images 51

Figure 1.4-13. Frequency shift of water and fat..... 53

Figure 2.3-1. The “pillowcase” setup 60

Figure 2.3-2. MRI X-tend table setup. 61

Figure 2.4-1. Echo train interleaves. 64

Figure 2.4-2. FSF comparison images 67

Figure 3.2-1. Axial slices at the umbilicus level of two female subjects..... 75

Figure 3.3-1. Plots of cold vs. warm FSF 78

Figure 3.3-2. Plots of the cold vs. warm CT HU 79

Figure 3.3-3. Plot of CT HU vs. FSF for all 21 subjects 80

Figure 3.3-4. Plot of CT HU vs. FSF separated by BMI or temperature. 81

Figure 3.3-5. Plot of CT HU vs. FSF separated by both BMI and temperature. 82

Figure 3.3-6. CT HU vs. FSF for models A, B and C. 84

Figure 4.2-1. Flow chart of subject recruitment. 91

Figure 4.3-1. Coronal PET MIP..... 93

Figure 4.3-2. Flow charts showing the registration step. 94

Figure 4.3-3. Clavicular-level axial slices, post-registration. 95

Figure 4.3-4. Pictorial depiction of the rules used to generate a BAT mask. 96

Figure 4.4-1. Example images from thermoneutral and cold scans of a normal weight subject 100

Figure 4.4-2. Example images from thermoneutral and cold scans of an overweight subject ... 101

Figure 4.4-3. Clavicular level axial slices from cold scans of two subjects 102

Figure 4.4-4. Box and whisker plots of BAT values 104

Figure 4.4-5. Clavicular BAT volume versus age and BMI 105

Figure 4.4-6. Comparison of clavicular adipose tissue to umbilicus level WAT. 107

Figure 5.3-1. Random forest “BAT” and “not-BAT” training masks. 116

Figure 5.4-1. Plots of the mean precision at K. 118

Figure 5.4-2. Axial images and BAT probability maps in the neck of one subject. 119

Figure 5.4-3. Axial images and BAT probability maps in the chest of one subject. 121

Figure 6.1-1. Triglyceride representation. 124

Figure 6.1-2. Seven-oil phantom. 125

Figure 6.1-3. Results from the two-part fat-water separation processing. 126

Figure 6.1-4. Resulting fat signal fraction and triglyceride maps from the 7-oil phantom 127

Figure 6.1-5. MRI oil phantom results. 128

Figure 6.1-6. Clavicular level axial slice showing resulting triglyceride processing maps. 129

Figure 6.1-7. Human data plotted versus excised murine BAT and WAT tissue. 130

Figure 6.2-1. Automated FWMRI temperature-based mask creation. 133

Figure 6.2-2. Temperature mapping results from a PET-positive and PET-negative subject. ... 135

Figure 7-1. Three-axis plots: FSF v. R_2* v. ΔT.. 142

Figure 7-2. Mapping methods to characterize BAT. 143

Figure 7-3. Thermal Infrared (TIR) photos of two subjects. 147

LIST OF ABBREVIATIONS

^{18}F-FDG	Fluorine-18-labeled Fluorodeoxyglucose
^{1}H	Hydrogen
Acetyl-CoA	Acetyl coenzyme A
ADRB3	β_3-adrenergic receptors
ASC-1	Amino acid transporter
ASL	Arterial spin labeling
AT	Adipose tissue
ATP	Adenosine triphosphate
AUC	Area under the curve
B_0	Static main magnetic field
BAT	Brown adipose tissue
BMI	Body mass index
BOLD	Blood oxygenation level dependent
CA	Cold-activated
cAMP	Cyclic adenosine monophosphate
CI	Confidence interval
clo	Clothing insulation factor
CNR	Contrast-to-noise ratio
CT	Computed tomography
DIO2	Deiodinase iodothyronine type II
DWI	Diffusion weighted imaging
DXA	Dual-energy x-ray absorptiometry
e^-	Electron
F	Fat
$FADH_2$	Flavin adenine dinucleotide (hydroquinone form)
FFA	Free fatty acids
FGF21	Fibroblast growth factor-21
FID	Free induction decay
FOV	Field of view
FSF	Fat signal fraction
FWMRI	Fat-water MRI
GLC	Gas-liquid chromatography
H+	Proton
HOX-C9	Homeobox protein HOX-C9
HU	Hounsfield Units
IL-6	Interleukin-6
imFFE	Interleaved multiple fast field echo
IP	In-phase
ISMRM	International Society for Magnetic Resonance in Medicine
IV	Intravenous
IVIM	Intravoxel incoherent motion

mFFE	Multiple fast field echo
MIP	Maximum intensity projection
MPatK	Mean precision at K
MPatKmax	Mean precision at Kmax
MRI	Magnetic resonance imaging
mRNA	Messenger Ribonucleic acid
MRS	Magnetic resonance spectroscopy
MUF	Mono-unsaturated fraction
NADH	Nicotinamide adenine dinucleotide (reduced form)
NE	Norepinephrine
NIDDK	National Institute of Diabetes and Digestive and Kidney Diseases
NIH	National Institutes of Health
OP	Out-of-phase
P2RX5	Purinergic cell surface receptor
PAT2	Proton assistant amino acid transporter-2
PET	Positron emission tomography
PGC-1α	Peroxisome-proliferator-activated receptor γ coactivator 1α
PKA	Protein kinase A
PPARγ	Peroxisome proliferator-activated receptor gamma
ppm	Parts per million
PRDM16	PR domain containing 16 protein
PRF	Proton resonance frequency shift
PUF	Polyunsaturated fraction
PUFA	Polyunsaturated fatty acids
R_2*	Transverse signal decay rate
RF	Radio frequency
ROI	Region of interest
SAT	Subcutaneous adipose tissue
SD	Standard deviation
SENSE	Sensitivity encoding
SF	Saturation fraction
SFA	Saturated fatty acids
SNR	Signal-to-noise ratio
SUV	Standardized uptake value
T	Tesla
T_1	Longitudinal relaxation
T_2	Transverse relaxation
T3	Triiodothyronine
TE	Echo time
TIR	Thermal infrared
TN	Thermoneutral
TR	Repetition time
UCP1	Uncoupling protein 1
USDA	United States Department of Agriculture
VAT	Visceral adipose tissue
W	Water

WAT	White adipose tissue
Zic1	Zinc finger of the cerebellum protein
α	Flip angle
β_3	β-adrenergic receptor

PREFACE

Working at the interface of physics and biology, this dissertation applies the principles of imaging physics to better understand aspects of brown adipose tissue (BAT) biology. The overall aims of this dissertation are to provide a detailed introduction to BAT, to increase understanding of the imaging-derived properties of BAT in adult humans, and to apply innovative magnetic resonance imaging (MRI) techniques to better characterize a number of intrinsic properties of BAT. The focus of this work is applying MRI methods to detect morphological characteristics of BAT, as well as correlating the presence of BAT as detected with MRI to detection with positron emission tomography (PET)-computed tomography (CT). This includes developing MRI pulse-programming scripts to improve acquisition of MR data, necessary for making it possible to acquire high-quality data. Additionally, this thesis investigates imaging-derived differences between brown and white adipose tissue. The investigations pursued in this thesis led to four publications, listed below, and the structure of this dissertation is further explained in the following paragraphs.

I. **Gifford A**, Towse TF, Walker RC, Avison MJ, Welch EB. Human brown adipose tissue depots automatically segmented by positron emission tomography/computed tomography and registered magnetic resonance images. *J Vis Exp*. 2015;(96):e52415.

II. **Gifford A**, Towse TF, Walker RC, Avison MJ, Welch EB. Progress toward automatic classification of human brown adipose tissue using biomedical imaging. *Proc SPIE 9417, Medical Imaging 2015: Biomedical Applications in Molecular, Structural, and Functional Imaging*, 94170A. 2015. p. 94170A.

III. **Gifford A**, Walker RC, Towse TF, Welch EB. Correlations between quantitative fat-water magnetic resonance imaging and computed tomography in human subcutaneous white adipose tissue.
Accepted for publication on Nov. 18, 2015, at the *Journal of Medical Imaging*

IV. **Gifford A**, Towse TF, Walker RC, Avison MJ, Welch EB. Characterizing active and inactive brown adipose tissue in adult humans using PET-CT and MR imaging.
Under review at the *American Journal of Physiology Endocrinology and Metabolism*

Chapter 1 provides an introduction to both primary aspects of this work, the biology of adipose tissue and the applied imaging methods. Chapter 2 describes the study design on which this dissertation is based. This covers the subjects recruited, the study setup, all imaging acquisition and the data processing methods employed. Chapter 3 introduces the properties of white adipose tissue (WAT), and explores the correlation between the image-based metrics derived separately from fat-water MRI and CT. This chapter parallels the manuscript on WAT, Paper III. Chapter 4 begins exploring the main focus of this research, MRI of BAT. This chapter describes the development of an automated masking method to segment BAT in the acquired images, as described primarily in Paper I. The chapter then continues, presenting the properties of both inactive and active BAT, and how these values compare to those of WAT. The second half of this chapter is a reflection of Paper IV. Chapter 5 presents the progress made towards developing an automated machine learning method to segment BAT in an automated fashion, without the need for the binary mask used in Chapter 4. This chapter is derived mainly from Paper II. Chapter 6 covers additional MRI-derived properties that relate more directly to the biological functions of BAT. The ideas and concepts proposed in this chapter are preliminary explorations, the results of which have not been published at this time. Chapter 7 concludes the entire dissertation, proposes future work, and explores additional techniques for studying BAT.

Portions of text from the above mentioned published articles have been reproduced here, with permission from the respective publishing journals.

CHAPTER 1

INTRODUCTION

1.1 Motivation and Specific Aims

Adipose tissue is central to many aspects of metabolism in healthy and diseased states. The role of white adipose tissue (WAT) is relatively well understood, with WAT acting primarily as an energy storage site as well as being involved in the endocrine system.[1–3] However a second form of adipose tissue also exists in mammals, called brown adipose tissue (BAT). Though BAT has been studied since the mid 1500s, it has become the focus of much interest and excitement in the past two decades. While the scientific community has thought for some time that the primary role of BAT is to activate in response to cold, thereby releasing heat,[4–6] more recent evidence shows BAT also performs as an endocrine organ. Research continues to uncover more about the role BAT plays in the endocrine system, such as secreting adipokines which signal multiple tissues[7,8] and organs.[9] Research also shows BAT plays a role in whole body metabolism, assisting with glucose homeostasis and insulin sensitivity.[10,11] While these recent findings regarding BAT are exciting, much of our understanding of BAT today still comes from animal models even though studies show that cold-activated BAT is present in adults.[12–14]

The research into human BAT is somewhat limited because the primary technique for detecting BAT is through ^{18}F-fluorodeoxyglucose (^{18}F-FDG) positron emission tomography (PET)-computed tomography (CT) imaging. Although a useful technique for detecting the glucose metabolism of active BAT, it does not reveal other substrate fuel such as fatty acids,[15,16] and is limited due to the use of ionizing radiation. Consequently, to fully understand the function

of BAT and its role in whole body energy metabolism, new imaging techniques need to be employed. Though magnetic resonance imaging (MRI) has been proposed as an alternative BAT imaging technique,[17] there are still very few studies to date using MRI to study BAT in adults. Therefore the purpose of this research is to quantify the PET-CT and MRI characteristics of active and inactive clavicular BAT in healthy adult subjects, and to compare these to the values in subcutaneous WAT. Specifically, the aim of this research is to answer questions on adipose tissue morphology, composition and function. To achieve these goals we proposed acquiring PET-CT and MRI scans on the same cohort of healthy adult subjects after exposing the subjects to warm or cold temperatures. This would enable the characterization of BAT in both states: inactive (warm scan) and active (cold scan).

Goal of Specific Aim 1: Use MRI methods to detect morphological characteristics of BAT, as well as correlating the presence of BAT as detected with MRI to detection with PET-CT. We hypothesized that BAT would be observable on MRI in both active and inactive states thereby demonstrating that MRI is a promising alternative to CT for imaging BAT and providing morphological information.

Goal of Specific Aim 2: Optimize MRI methods for detecting metabolically active BAT, as compared to both WAT and non-active BAT. We hypothesized that MRI BAT would have a lower fat-signal fraction under active conditions, and that internally-referenced fat-water MRI proton resonance frequency shift thermometry can measure the elevated temperature of metabolically active BAT thereby demonstrating that MRI is a promising alternative to PET for detecting the activation of BAT.

Goal of Specific Aim 3: Develop and optimize MRI methods for molecular characterization of BAT, as compared to WAT. We hypothesized that the triglyceride

characteristics such as saturation fraction as measured using MRI, are different between BAT and WAT.

Successfully achieving these aims will provide a foundation for performing MRI-based analysis of human BAT. The techniques developed will provide a method to obtain valuable clinical assessments of BAT and to study BAT's relationship with many pathological disorders.

1.2 Exploring adipose tissue

1.2.1 Physical Characteristics of WAT and BAT

White and brown adipocytes form two distinct tissue types in the mammalian body, each with unique characteristics and purpose. WAT serves mainly as a fuel repository for the body, storing and releasing fatty acids between meals.[1,2] Primarily located as a near-continuous subcutaneous layer with additional depots located surrounding organs; WAT can be considered to form a large organ, accounting for up to 20% and 40% of the body weight in healthy and obese adult humans, respectively.[18] White adipocytes range from 25-200 μm in size.[19,20] The increased size is due to the uptake of fatty acids for storage, which can enlarge the lipid vacuole size dramatically.[21,22] Each white adipocyte is spherical, with a single large lipid vacuole occupying the majority of the cellular space. This causes the cytoplasm, nucleus and other organelles to be displaced to the outer rim of the cell,[22] as seen in Figure 1.2-1. Each adipocyte also contains limited mitochondria, the organelle responsible for generating most of the cell's energy in the form of adenosine triphosphate (ATP), with only enough to provide the ATP for the cell's needs.[2]

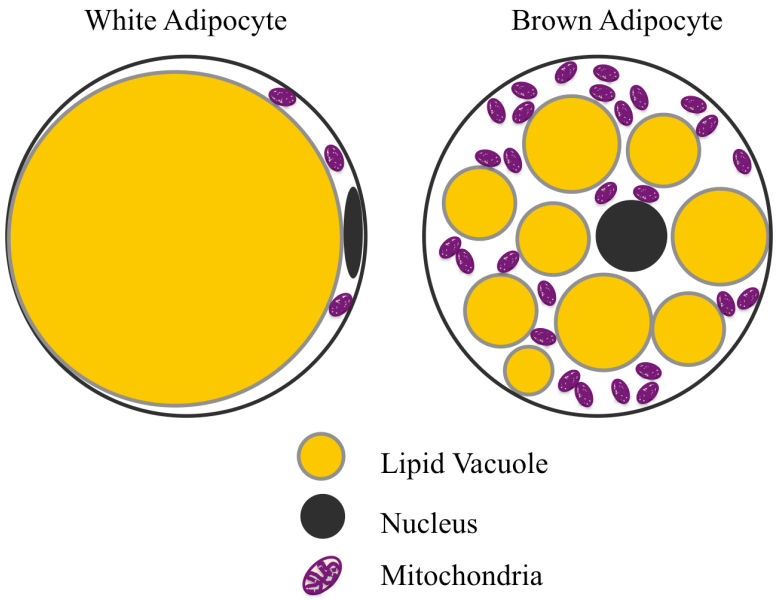

Figure 1.2-1. Schematic of the typical morphology of white and brown adipocytes.

Contrary to WAT, BAT is capable of switching between a passive storage state, here called "non-active BAT," and an active state or "activated BAT." When activated, BAT is responsible for non-shivering thermogenesis and the release of hormones as part of the endocrine system. The thermogenic and endocrine properties of BAT will be discussed further in sections 1.2.3 and 1.2.4, respectively. BAT takes form in smaller depots than WAT, primarily located around or near vital organs. The BAT depot locations for rodents, human infants, and adults are depicted in Figure 1.2-2. In small mammals such as mice and rats, BAT is located primarily in the interscapular region, with additional depots located in the subscapular, cervical, perirenal, and inguinal regions.[5] These regions are preserved in human neonates and young infants, with additional clavicular depots and occasional depots also appearing in the periaortic and neck region.[23–25] However, as infants age, the depots of BAT begin to change. By early adulthood, the primary location of BAT has changed from the interscapular depot to the lower neck and

supraclavicular region. Paravertebral, axillary, perirenal, and periaortic depots occasionally accompany the clavicular depots.[23]

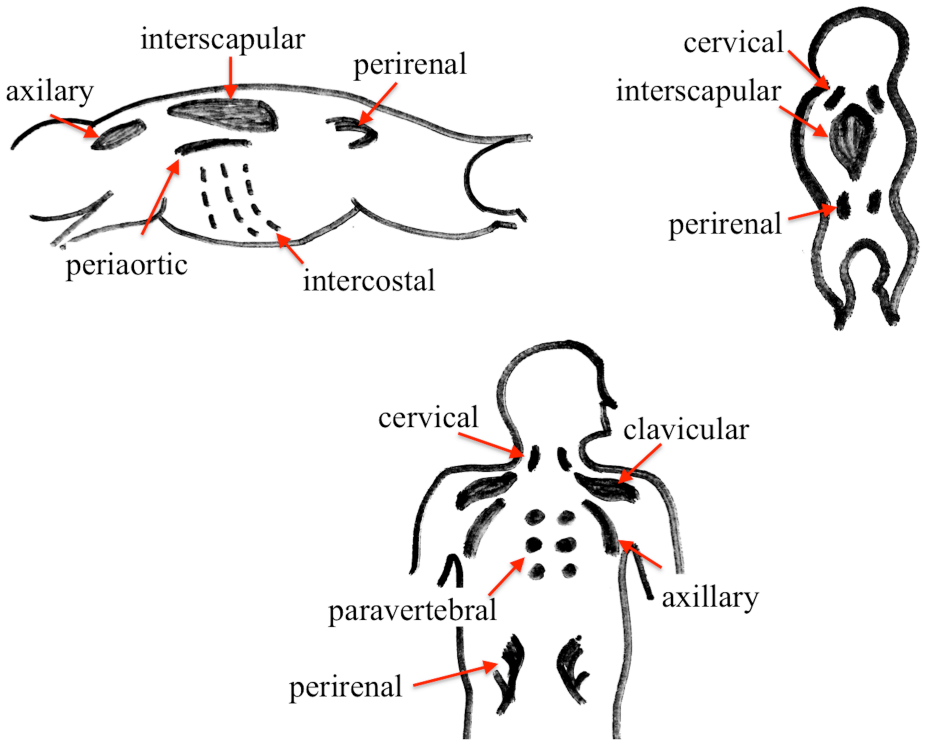

Figure 1.2-2. BAT depot locations in rodents, human infants, and adults.

Unlike WAT, BAT is highly innervated by the sympathetic nervous system and perfused by a dense vascular network.[1] The sympathetic nervous system triggers BAT to become active, thereby releasing heat. This process is covered more in depth in following sections. The adipocytes forming BAT are also much smaller than WAT, only 15-40 μm in diameter.[19,20] Each adipocyte is multilocular, containing many small lipid vacuoles, with a more centrally located nucleus, as seen in Figure 1.2-1. Brown adipocytes are also abundant with mitochondria, which contain an uncoupling protein (UCP1). UCP1 is uniquely expressed in brown adipocytes[1] and

exists on the inner mitochondrial membrane.[26] The role UCP1 plays in thermogenesis is discussed more in later sections.

1.2.2 Cell Lineage

Though both are defined as adipose tissues, brown and white adipocytes are derived from different cell lineages. Additionally, the category of brown adipocytes can be divided into "brown" and "beige" adipocytes.[27] Beige, also called "brite" for "brown-in-white," adipocytes are very similar phenotypically to brown adipocytes but are in fact derived from a slightly different cell lineage and have different cell surface markers than both brown and white adipocytes.[28] Beige adipocytes reside in WAT depots and - aside from the cell surface markers - are initially visually indistinguishable from white adipocytes. However, upon chronic cold stimulation these white-appearing adipocytes can begin expression of UCP1 and become multilocular beige adipocytes.[29–32] In addition to chronic cold exposure, beige adipocytes can also be induced through exposure to certain hormones such as Irisin[33] and fibroblast growth factor-21 (FGF-21), and transcription regulators such as PPARγ, peroxisome-proliferator-activated receptor γ coactivator 1α (PGC-1α), and PRDM16.[34]

Though the study of cell lineage is currently ongoing, the following differences have been shown to exist between the three categories of adipocytes. Classical white adipocytes stem from adipocyte precursors derived from mesenchymal stem cells,[35,36] while brown adipocytes are derived from the same mesenchymal precursors from which muscle and dermis cells are also derived.[27,37,38] Beige adipocytes appear to be derived from a similar progenitor to white adipocytes, however the story is still unfolding.[28,39,40] The lineage of white, beige and brown adipocytes is illustrated in Figure 1.2-3.

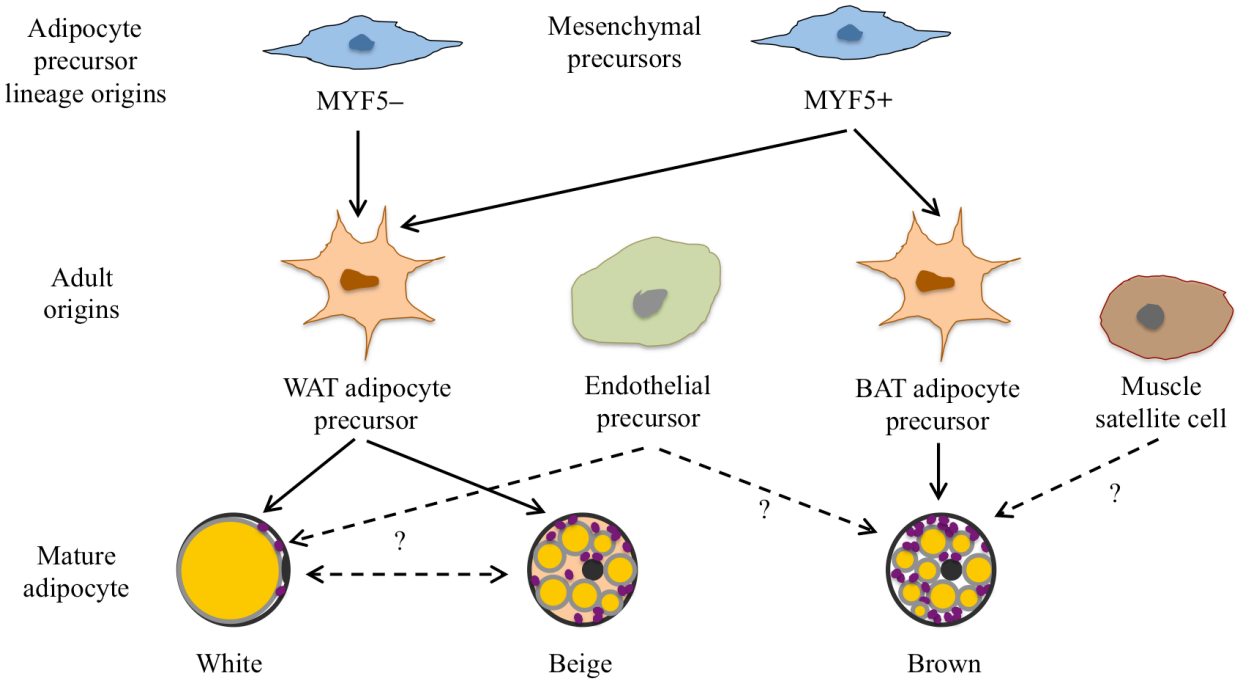

Figure 1.2-3. Cell lineage of white, beige and brown adipocytes.

A few of the distinguishing characteristics and cell markers for the three varieties of adipocytes are listed in Table 1.2-1.[38,41,42]

Table 1.2-1. Markers and characteristics of white, beige and brown adipocytes.

White	Beige	Brown
Myf5-negative precursors	Myf5-negative & Myf5-positive precursors	Myf5-positive precursors
Leptin	UCP1	UCP1
DPT (Dermatopontin)		DIO2
	PAT2	PAT2
ASC-1	P2RX5	P2RX5
		ADRB3
HoxC9 (Homeobox C9)		Zic1

Abbreviations: UCP1: Uncoupling protein 1, DIO2: Deiodinase iodothyronine type II allows BAT to sustain an elevated metabolic state.[43] β_3-adrenergic receptors (ADRB3) are involved in regulating lipolysis and thermogenesis as well as norepinephrine-induced activation in BAT.[6] ASC-1: amino acid transporter is a cell surface protein, PAT2: proton assistant amino acid transporter-2, P2RX5: purinergic cell surface receptor.

1.2.3 BAT Thermogenesis

As introduced earlier, one of the main roles of brown adipose tissue is to generate heat. Research in both small mammals[5,44,45] and humans[12] shows that exposure to cold temperatures causes BAT to become metabolically active and release heat. One mechanism for activating BAT is through the sympathetic nervous system. The sympathetic nervous system is highly innervated in BAT,[46] and regulates the body's response to energy deficits due to conditions such as energy shortages (fasting) or increased energy expenditure (cold exposure).[47] The sensation of cold causes the hypothalamus to release norepinephrine via the sympathetic nervous system, which signals both WAT and BAT. When the sympathetic nervous system signals WAT, it triggers lipolysis of the stored lipids, causing the release of nutrients for other organs including BAT.[48]

Because BAT is highly innervated it undergoes rapid stimulation when norepinephrine is released, which signals the brown adipocyte to activate, beginning the thermogenic process. The

norepinephrine binds to the β-adrenergic receptors on the surface of brown adipocytes and triggers lipolysis through the cyclic monophosphate (cAMP)-dependent protein kinase A (PKA) signaling pathway.[39] This causes the lipid droplets to undergo lipolysis, providing free fatty acids (FFAs), which serve as the main substrate for oxidation.[30,48] The released FFAs are transported to the inner mitochondrial space where they serve two purposes. First they undergo β-oxidation, forming Acetyl coenzyme A (acetyl-CoAs), which enter the citric acid cycle. This results in the formation of the reduced electron carriers NADH and $FADH_2$, which are oxidized in the electron transport chain located on the inner mitochondrial membrane (Figure 1.2-4). This, in turn, causes protons to be pumped from the mitochondrial matrix to the mitochondrial intermembrane space forming a proton gradient across the membrane. This process is no different than what occurs in other cells; the difference exists because brown adipocytes contain large amounts of the enzymes involved,[49] and because of the unique presence of UCP1.

The second role of the FFAs is to activate UCP1, the central protein in the thermogenesis cycle. In cells with no UCP1, or in inactive BAT, the proton gradient is reversed through the synthesis of ATP by the ATP synthase enzyme.[26] The presence of UCP1 however allows the protons to bypass the ATP synthase enzyme and "leak" back across the inner membrane of mitochondria, generating heat instead of ATP,[6,50,51] as shown in Figure 1.2-4.

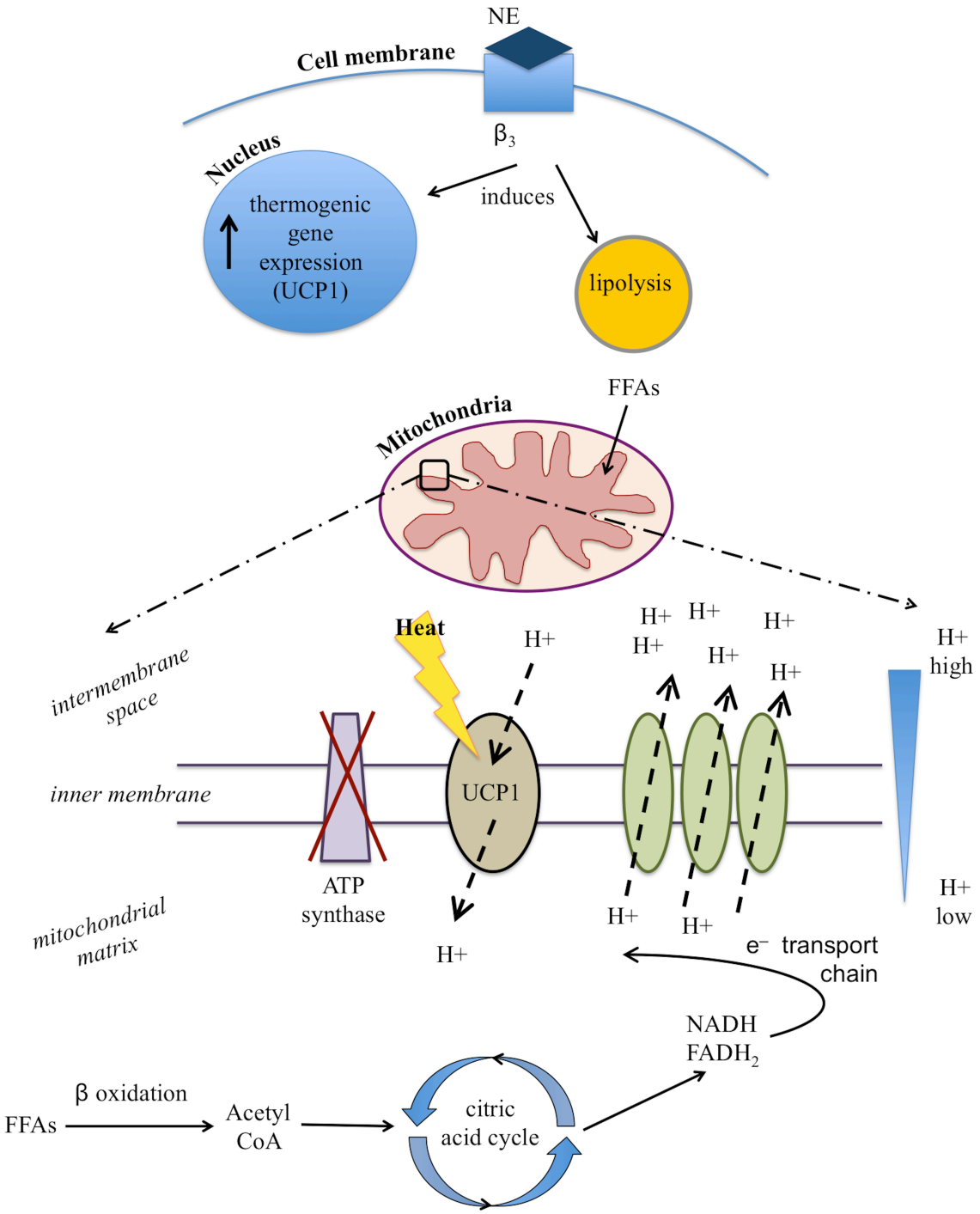

Figure 1.2-4. Schematic of cold-induced thermogenesis in activated BAT. Abbreviations: NE: norepinephrine, β_3: β-adrenergic receptor, UCP1: uncoupling protein 1, FFAs: free fatty acids, NADH: Nicotinamide adenine dinucleotide, FADH2: Flavin adenine dinucleotide, e^-: electron, H+: protons, ATP: adenonsine triphosphate.

The importance of UCP1 was shown in research of UCP1-ablated (UCP1(–/–)) mice.[52] This research by Matthias et al. showed that UCP1(–/–) brown adipocytes functioned the same as wild-type cells in the response to norepinephrine (also called noradrenaline) induced lipolysis. However the wild-type cells had approximately a 10-fold increase in thermogenesis over the UCP1(–/–) cells. Their research concluded that thermogenesis cannot be induced in brown adipocytes lacking UCP1.[52] It is also possible for BAT to lose its ability to generate heat. Exposure to warm temperatures reduces the norepinephrine signal to BAT thereby reducing the amount of activation. Prolonged exposure to warm conditions can cause the adipocytes to decrease gene expression for UCP1 and increase the production of the hormone leptin, becoming more WAT-like. Further discussion of leptin and hormone signaling is continued in section 1.2.4. Without UCP1, no thermogenesis can be induced in brown adipocytes, even with norepinephrine signaling.[52] In addition to exposure to heat, research shows that BAT activity can be suppressed through the use of several different medications such as: β-blockers,[53] oral diazepam or intravenous fentanyl.[54]

Contrary to losing BAT, it is also possible to stimulate the growth and activation level of BAT. Research in the primates Macaca mulatta and Microcebus murinus show they recruit BAT after severe and chronic cold acclimation, in a similar manner as in mice.[55–57] Prolonged exposure to cold causes brown adipocytes to synthesize new mitochondria and UCP1. The brown adipocyte count also increases, thereby increasing the total volume of BAT, and the vasculature and neural network are also expanded.[6,46] This effect has also been shown in humans where prolonged exposure to cold increased both the oxidative capacity and volume of BAT.[58] Perhaps even more important is the finding that prolonged cold exposure can cause the formation of beige adipocytes within WAT depots.[59,60] With the majority of the research on adipocyte

"browning" published in the last three years, the ability to induce beige adipocytes is a hot topic with much still to be understood. However, the research so far shows that both pharmacological and environmental effects play a role. For example beige adipocyte recruitment occurs in humans after prolonged adrenergic stress from burns,[61] and chronic cold exposure.[62,63] Research in mice shows that additional mediators such as Irisin[64] and FGF-21[65,66] may also induce browning of WAT depots. The possibility of recruiting beige adipocytes is of great interest because it has been shown mice are resistant to weight gain after enhanced BAT activity and recruitment of beige adipocytes.[38]

1.2.4 Endocrine Function and Hormonal Signaling

Though the classical view of the function of WAT is its long-term fuel storage and of BAT is its role in non-shivering thermogenesis, both tissues also function as endocrine organs.[67,68] White adipocytes secrete several hormones and adipokines such as leptin, and adiponectin, and are influenced by other signals such as interleukin-6 (IL-6). Leptin is a hormone created primarily by white adipocytes that acts in part on the hypothalamus to stimulate satiety[69] and inhibit hunger.[70] Research also shows that insulin-resistant patients with lipodystrophy showed improvement in whole-body insulin-stimulated glucose metabolism after treatment with leptin.[71] Adiponectin, a protein secreted by white adipocytes is another important hormone. Responsible for several metabolic processes such as glucose regulation and fatty acid oxidation, adiponectin levels in plasma are high in comparison to other hormones.[72] IL6 however is a cytokine expressed by white blood cells. IL-6 is an important inflammatory molecule, and increased levels of IL-6 have adverse effects on insulin signaling, and the presence of IL-6 is inversely related to the secretion of adiponectin.[21,73]

The two adipokines previously discussed, leptin and adiponectin, are poorly expressed by brown adipocytes, and their presence or absence is often used as markers to distinguish between WAT and BAT. Brown adipocytes do however secrete their own endocrine factors, acting on several tissues and organs. The most prominent BAT-derived endocrine factors are FGF-21, and IL-6. FGF-21 is a powerful endocrine factor, responsible for promoting glucose oxidation in the liver, WAT and pancreas.[66,74,75] Additionally, recent research shows that FGF-21 can cross the blood-brain barrier and may act to increase hepatic insulin sensitivity in rats with diet induced obesity.[76] This indicates that BAT endocrine factors can also influence the central nervous system in a similar manner to traditional adipokines. FGF-21 has also been identified as being expressed by beige adipocytes, suggesting that beige adipocytes also have an endocrine role.[8,77–79] In addition to being a proinflammatory molecule, as previously discussed, IL-6 is also expressed by active brown adipocytes.[80] It has also been shown that the presence of IL-6 is required for BAT transplantation to improve the metabolic status in mice, however it is not yet known why.[81,82] Figure 1.2-5 maps the role of BAT as an endocrine organ, and the factors secreted by other organs that modulate BAT activity.

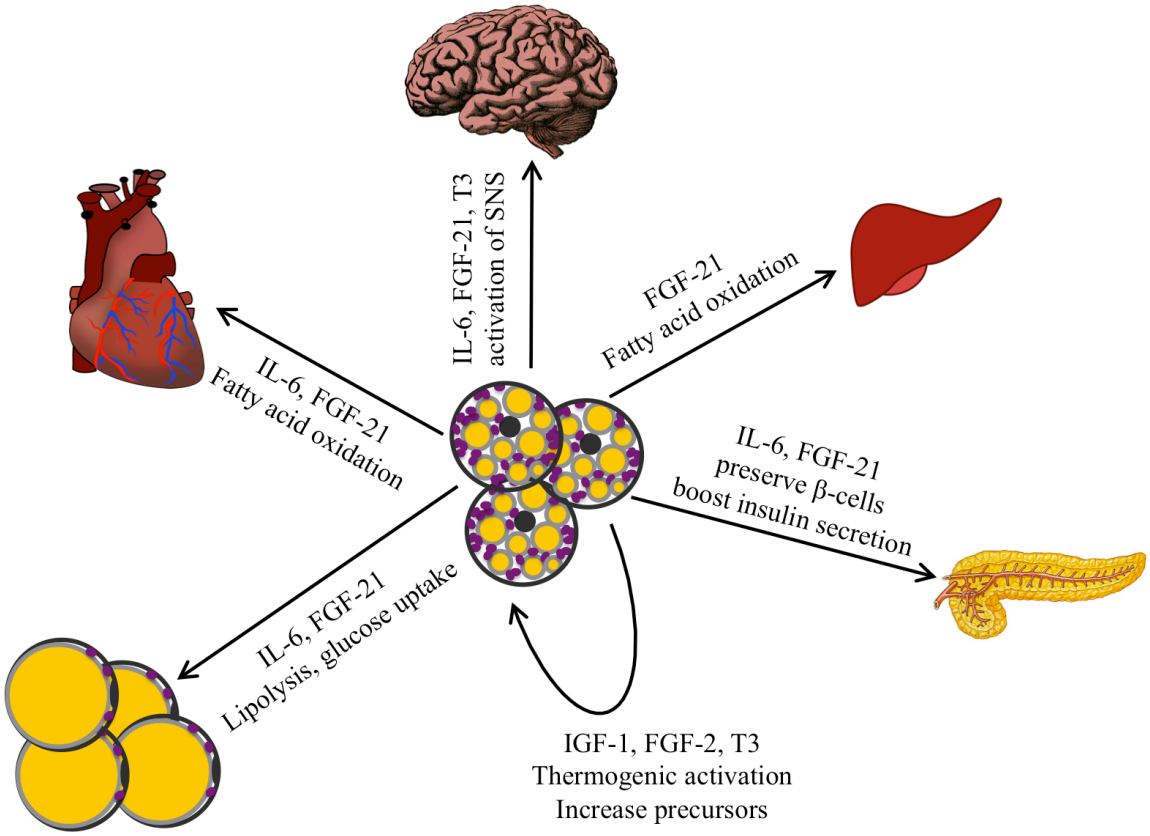

Figure 1.2-5. Brown adipose tissue endocrine signaling factors, influencing itself, and white adipose tissue, as well as the heart, brain, liver and pancreas.

Two key factors that act on BAT are Triiodothyronine (T3), and irisin. The first, T3, is a hormone secreted by the thyroid that affects physiological processes such as metabolism and body temperature. However, BAT is also capable of producing T3, indicating that BAT also sends signals that influence the body's energy expenditure.[83,84] The second, irisin, is a protein secreted by muscle after exercise. Irisin was only recently found in 2012 by Boström et al.,[64] and quickly received interest for its role in the stimulation of beige adipocyte production. The work by Boström et al. showed that when increased irisin levels were induced in obese mice, it caused beige adipocytes to form in the WAT depots, the mice lost weight, and their glucose tolerance and insulin sensitivity were improved. They also showed that blocking irisin diminished

exercise-induced browning. Since this exciting discovery, research has resulted in conflicting evidence over the validity of irisin as an exercise-induced hormone that causes browning of adipocytes in WAT. Overwhelming evidence indicated that there was no correlation between increased irisin levels and exercise,[7,85–87] reducing the possibility for irisin to play a significant role in the browning of WAT depots in humans. Other research however was able to corroborate the original findings, showing an elevated level of irisin after exercise in healthy adults,[88,89] including a second report just released by the original group.[90] Given the immense potential of irisin in mediating the browning of adipocytes, it has garnered significant attention; however there is still much to be learned about irisin.[91]

1.3 BAT in Humans

1.3.1 A Brief History

The earliest known work describing brown adipose tissue was performed by the Swiss naturalist and physician, Conrad Gessner in 1551, when he described a piece of tissue in marmots as "neither fat, nor flesh, but something in between".[92] Now, nearly 500 years later, though much has been learned, this type of tissue is still a great curiosity.

Between 1551 and 1976, the majority of our knowledge on BAT came from dissection, observation and microscopy. Little was published between 1551 and 1670 when Velsch described tissue in the back of small rodents which he described as gland-like and similar in structure, appearance, and function to the lymphatic system and the thymus.[93] This was largely believed correct until 1817 when Jacobson proved with research in marmots, hedgehogs, and bats that the tissue was distinct from the thymus though it was still considered a ductless gland.[94]

During the following 100 years the tissue became known by many names, the most common being "hibernating gland".[95]

Though much of the research in those first 400 years focused on animals, studies with humans - particularly with human fetuses - were performed as early as 1899.[95] The research performed by Merkel in 1899, Hatai in 1902, and Bonnot in 1908 showed that the interscapular and dorso-cervical fat pad of human fetuses was similar in features to the so-called hibernating gland in previous mammal research.[95,96] Bonnot also showed that the fat pad volume varied and was largest in fetuses from well-nourished mothers.[96] At this time Bonnot also found and characterized tissue with similar properties in 25 adult humans, being one of the first to do so. He described the tissue as possessing similar color, cellular properties, and blood vessel density to that of fetuses and small mammals.[96] His autopsy work showed the largest region of the tissue occurs in the lower neck and clavicular region, with extensions down to the superior scapula and up to the mastoid process.

Starting in the early 1900's until the 1990's, limited research was performed on brown adipose tissue in humans. Two reports of brown fat-like tumors were published in 1927 and 1950: The first one discussed the appearance of a tumor in the neck of an 11-week-old female child,[97] and the second one regarding a tumor in the posterior cervical region of a 21 year old male.[98] Two of the largest histological studies on the presence and location of brown fat in humans were performed by Heaton in 1972,[23] and Tanuma et al. in 1975.[99] Heaton performed complete autopsies on 14 children aged 0 to 10 years, 7 adolescents 11-20 years, and 31 adults aged 21-70 years, who had all been healthy before dying suddenly. His findings indicated that BAT was present in adults throughout life, but the number and size of BAT depots diminished greatly after 50 years of age. In the work by Tanuma et al., they performed biopsies of the

perirenal fat in 125 humans aged 1 month to 86 years. The results from Tanuma et al. indicated that the presence of BAT in the perirenal depot is most prominent in infants and declines with age. It is from this work that much of the understanding regarding the location of BAT in adult humans is derived, as well as the thought that the presence of BAT declines with age. Apart from these studies, little else was published in the 1900's on BAT in humans. Perhaps this was because BAT was still believed to be a gland associated with hibernation, and therefore research focused on hibernating mammals.[55,100,101] Or perhaps it was because of the limited number or studies reproducing Bonnot's 1908 findings in adults. Whatever the reasons, it was not until the late 1900s that interest in studying BAT in humans was rekindled.

1.3.2 The Re-"Discovery" of BAT in Humans

Prior to the invention of tomographic imaging techniques, all research on BAT was conducted using dissection and microscopy techniques. However this quickly changed when it was discovered in 1980 that tumors and other tissues with high glucose metabolism showed marked uptake of the PET radiotracer ^{18}F-FDG.[102] Although this finding almost immediately solidified the use of ^{18}F-FDG PET scans as a major clinical tool, almost 20 years passed before Engel et al. first made reference to areas of "artifactual accumulation" of ^{18}F-FDG in the shoulder region of patients.[103] At this same time in 1996, Barrington et al. also noted patterns of ^{18}F-FDG uptake in the neck and paravertebral space. At the time, these regions of uptake were attributed to muscle, partly because of the lack of soft-tissue contrast in the PET images, and partly due to the disappearance of the "artifactual accumulation" after taking muscle relaxants and performing a second scan.[104] The muscle relaxant used to reduce the uptake of ^{18}F-FDG is in the benzodiazepine family of drugs.

In 1998 a breakthrough in medical imaging occurred when PET and CT scanners were combined.[105] Using the newly combined power of the PET-CT scanner, Hany et al. analyzed 638 patients admitted for PET-CT scans in 2001.[106] They noted that while the symmetrical ^{18}F-FDG uptake in the neck and cervical spine region was well known, up to that point it had been attributed to muscular uptake. The work by Hany et al. aimed to re-evaluate this tissue region with the relatively newly combined PET-CT machine, using the soft-tissue contrast provided by the CT scanner to distinguish the tissue with increased glucose uptake. Of the 638 patients analyzed, only 17 showed the symmetrical ^{18}F-FDG uptake pattern. However, Hany et al. noted that the uptake in all 17 patients was localized to regions of adipose tissue, not muscle, as defined by the CT image. From these results, Hany et al. hypothesized that this tissue was in fact BAT, as the location correlated to the location of BAT described previously.[23] Two years later Cohade et al.[107] and Yeung et al.[108] both separately reported on the uptake of ^{18}F-FDG in the clavicular region of patients admitted for PET-CT scans. Both groups also noted that the regions of clavicular uptake were localized to areas of adipose tissue, and should not be confused with regions of malignant or metastatic uptake. Cohade et al., also attempted to coin the term "USA-fat", for Uptake in the Supraclavicular Area Fat,[107] but the term was not adopted widely.

This sudden availability and ease of imaging in the clinic resulted in the unexpected detection of regions of BAT and began to reignite an interest in studying BAT in humans. However even with these reports on the possibility that adults retained BAT depots, the majority of the studies over the next several years aimed not to understand the tissue, but rather how to pharmacologically reduce the uptake of ^{18}F-FDG in BAT to remove it from PET scans.[53,54,109] It was not until 2009 that three independent groups all provided histological confirmation that BAT

was responsible for the ^{18}F-FDG uptake in the clavicular adipose tissue of healthy adult humans under controlled studies,[12–14] which caused interest in the field of BAT research to explode.

1.3.3 Is FDG Indicative of Active BAT?

Because activated BAT takes up glucose, the scientific community thought it probable that the uptake of ^{18}F-FDG in adipose tissue was representative of BAT. However, as previously mentioned, this was not confirmed until the work performed by Saito et al,[12] Virtanen et al.,[13] and van Marken Lichtenbelt et al.,[14] in which they performed PET-CT scans on healthy adult subjects. Additionally, two of the studies were performed after exposing the subjects to both cold and warm temperatures for two hours.[13,14] In the work by Virtanen et al., a tissue biopsy was performed of both the supraclavicular BAT and the subcutaneous WAT after each scan. Tissue biopsy analysis showed that UCP1, DIO2, PGC1α mRNA, PRDM16, and ADRB3 were all increased in the BAT biopsy tissue multifold over the expression detected in the WAT biopsy. The presence of these five markers indicated that the adipose tissue exhibiting uptake of ^{18}F-FDG is indeed brown adipose tissue.

However, care must be taken to distinguish between the fact that the presence of elevated levels of ^{18}F-FDG in adipose tissue is indicative of activated BAT, and the incorrect conclusion that an absence of ^{18}F-FDG would indicate an absence of BAT, or BAT that is not active. Without biopsy samples of the tissue it is not possible to determine for certain if the tissue is indeed BAT. This illustrates one of the main issues with using PET-CT imaging to detect BAT: it relies on the uptake of ^{18}F-FDG by active brown adipocytes to determine the presence of BAT. Therefore, if no uptake occurs, it is assumed that BAT does not exist in that subject. Previous research shows this is untrue, and that brown adipocytes are present in the supraclavicular

adipose depot of subjects who are PET-negative.[110] Biopsy samples of the clavicular adipose depot in these subjects mainly contained unilocular adipocytes, but there existed a scattering of multilocular cells, which stained positive for BAT specific markers such as UCP1.[110] Furthermore, other work shows that the supraclavicular adipose tissue of PET-negative subjects is capable of differentiating *in vitro* into brown adipocytes.[111] These two findings demonstrate that the prevalence of BAT in adults may be higher than PET scans indicate, which is exciting when considering the possible role BAT may play in mitigating the metabolic syndromes.

1.3.4 Is Human BAT Brown or Beige?

Given that both brown and beige fat exist, it becomes important to determine which fat occurs in humans. Research shows that it depends on where you look. It was initially thought that humans had beige adipocytes, not brown.[77] This was disputed when Lidell et al.[112] and Cypess et al.[113] each showed that humans have both brown and beige adipocytes and that the type of fat present depended on the anatomical location. The work performed by Lidell et al. focused on human infants, and showed that the interscapular depot expressed UCP1 and Zic1 (a Zinc finger of the cerebellum protein), an indication of brown fat. They also analyzed perirenal adipose tissue, noting that due to the low expression of Zic1 and higher expression of Homeobox protein HOX-C9, this tissue was more likely to be beige adipose. Cypess et al. analyzed the layers of fat in the necks of adult humans, discovering that white, beige, and brown adipocytes can be present. Their work showed that the most superficial subcutaneous adipose tissue contained no UCP1 and displayed adipocytes consistent with classic white adipose tissue. A second region of adipose tissue that had sporadic expression of UCP1 and appeared more consistent with the morphology of beige adipocytes. The deepest level of adipose tissue had

characteristics consistent with classical BAT, with the smallest lipid vacuoles and highest mitochondrial count. Furthermore, this deep adipose layer expressed both UCP1 and Zic1, indicating true brown fat.

The distinction between which type of adipose tissue occurs in humans is important because each tissue may respond to unique external catalysts. Therefore, understanding which tissue is present could better direct research. And since humans do appear to have both beige and true brown adipocytes, this indicates that the metabolic benefit of BAT to rodents may also translate to humans.[40,114]

1.3.5 Prevalence and Significance of BAT in Adult Humans

Until roughly 10 years ago, uncertainty remained regarding the presence of BAT in adult humans. Though it is now well accepted that adults have BAT depots its prevalence is still unknown. Retrospective studies of elevated ^{18}F-FDG levels are often used to quantify the prevalence of BAT in the adult population, citing the prevalence as anywhere from 7%[107] to 33%[12]. However, retrospective studies do not necessarily provide an accurate measure, partly because the study conditions are not controlled, and also because BAT may be present even without the elevated uptake of ^{18}F-FDG. More recent prospective studies indicate a much higher prevalence, ranging form 40-100%.[13,14,115–118] The results from the research for this dissertation show a prevalence of 83% in the subjects studied.

Is the presence of BAT significant for humans? The thermogenic nature of BAT is perhaps more necessary and useful in human infants, as BAT forms a larger percentage of body mass and total adipose mass, and the surface area to volume ratio is much larger. Additionally, newborn humans transition from an environment at 37°C to an environment typically at much

lower temperature. This factor along with a higher surface area-to-volume ratio than in adult humans, makes it specifically challenging for infants to maintain their internal body temperature in a homeothermic range.[119] Adult humans have a higher ratio of heat production due to basal metabolism and the smaller surface-area-to-volume ratio relative to infants. It is possible that the more important function of BAT in adult humans is not the release of heat, but rather its contribution to the endocrine system, however this research is currently ongoing.

BAT in mice accounts for approximately 5-10% of their total body weight, while in humans it is roughly 0.05-0.5% total body weight.[120] When activated by exposure to 18°C, approximately 60 grams of human clavicular BAT had a glucose uptake rate of 12.2 μmol per 100 grams per minute. If continually active at this rate, the BAT would have taken up 11 mmol of glucose in 24 hours.[13] However, the predominate substrate for BAT activation is free fatty acids, and in rats it has been shown that only approximately 10% of the total BAT metabolism is from glucose.[121] Therefore, if this ratio of glucose to fatty acids in BAT metabolism holds true for humans, then the amount of fuel consumed could be important. For example, if the rate of 11 mmol of glucose per 24 hours constitutes only 10% of the total metabolism, with fatty acids accounting for the remainder, then this would result in approximately 4-5 kg of adipose tissue being metabolized in a year. Therefore, given that this is a small amount of fat relative to total body weight, it is possible BAT is more useful as a method of metabolic maintenance rather than weight loss.[122,123]

1.3.6 Where Is the Field Now?

The field of BAT research has been ongoing for hundreds of years. However, as discussed previously, it is only within the past 10-15 years that the research on BAT in humans

has renewed. In February of 2014, the National Institutes of Health (NIH) National Institute of Diabetes and Digestive and Kidney Diseases (NIDDK) hosted a workshop titled "Exploring the Roles of Brown Fat in Humans".[124] From this workshop it became clear that the current field of human BAT research is still limited due to the lack of definitive noninvasive methods to quantify the mass, activity level and potential for activation of BAT in all locations and forms (i.e. brown or beige). Most imaging studies employ PET-CT to detect and characterize BAT, and a few studies use MRI instead, or PET/MR systems. However, no studies have used PET/CT and MRI on the same subjects. Furthermore, though known that the behavior of BAT differs between its active and inactive states, many of the studies obtain data only after exposure to cold. The research methods presented in this dissertation are, to our knowledge, novel in the field of human BAT research. Table 1.3-1 summarizes the methods used in many of the recent imaging-based studies on human BAT.

Table 1.3-1. Methods utilized in recent studies on human BAT, in comparison to the research methods of the research in this dissertation.

Author	Journal	Year	Human	Adult child	Healthy	Disease	PET	CT	MRI	Other	Biopsy	Cold	Warm	Temperature not a factor
Saito	Diabetes	2009	x	adult	x		x	x				x	x	
van Marken Lichtenbelt	New Eng J Med	2009	x	adult	x		x	x				x	x	
Hu & Gilsanz	AJRoentgenol	2013	x	both		x			x					x
Vosselman & Lichtenbelt	Am.J. Clin Nutr	2013	x	adult	x		x	x				x		
Rooijen & Marken Lichtenbelt	Invest. Radiol	2013	x	adult	x		x	x	x			x		
Chen & Kwong	J Nuc Med	2013	x	adult	x				x			x	x	
Chen & Celi	J.Clin. Endocrin Metab	2013	x	adult	x		x	x				x	x	
Schlogl & Thearle	J.Clin. Endocrin Metab	2013	x	adult	x		x	x				x		
Reddy & Barber	J.Clin. Endocrin Metab	2013	x	adult		x	x	x	x		x			x
Yoneshiro & Saito	J.Clin. Investigation	2013	x	adult	x		x	x				x		
van der Lans & Marken Lichtenbelt	J.Clin. Investigation	2013	x	adult	x		x	x			x	x		
Cypess & Tseng	Nat. Med	2013	x	adult	x					gene expression				
Lidell & Enerback	Nat. Med	2013	x	infant		x			x	gene expression				x
Admiraal & Verberne	Nuc Med	2013	x	adult	x		x	x		SPECT		x		
Zhang & Li	Diab. Metab. Res	2014	x	adult		x	x	x						x
Lee & Celi	Diabetes	2014	x	adult	x		x	x			x	x	x	
Chondronikola & Sidossis	Diabetes	2014	x	adult	x		x	x				x	x	
Yeung & Larson	J Nuc Med	2014	x	both		x	x	x						x
Ovara & Virtanen	J.Cereb Blood & Meab	2014	x	adult	x		x	x						
Kim & Gilsanz	J.Clin. Endocrin Metab	2014	x	child		x			x	TIR				x
Schopman & Holleman	Metabolism	2014	x	adult	x		x	x				x		
Tews & Wabitsch	Molec.Cell.Endocrin	2014	x	adult		x				gene express	x			x
P. Svensson & M. Svensson	Obesity	2014	x	adult	x					biology assay				x
Vosselman & Lichtenbelt	PlOS One	2014	x	adult	x		x	x				x	x	
Boon & Rensen	PlOS One	2014	x	adult	x		x	x		skin temp		x		
Broeders	Cell Metab	2015	x	adult	x		x	x				x		
Blondin	Diabetes	2015	x	adult	x	x	x	x		biology assay		x	x	
Salem	Diabetes, Ob & Metab	2015	x	adult	x		x	x		TIR		x		
Vosselman	Int J Ob	2015	x	adult	x		x	x		DXA	x	x		
Chondronikola	Int J Ob	2015	x	adult	x		x	x			x	x		
Franx	J Nuc Med	2015	x	both		x	x		x					x
Blondin	J Physio	2015	x	adult	x		x	x		biology assay		x	x	
van der Lans	J Physio Sci	2015	x	adult	x		x	x		skin temp		x		
Hanssen	Nat. Med	2015	x	adult		x	x	x		DXA	x	x		
Lundstrom	PlOS One	2015	x	adult	x				x			x	x	
My Research			**x**	**adult**	**x**		**x**	**x**	**x**	**TIR**		**x**	**x**	

1.4 Imaging Methods Used in this Research

1.4.1 Positron Emission Tomography

Though Positron Emission Tomography (PET) imaging was invented in 1961, it took the formation of the radiotracer fluorine-18-labeled glucose analog, Fluorodeoxyglucose, or ^{18}F-FDG in 1976[125] and the discovery in 1980 that tumors show a marked uptake of ^{18}F-FDG[102] for PET imaging to assert itself as a clinical imaging necessity. It is partly due to the general clinical availability and prevalent use of PET imaging that PET became the principle modality for detecting BAT in adult humans.

The principle of PET imaging is based on the detection of radiation emitted from a positron-electron annihilation event. First a radiotracer is injected into the body to be imaged, and this radiotracer becomes distributed through the body. As the radioactive tracer, or radiotracer, undergoes radioactive decay, it emits positrons. The emitted positron then interacts with a nearby electron causing an annihilation event and the formation of two 511-keV photons, as depicted in Figure 1.4-1. These two photons travel in nearly opposite directions and are detected by two cameras on opposite sides of a ring of cameras surrounding the object to be imaged. If the two cameras register the two photons to within 6-12 nanoseconds of each other, then this is considered a true event and it is assumed that an annihilation event occurred along the line between the two detectors. Therefore, by detecting the number and spatial distribution of the photon events, it is possible to reconstruct an image of the concentration of positron decays within the imaged object.[126]

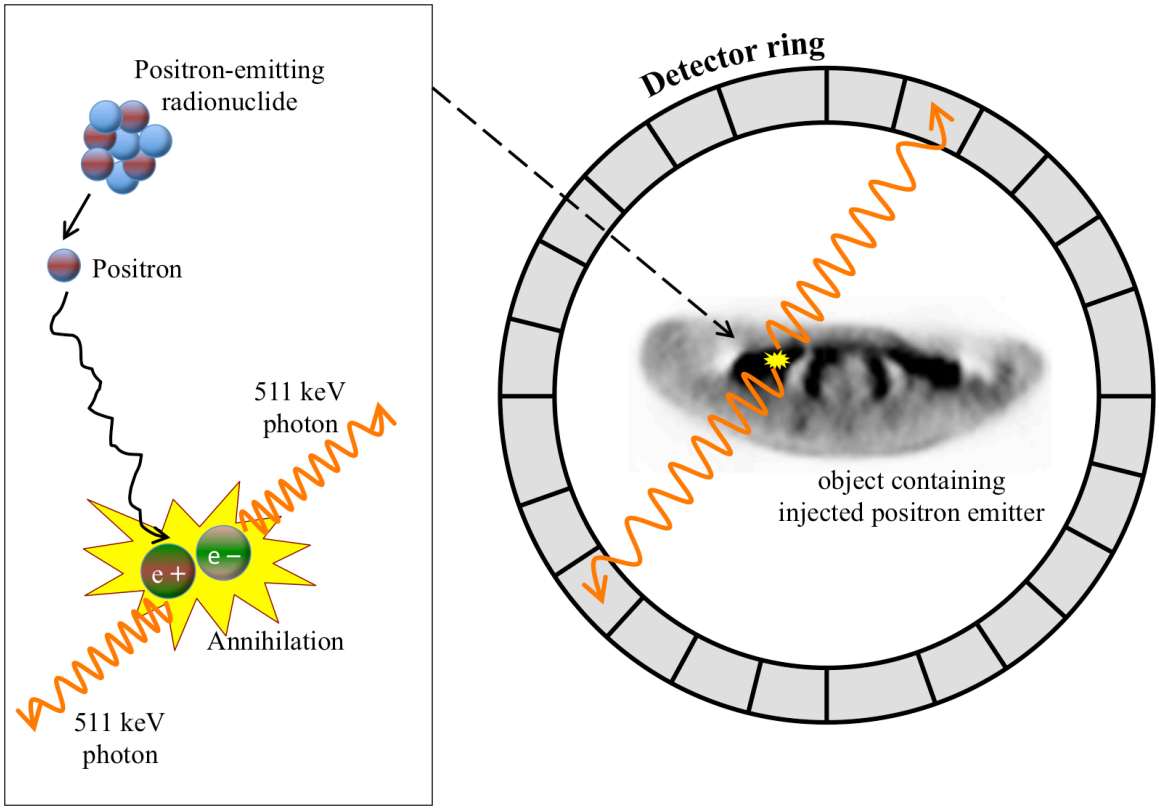

Figure 1.4-1. Positron Emission Tomography schematic. The positron-emitting radionuclide injected into the subject emits a positron, which travels a short distance and interacts with an electron. The causes an annihilation event from which two 511 keV photons are emitted at approximately 180 apart. When two detectors register the photons to within 6-12 nanoseconds it is logged as a true event and the annihilation is assumed to exist along the path between the two detectors.

A very common radiotracer is ^{18}F-FDG. Along with standard glucose, cells take up ^{18}F-FDG by the Glut-1 and Glut-3 transporters. Both ^{18}F-FDG and glucose are then phosphorylated by hexokinase, turning glucose into glucose 6-phosphate and ^{18}F-FDG into ^{18}F-FDG-6-phosphate-4 (^{18}F-FDG-6-PO_4). At this stage glucose 6-phosphate continues down the glycolysis pathway, but ^{18}F-FDG-6-PO_4 becomes trapped due to the presence of the ^{18}F in the position of the normal hydroxyl. Once the ^{18}F isotope decays it turns into oxygen-18, allowing the molecule to be metabolized in the same manner as normal glucose. The phosphorylation of glucose is proportional to the metabolic rate of a cell; therefore cells with a higher metabolic rate will take

up glucose and consequently more ^{18}F-FDG. The increased glucose demand of active BAT combined with the relatively long half-life of the ^{18}F isotope (110 minutes), makes ^{18}F-FDG an attractive radiotracer for imaging active BAT.

PET imaging is inherently quantitative, and the most widely used quantified parameter from a PET scan is the standardized uptake value (SUV). The SUV of a PET image is calculated on a pixel-by-pixel basis as follows:

$$SUV = \frac{(pixel\ value) * (subject\ weight\ [grams])}{actual\ activity} \quad [1.4\text{-}1]$$

where $(pixel\ value)$ is the stored value in the digital imaging and communications in medicine (DICOM) file for the given pixel location, and:

$$actual\ activity = (PET\ tracer\ activity) * \frac{-time\ elapsed}{2^{(PET\ tracer\ half-life)}} \quad [1.4\text{-}2]$$

and:

$$time\ elapsed = (scan\ time) - (injection\ time)\ [minutes] \quad [1.4\text{-}3]$$

The quantity $(PET\ tracer\ activity)$ is the radionuclide total does, the value of which can be obtained from the image meta-data in the DICOM header file. If the entire injected dose of FDG remained in the body and became uniformly distributed, then the SUV everywhere would be 1 g/ml. With the assumption that 1 ml of tissue weighs 1 g, SUV values would be unitless.

However, because 1 ml of tissue does not always weigh 1 g, it is more appropriate to use the units of [g/ml] for SUV images.[127] There are several additional assumptions made regarding the calculation of SUV. These include the assumption that there is negligible free FDG in the tissue at the time of the PET scan, meaning that all the FDG was taken up by tissue and can therefore be quantified as the uptake value. Also the assumption is made that all tissues are affected in the same way by glucose levels. Furthermore, tissue uptake of FDG may not plateau at same rate in different subjects, meaning that the maximum FDG may not be reached in the same timeframe. Similarly, subjects were scanned at different times post injection, typically varying within 20 minutes of each other, so variation in uptake period could cause variation in SUV.[128] A few healthy tissue SUV levels measured from ^{18}F-FDG PET scan are listed in Table 1.4-1 (data are presented as median ± range).[129]

Table 1.4-1. SUV levels of healthy tissue measured by ^{18}F-FDG PET scans. Data are presented as median ± range.

Tissue	SUV mean
Myocardium	5.86 ± 4.33
Liver	2.55 ± 0.44
Subcutaneous WAT	0.28 ± 0.11
Bone marrow	1.69 ± 0.49
Lung	0.42 ± 0.12
Blood pool	2.02 ± 0.33
Psoas muscle	0.74 ± 0.17

The spatial resolution of PET imaging is limited by several factors. First, the emitted positron does not interact with an electron immediately, but travels some distance during which time the positron loses kinetic energy.[130] The distance traveled depends on the isotope and on both initial energy and tissue density, and for ^{18}F the distance in soft-tissue is approximately 0.64mm.[126] Therefore the annihilation will occur some distance away from the decay event. The second factor affecting resolution is the noncollinearity of the two emitted photons. When the annihilation event occurs residual momentum can cause the two photons to not release exactly 180° apart. Therefore, the position of the two photons detected on opposite sides of the detector ring is slightly out of alignment. The typical size of a human whole body PET scanner results in a loss of resolution on the order of 1-2 mm. The third factor affecting resolution is Compton, or incoherent scattering. During Compton scattering the photon interacts with an electron causing the photon to loose energy and scatter in a new direction. These three factors are illustrated in Figure 1.4-2.

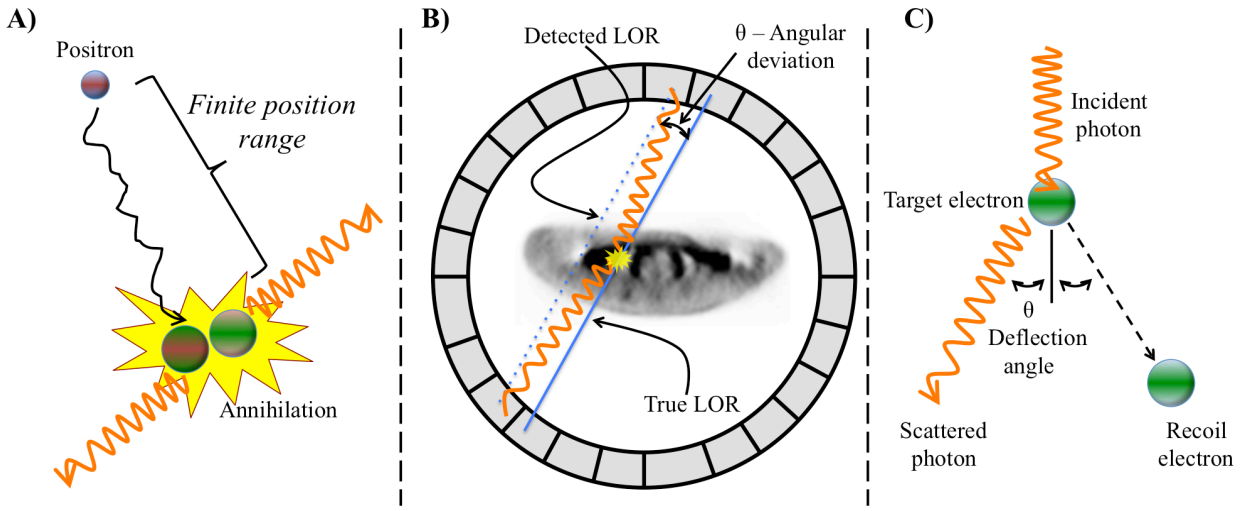

Figure 1.4-2. Three factors influencing the resolution capability of PET imaging: A) Finite position range: the emitted positron travels a distance prior to interacting with an electron, B) noncollinearity: when the positron and electron interact, the residual momentum is transmitted to

the photons, causing a deviation from 180° (θ), C) Compton scattering: the photon emitted after the annihilation event interacts with an electron in its path, causing the photon to loose energy and deflect to a new direction.

Additionally, contrast (C) between two tissues, A and B in an image arises from a difference in measurement between the two tissues, and can be expressed as:

$$C = \frac{A - B}{A} \qquad [1.4\text{-}4]$$

With ^{18}F-FDG PET imaging the difference in measurement is the direct result of the accumulation of ^{18}F-FDG in the tissue. Therefore, contrast only exists between tissues if the two tissues metabolize different amounts of glucose. This causes a problem for imaging BAT, as the glucose metabolism of inactive BAT is not different than WAT. Therefore PET imaging of BAT is only useful when BAT is active and the glucose metabolic rate is higher.

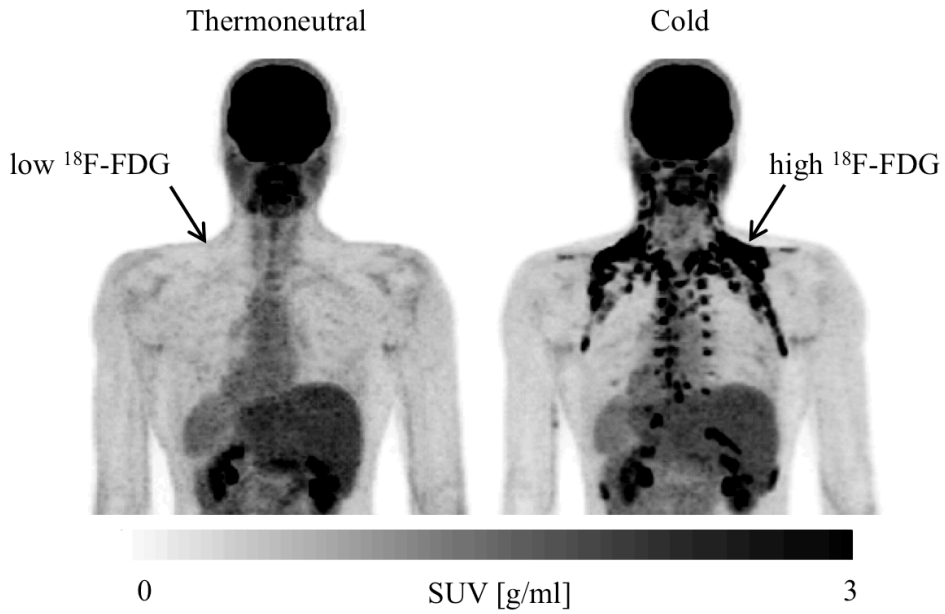

Figure 1.4-3. Coronal PET maximum intensity projection images from a thermoneutral and cold scan, displayed in inverted gray scale. The clavicular regions of increased ^{18}F-FDG uptake (arrow, cold scan) are not visible in the thermoneutral scan (arrow, thermoneutral scan).

1.4.2 Computed Tomography

Although ^{18}F-FDG PET imaging contributes important information on the glucose metabolism of BAT, spatial certainty and tissue distinction are also necessary to detect and quantify BAT. Because of this lack of tissue distinction in PET imaging, it was not until 2001 when CT combined with PET that identifying BAT was possible.

Computed tomography, or CT, imaging is based on x-ray imaging. CT employs a beam of x-rays, or high-energy photons, which are targeted at the object to be imaged. Located in a ring around the object is a series of digital x-ray detectors connected to a computer (Figure 1.4-4). The beam source then rotates quickly around the object and the x-ray detector on the opposite side of the object from the source measures the x-rays as they leave the object. Each time a full rotation is completed, the computer reconstructs the measured signal from the x-ray

detector to create a 2-dimensional image slice of the patient, typically ranging from 1-10 mm. The object is then moved incrementally past the detector and another circuit is completed. In this manner slices can be built up to create a three-dimensional image of the object.

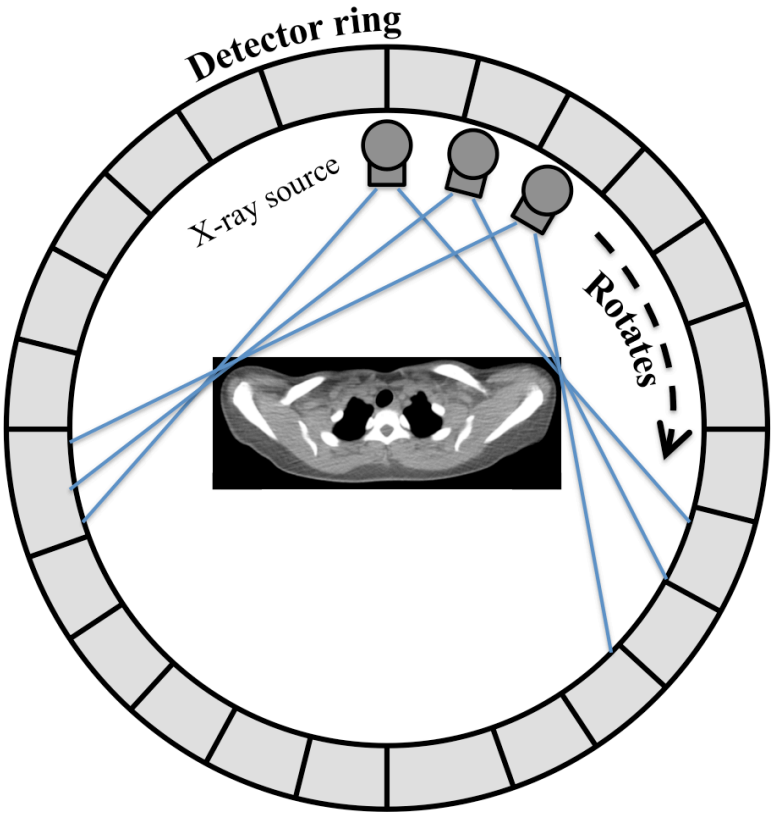

Figure 1.4-4. Computed tomography imaging schematic.

CT imaging is based on quantifying the attenuation of the x-rays as they pass through the object. As the x-ray photons pass through the object, they get absorbed, which results in less energy; this process is known as attenuation. The photons are dissipated either through the photoelectric effect or Compton scattering. The photoelectric effect occurs when a photon interacts with an electron and all the energy is used to eject the electron from the atom. No photons are released from this event. The second method of photon interaction, Compton

scattering, was described previously. Contrast in a CT image is therefore the result of photoelectric absorption and the electron densities of different types of material.

Calculation of the attenuation for a given voxel *i* in an image is performed as follows. The detector-measured intensity (N_1) of the x-ray after traveling through one voxel is given by:

$$N_1 = N_0 e^{-(w_1 \mu_1)} \quad \text{[1.4-5]}$$

where N_0 is the initial x-ray intensity, w_1 is the x-ray path length through the voxel, and μ_i is the attenuation coefficient of the material in the voxel. Therefore, the detector-measured intensity (N_i) of the x-ray after traveling through N voxels is given by:

$$N_i = N_0 e^{-(w_1 \mu_1)} e^{-(w_2 \mu_2)} e^{-(w_3 \mu_3)} \dots\dots e^{-(w_n \mu_n)} \quad \text{[1.4-6]}$$

Then, by dividing both sides by N_0 and multiplying by -1, taking the natural logarithm of each side together with the rule that the product of exponential functions is equal to the sum of exponents, this results in the following:

$$-\ln \frac{N_i}{N_0} = w_1 \mu_1 + w_2 \mu_2 + w_3 \mu_3 + \cdots\cdots w_n \mu_n \quad \text{[1.4-7]}$$

The left side of Equation [1.4-7] is the resulting measurement, termed X_i, and each $w_n \mu_n$ term represents the attenuation within a voxel *i*, which can be simplified as u_i, resulting in the following simplified equation:

$$X_i = u_1 + u_2 + u_3 + \cdots + u_n \quad [1.4\text{-}8]$$

Therefore, by collecting views from multiple angles around the object, it is possible to measure the value through the same pixel multiple times. Doing so enables back-calculation of the unknowns in each voxel. The convention is to translate the calculated attenuation with an integer value, called Hounsfield Units (HU), calculated as follows:

$$CT\ HU = \frac{K(u_{voxel} - u_{water})}{u_{water}} \quad [1.4\text{-}9]$$

Here, u_{voxel} is the calculated attenuation, u_{water} is the attenuation of water and equals 0 by convention, and K is an integer constant of 1,000.[131] Hounsfield Units are named after Sir Godfrey Hounsfield, an English electrical engineer who shared the Nobel Prize in Physiology or Medicine in 1979 with Allan McLeod Cormack, for his part in developing the x-ray computed tomography technique. Typical HU values of healthy tissue are listed in Table 1.4-2, and Figure 1.4-5 shows a representative axial slice of a CT image.

Table 1.4-2. Hounsfield Units of healthy tissue.

Tissue	HU Value
Air	-1,000
Lungs	-500
Adipose tissue	-100
Water	0
Kidney	+30
Liver	+50
Cancellous bone	+700

Figure 1.4-5. Coronal CT slice through the head and abdomen of an adult. This image displays the range of HU values present in CT images, for example, between adipose tissue and bone.

Because the attenuation through different tissues can vary significantly, the tissue contrast and therefore anatomical distinction between soft and hard tissues such as muscle and bone in CT images can be high. Because of these differences it is relatively easy to distinguish between BAT and surrounding tissues such as muscle or bone, regardless of BAT's activation status. However, the ability to distinguish soft tissue contrast is more dependent on the signal-to-noise ratio (SNR) and contrast-to-noise ratio CNR, and may require a high dose CT scan to clearly distinguish between soft tissues with similar attenuation coefficients. Thus the difference in attenuation through inactive versus active BAT is not as drastic without higher dose CT scans.

When BAT is activated over a short period of time it is characterized by an increase in blood flow,[132,133] which would raise the HU value of BAT (making it less negative). If activated over a long period of time, activated BAT begins to deplete the lipid vacuoles, reducing the amount of fat in the adipose tissue.[44,101] This would also raise the HU value of BAT. Therefore, causing BAT to be active for the short periods of time characteristic of typical human studies

would result in a lower contrast between the active and inactive states as measured using CT HU values than that as measured by PET SUV-values.

1.4.3 Magnetic Resonance Imaging

MRI was developed in the 1970s around the same time as PET, and used as early as 1989 to study BAT in laboratory rodents. This early work with rodents demonstrated the ability for MRI to not only distinguish BAT from WAT,[134,135] but also the difference between the BAT of warm-housed and cold-acclimated rats.[136] A few years later, research was performed using magnetic resonance spectroscopy (MRS) to acquire spectra of interscapular BAT, periepididymal WAT and leg muscle tissue of rats.[137] In these samples, the water-proton percentage was roughly 46%, 20% and 99% in BAT, WAT and muscle respectively. This is possibly the earliest work quantifying the water content of BAT and WAT using MRS. However, perhaps because MRI is not as widely utilized clinically nor is the data as easy to acquire and analyze as PET-CT, it was not until recently that MRI began taking root as a promising primary method for detecting and quantifying human BAT.

Unlike PET and CT, MRI does not rely on ionizing radiation to produce images. Instead, MRI relies on how nuclei respond to absorbed radio frequencies. Additionally, the image formed by MRI is influenced by factors such as how the absorbed energy is re-emitted, called relaxation, and the movement of the nuclei out of or into the imaged plane, called flow. In addition to the anatomical information contained in an MR image, MRI can measure the variations in molecular electron distribution providing chemical information as well. It is this combination of anatomical and chemical information, along with the versatility of MRI that makes MRI such a powerful modality.

MRI systems utilize three types of magnetic fields to generate signal: a strong static main magnetic field (B_0) with units of Tesla (T), electro-magnetic radio frequency (RF) fields, and linear gradient fields. The main magnetic field aligns with the bore of the MRI machine, and by convention is called the z-axis or the longitudinal axis. When placed in a strong external magnetic field (for example, B_0) the hydrogen protons align along B_0 (Figure 1.4-6) and resonate with a precise frequency called the Larmor frequency, which is directly dependent on the strength of B_0:

$$\omega = \gamma B_0 \qquad [1.4\text{-}10]$$

Here ω is the Larmor frequency (in Megahertz), γ is the gyromagnetic ratio (42.57 MHz/T for H^1) and B_0 is the external magnetic field (in Tesla).

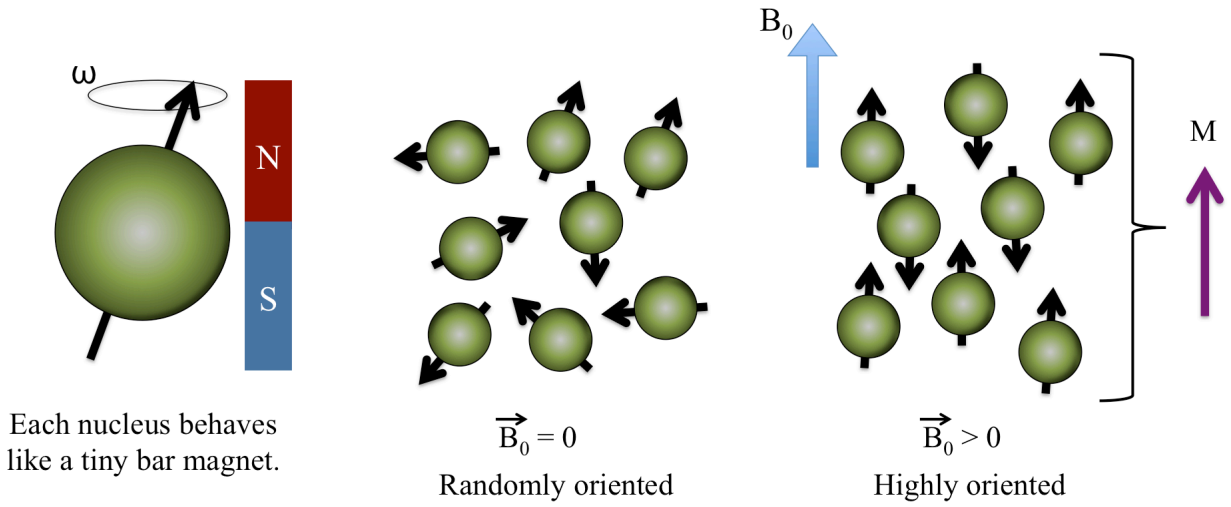

Figure 1.4-6. ^1H nuclei behave like tiny bar magnets. In the absence of an external magnetic field ($B_0 = 0$), the nuclei are randomly oriented. However, in the presence of an external magnetic field ($B_0 > 0$), the nuclei align themselves along B_0, either parallel or antiparallel. The sum of all the individual nuclei result is called the net magnetization, M.

However, to detect information from the nuclei, they must be perturbed away from their alignment with B_0, as seen in Figure 1.4-7. This is achieved through the use of a time-varying RF pulse, called $\overrightarrow{B_1}(t)$, applied perpendicular to B_0 and matching the Larmor frequency of the nuclei of interest:

$$\overrightarrow{B_1}(t) = B_1 \begin{bmatrix} \cos(\omega_{RF} t) \\ -\sin(\omega_{RF} t) \\ 0 \end{bmatrix} \quad [1.4\text{-}11]$$

Here ω_{RF} is the frequency of the applied RF field $\overrightarrow{B_1}$, where the magnitude B_1, is typically in fractions of a Gauss. Applying the RF pulse causes the protons to deflect away from B_0, synchronizing and rotating in phase about B_1 towards the x-y plane. This angle of rotation about $\overrightarrow{B_1}$ is called the RF flip angle (α), Figure 1.4-7-B, and is described by:

$$\alpha = \gamma \overrightarrow{B_1} t \quad [1.4\text{-}12]$$

where t is the duration of the RF pulse.

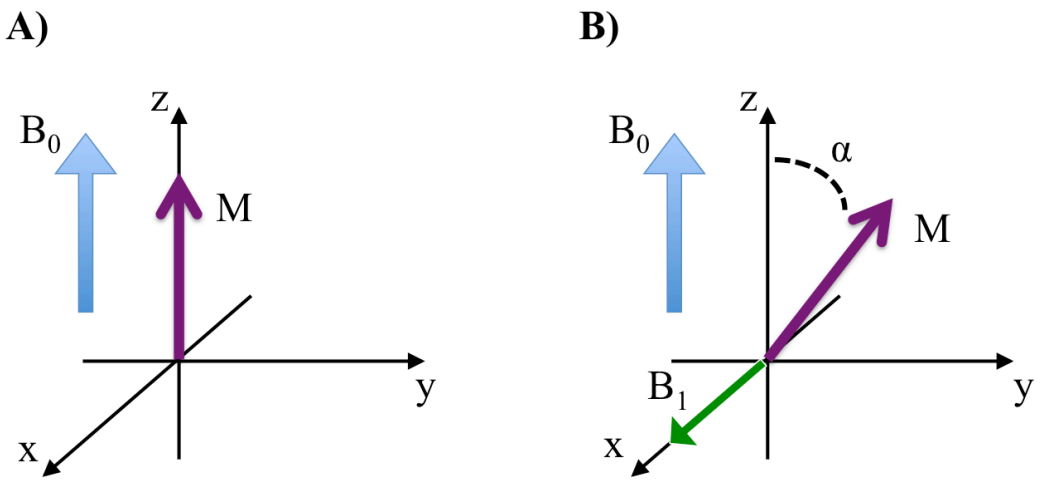

Figure 1.4-7. As seen in **Figure 1.4-6**, in the absence of other forces, the net magnetization (M) aligns along B_0 **(A)**. When the RF field (B_1) is applied perpendicular to B_0, this causes M to rotate about B1 by an angle ***α*** **(B)**.

After this excitation, the protons re-emit the absorbed RF energy in a process called relaxation. Relaxation occurs in two ways: longitudinal and transverse relaxation. Longitudinal relaxation occurs when the excited protons interact with the surrounding molecular lattice thereby releasing energy. This causes the bulk magnetic moment of proton nuclei to return to equilibrium in an orientation along B_0, characterized by the value T_1, as seen in Figure 1.4-8-A. T_1 is the time required for the net magnetization to return to 63% of the original value, prior to excitation. Transverse spin-spin relaxation is the result of the transfer of energy between excited protons in different energy states. This causes the protons to gradually de-phase, characterized by T_2, the time required for the transverse magnetization to decrease to 63% of its original value, as seen in Figure 1.4-8-B.

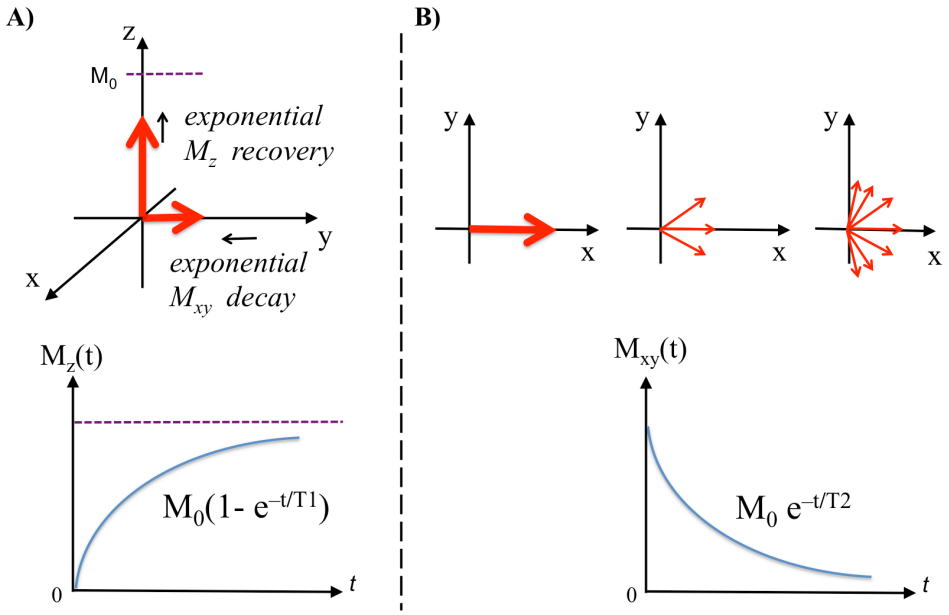

Figure 1.4-8. After the application of the RF pulse, as in **Figure 1.4-7**-B, two forms of relaxation occur: 1- longitudinal relaxation, governed by T_1, causes M to "relax" back to equilibrium **(A)**, 2- transverse relaxation, governed by T_2, causes the spins in the transverse plane to dephase **(B)**.

The precessing transverse signal induces an electrical signal received by the RF coil. The changes in the induced current correspond to changes in the transverse magnetic moment over time, and the decay of the signal is called the free induction decay (FID). The FID decays at a rate called T_2*, a time constant related to both T_2 relaxation and magnetic field (B_0) inhomogeneities.

1.4.3.a) Fat-Water MRI

The majority of the MRI work presented here is based on a method called fat-water MRI, or FWMRI. FWMRI is a method that separates the MRI signal from water and fat based on chemical shift encoding. MRI primarily detects signal generated from protons, which are either part of water, or molecules such as proteins, carbohydrates, or fat. Nuclei of different molecules

with different numbers of electrons experience variations in an effect called electron shielding, which results variations in the effective magnetic field experienced by the nucleus. The electron shielding felt by protons in water is less than that of protons in triglyceride molecules of fat. This causes the proton resonance frequencies to be different between water and fat. Furthermore, the protons in triglyceride molecules do not all experience the same electron shielding, and therefore fat is better described by multiple frequencies. The chemical shift of the resonance frequency, Δf_{cs} is related to B_0 as:

$$\Delta f_{cs} = \gamma B_0 \Delta\delta[ppm] \cdot 10^{-6} \quad [1.4\text{-}13]$$

where γ is the gyromagnetic ratio. At 3T, the main fat protons resonate 420 Hz more slowly than water (Figure 1.4-9). However, the resonance frequency of water is temperature dependent, which can cause the apparent chemical shift between fat and water to change based on temperature. The temperature dependence will be explored further in Section 1.4.3.b).

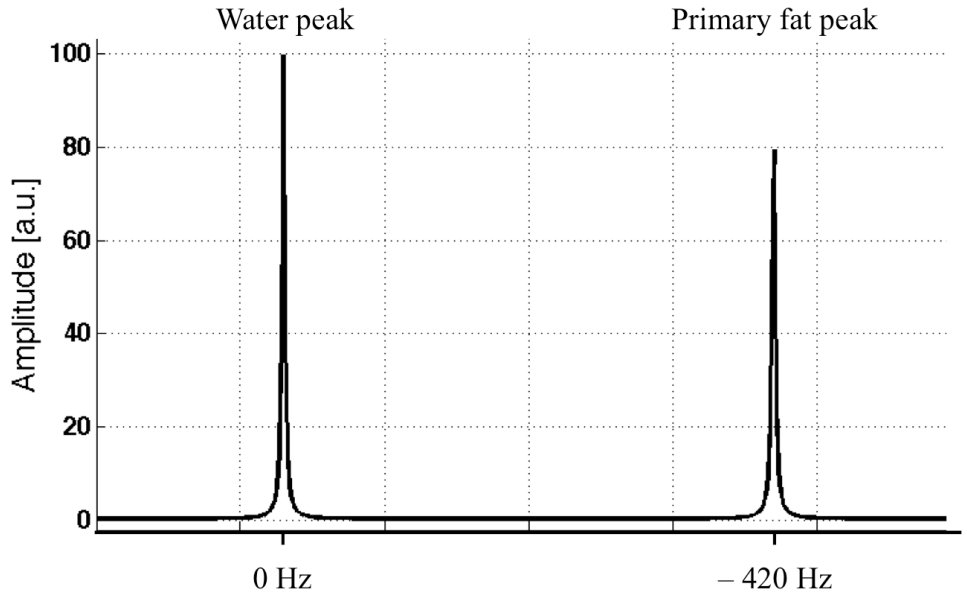

Figure 1.4-9. Chemical shift in frequency of fat to water at 3 Tesla.

This difference in frequency between water and fat creates a phase shift, which can be encoded by acquiring images at different echo times (TE). A simplistic model of the signal $Y(t)$ from water and fat in a voxel as a function of time t is given by:

$$Y(t) = W + Fe^{i\omega_B t} \quad \text{[1.4-14]}$$

where W and F are the water and fat signals respectively at time $(t = 0)$, and $\omega_B = \gamma B_0 - (\delta_B - \delta_W)$ is the difference in resonance frequency between water and fat due to the chemical shift. This enables the signal from water and fat to be separated, resulting in an image based primarily on water protons and another based on fat protons.

The first chemical shift based separation of water and fat images was performed by Dixon in 1984.[138] The original Dixon technique is based on the simplification that the spectral dimension is only sampled at two key points: one where the fat and water resonances are in-phase and one where the water and fat are 180 degrees out of phase. This generates an in-phase (IP) image, where the voxel intensity is proportional to the addition of the transverse magnetization of both the water and fat components, and an out-of-phase (OP) image, where the voxel intensity is proportional to the difference between the water and fat transverse magnetization.

$$\begin{aligned} Y_{IP} &= W + F \\ Y_{OP} &= W - F \end{aligned} \quad \text{[1.4-15]}$$

Therefore, adding the in-phase (IP) and out-of-phase (OP) images results in a water image, while subtracting the OP image from the IP image results in a fat image[138].

$$W = \frac{Y_{IP} + Y_{OP}}{2}$$
$$F = \frac{Y_{IP} - Y_{OP}}{2} \qquad \text{[1.4-16]}$$

Example MR fat and water images are displayed in Figure 1.4-10. Dixon imaging assumes the image phase is only due to chemical shift, however local variations in the field can also produce phase errors causing the water and fat signals to be confused and "leak" into the opposing image. A few approaches to correct for these difficulties include increasing the number and timing of the spectral samples, using a more accurate signal model, and algorithms to correct for phase errors.

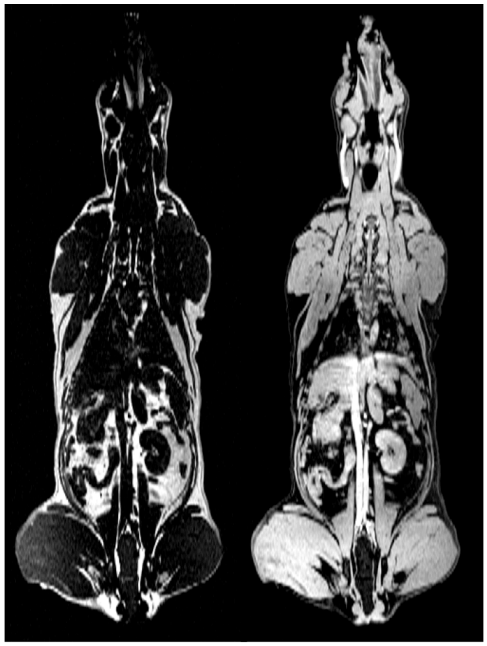

Fat Water

Figure 1.4-10. Magnetic Resonance fat-water separated coronal images of a Canine.

To adjust for the off-resonance effects caused by B_0 inhomogeneities, the signal equation is adjusted to include an unknown frequency ω that varies from voxel to voxel:

$$Y(t) = (W + Fe^{i\omega_B t})\, e^{i\omega t} \qquad [1.4\text{-}17]$$

In this equation W and F are the water and fat signals at $(t = 0)$, and the frequency $\omega_B = \gamma B_0(\delta_B - \delta_W)$ is the difference in resonance frequency between water and fat due to chemical shift. Dixon's original 2-point method did not include the $e^{i\omega t}$ term because the absolute value of the IP and OP images were used[138]. However, this approach only applies when the signal from water is greater than the signal from fat. This is not always the case in a given voxel; for example it is not the case in subcutaneous WAT, which contains more fat than water.

Estimating ω in each voxel produces a map of the inhomogeneity in the main magnetic field (B_0),[139,140] and acquiring data at additional echo times simplifies the estimation of ω.[140] Additionally, Eq. [1.4-17] assumes no relaxation occurs, which can only be approximated for $t \ll T_2^*$. Incorporating T_2* into the signal equation produces a more accurate estimation of water and fat, while also providing a T_2* map of the acquired image, and the equation becomes:

$$Y(t) = (W + Fe^{i\omega_B t})\, e^{(i\omega - R_2^*)t} \qquad [1.4\text{-}18]$$

where $R_2^* = \frac{1}{T_2^*}$ and here is assumed equal for water and fat. Because of the increase in the number of nonlinear terms to be estimated in each voxel, T_2* can only be estimated if more than 3 spectral samples are acquired.

Another approach to correct for errors in the water-fat separated images is to use a fat spectral model with more than one peak. So far the assumption has been made that all fat can be estimated by a chemical shift of 1.3 ppm; however, this is only valid for approximately 60% of fat protons. An example of a 9-peak fat spectrum is illustrated in Figure 1.4-11. Because fat is more accurately modeled with multiple peaks it is beneficial to use a signal model that accounts for multiple fat resonances:

$$Y(t) = (W + F\sum_{m=1}^{M} \alpha_M\, e^{i\omega_M t})\, e^{(i\omega - R_2^*)t} \qquad [1.4\text{-}19]$$

Here the fat protons are assumed known *a priori* to exist at M resonances with frequencies $\omega_m = \gamma B_0(\delta_m - \delta_W)$ and relative amplitudes α_m.

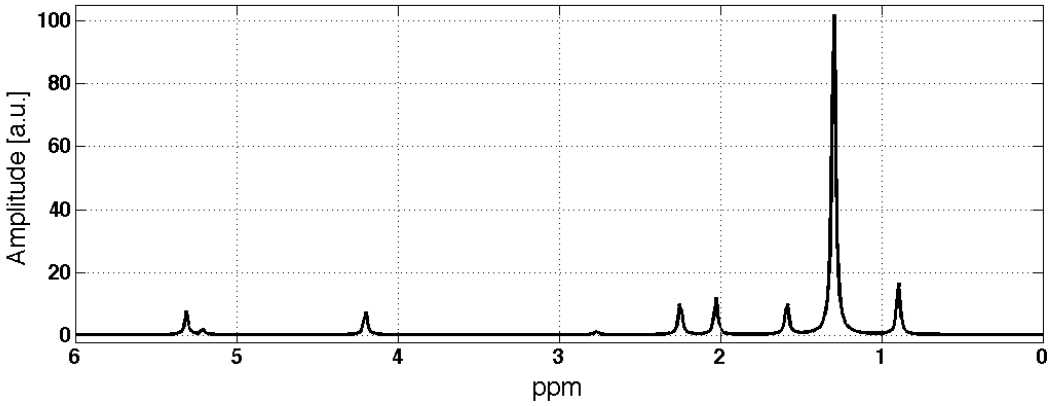

Figure 1.4-11. 9-peak fat spectrum model.

Using multiple fat resonances increases the accuracy of the model and results in more accurate estimation of the water and fat signal.[141] The research presented in this dissertation utilizes two fat spectral models, a 6-peak[142,143] and a 9-peak[144] model. These two fat spectral models will be explained and elaborated in Section 2.4.1.

In the work presented here, we aim to characterize two primary results from FWMRI scans: fat-signal fraction (FSF) and the transverse signal decay rate (R_2*). The first of these, FSF, is calculated from the water and fat separated images, which result from solving Eqn. [1.4-19]. The fat-water separation method used in this work will be further described in Section 2.4.1. The FSF image is calculated as:

$$FSF = \frac{Fat}{Water + Fat} \qquad [1.4\text{-}20]$$

in voxels where the signal is greater in the fat image (fat dominant), and

$$FSF = 1 - \frac{Water}{Water + Fat} \quad [1.4\text{-}21]$$

in voxels where the signal is greater in the water image (water dominant). FSF is calculated in this manner to reduce the effect of noise bias.[145] The resulting image pixel values are $0 \leq FSF \leq 1$, which in this work has been scaled by 100 to result in units of percent [%]. This results in a quantitative measure of the relative fraction of signal arising from fat protons.[146] An example coronal FSF image of a human female can be seen in Figure 1.4-12.

FSF is therefore a useful method for quantifying the difference between BAT and WAT because, as discussed earlier, brown adipocytes contain less fat and more water than white adipocytes. Hence, we would expect the FSF of BAT to be a lower percent than the FSF of WAT. Indeed, previous work shows that in mice interscapular BAT ranges from 40-80% FSF, while gonadal WAT ranges from 90-93% FSF.[147] Additionally, humans aged 5-26 years also show a FSF of 39.2-80.6% FSF in clavicular BAT and a range of 87.4-96.0% FSF in subcutaneous WAT.[148]

The second FWMRI characteristic of interest is transverse signal decay rate, (R_2*), related to T_2* relaxation time as: R_2* [s^{-1}] = 1000/T_2* [ms] and is also a result from solving Eqn. [1.4-19]. An example coronal R_2* image of a human female can be seen in Figure 1.4-12. Activated BAT is associated with increased perfusion,[6] and in turn, the increased blood flow supports the increased metabolism of BAT.[149] T_2*-weighted signal is sensitive to perfusion due to the blood oxygenation level-dependent (BOLD) effect. As the concentration of deoxyhemoglobin decreases in perfused vessels, it causes an increase in signal. Previously, T_2*-weighted imaging has been used to map perfusion in the brain[150] and skeletal muscle.[151] Additionally, work in mice shows a decrease in T_2*-weighted image signal intensity of the

interscapular BAT depot after activation by injection of norepinephrine.[152] In this work Khanna et al. associate the shortening of T_2* in activated BAT to an increase in oxygen consumption. Unlike what occurs in the brain, Khanna et al. hypothesized that activated BAT is not sufficiently compensated by an increase in blood flow, resulting in completely deoxygenated blood. Therefore, an increase in paramagnetic deoxyhemoglobin results in faster decay of the MR signal. Additionally, the R_2* value in BAT is of interest because previous work shows it may reflect tissue iron content.[153–155] Because BAT has a higher iron content than WAT due to the elevated mitochondrial presence and dense blood vessel innervation, it is possible that the R_2* could show differences between the two tissues. This has been shown to be true in infants and adolescents, where the R_2* of supraclavicular BAT ranges from 39-84 s^{-1}, and subcutaneous WAT ranges from 22-40 s^{-1}.[148,156]

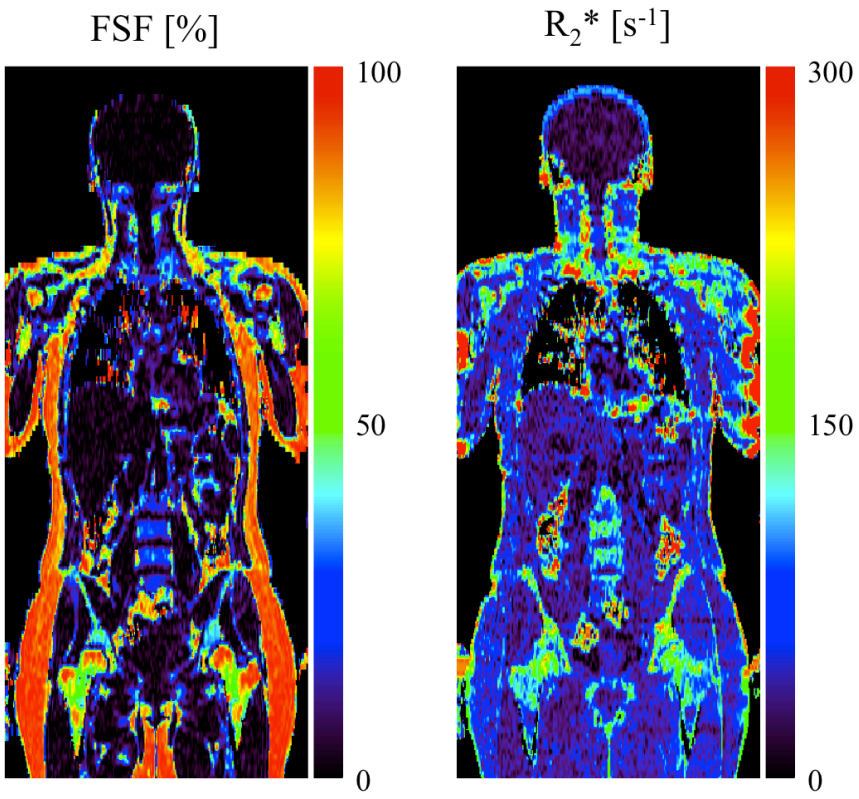

Figure 1.4-12. Coronal images showing the MRI-derived fat-signal fraction (FSF [%]) and transverse signal decay (R_2* [s^{-1}]) in an adult female subject.

1.4.3.b) Internally-Referenced MRI PRF Temperature Mapping

One of the hallmark characteristics of BAT is that it releases heat when active.[5] Therefore, while FSF and R_2* may be able to distinguish between BAT and WAT, the ability to quantify the temperature of tissue could provide a clear distinction between active and inactive BAT. The MRI-based temperature mapping method used in this work takes advantage of the fact that water undergoes a chemical shift due to temperature while fat does not. This is useful because both water and fat are present in BAT, meaning that fat can be used as an internal reference for quantifying the chemical shift of water due to temperature.

Nuclei of different molecules with different numbers of electrons experience variations in an effect called electron shielding, which results in variations in the effective magnetic field experienced by the nucleus. Therefore, as discussed in the previous section, in addition to spatial information the MR signal also contains information about the chemical environment. The units of chemical shifts are denoted in parts per million [ppm], and the ^{1}H nuclei of water molecules have a chemical shift of approximately 4.7 ppm at body temperature. This chemical shift of water is however, also dependent on temperature. The hydrogen bonds of water molecules effectively pull the electrons away from the protons, resulting in a higher resonant frequency. However, if the temperature increases the hydrogen bonds stretch causing the electrons to pull closer to the protons and resulting in an increased electron shielding effect. This reduces the effective magnetic field felt by the protons and the resonant frequency decreases. The temperature-based shift in the frequency of water is $P_c = 0.01\ ppm/°C$, and has been shown to be linear in the temperature range pertinent to biological application. This technique of temperature mapping is called proton resonant frequency shift (PRF) thermometry, and typically uses the change in phase from a series of images to calculate the temperature. However, because protons on lipids do not experience the same shift in temperature-based shift in frequency, the resonant frequency of fat can be used as a reference, as seen in Figure 1.4-13.

The following equation captures the employed model for the voxel-by-voxel MR signal as a function of time:

Modifying Eqn. [1.4-19] enables solving for the temperature-dependent frequency shift of water (Δf_T) in addition to the previously obtained water, fat and R_2* values.

$$Y(t) = (We^{i2\pi\Delta f_T t} + F\sum_{m=1}^{M} \alpha_M\, e^{i2\pi\Delta f_M t})e^{i\varphi}\, e^{(i2\pi\Delta f_{B0} - R_2^*)t} \qquad [1.4\text{-}22]$$

Were Δf_T is the temperature dependent frequency shift, W and F are the water and fat magnitudes, respectively, with complex phase φ. Again α_M and Δf_M are the amplitude and frequency of the m^{th} fat spectral peak, respectively, and Δf_{B0} is the background field off-resonance term, and R_2^* is the shared signal decay rate for both water and fat.

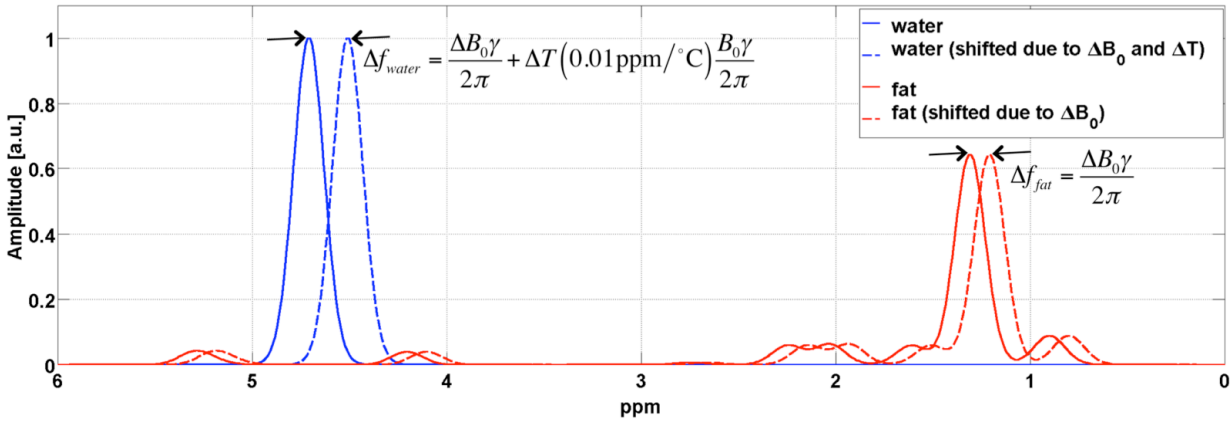

Figure 1.4-13. Frequency shift of water (shifted due to ΔB_0 and ΔT) and fat (shifted due to ΔB_0, only).

Convention dictates that higher frequencies are presented to the left, and frequencies decrease along the x-axis to the right. Each resonance corresponds to a line in the spectrum. The lines have width due to T_2* decay, giving a Lorentzian line shape to each peak, and the area under the line is proportional to the number of nuclei with that given frequency.

1.5 Summary

The research presented in this dissertation aim to apply the principles of imaging to measure the biological properties of BAT, focusing on advancing the understanding of MRI-derived characteristics of BAT in adult humans. The quantitative MRI-derived FSF measurement is characterized, demonstrating that MRI is a promising imaging modality to provide morphological information of BAT, and is a potential alternative to CT. By capitalizing on the biologic properties of BAT that make MRI-derived temperature mapping possible, work which demonstrates MRI as a promising alternative to PET for detecting the activation of BAT is also presented.

CHAPTER 2

STUDY DESIGN

When the study design for this research began to take shape, few prospective studies on healthy adult subjects had been published at the time, and none that used MRI. Consequently no consensus points existed on which to base the methods of this research. At the start of this research only two years had passed since the scientific community accepted the indisputable proof that the uptake of ^{18}F-FDG seen in PET scans was due to BAT.[12–14] These three studies by Saito et al.,[12] Virtanen et al.,[13] and van Marken Lichtenbelt et al.[14] each used two hours of exposure to a set temperature to either induce BAT activation or to keep BAT inactive, though the temperatures varied in each study (16-19°C (cold), and 22-28°C (warm)). It was not until after our research began that the idea to utilize individualized cooling methods was published.

Furthermore, there was no standardization on how to define regions of BAT in PET-CT images, as the two studies that presented unequivocal evidence of BAT did not specify the image-based rules (SUV and HU limits) by which they defined BAT.[12,14] Over the next three years the principally cited method for delineating BAT was published by Cypess et al. in 2009.[157] In the research by Cypess et al. the PET-CT scans of 1,972 patients were retrospectively analyzed using the following rules used to define BAT: SUV > 2.0 g/mL, and -250 to -50 HU. Then in 2011 Ouellet et al.[158] published a retrospective study on 4,842 patients, using a different set of BAT-definition rules: SUV > 1.0 g/mL, and -100 to -10 HU. It is from these publications that the basis for the formation of the rules used to delineate BAT as described in this dissertation, were based. To this day there is no standardization of how to demarcate BAT based

on SUV and HU values, with published values ranging from 1.0 to 2.5 SUV,[16,159] and -300 to -10 HU.[11,160]

The study design used in performing the research presented here was based on those limited published studies. Since the start of this project tremendous volumes of research have been published and much has been learned regarding BAT, however there is still much to be studied with respect to BAT in humans.

2.1 Subject Enrollment

The local ethics committee of Vanderbilt University approved this study, and all subjects provided written informed consent prior to participation. Twenty-five healthy adult human subjects were recruited for the study. To be eligible for the study, subjects were screened for the following exclusion criteria: have known diabetes mellitus, use beta blockers or anxiety medication, smoke or chew tobacco products, drink more than 4 cups of coffee each day, or more than 2 alcoholic drinks each day. Demographics for all enrolled subjects are given in Table 2.1-1.

Table 2.1-1. Subject demographics.

Characteristic	All Subjects
N (male)	25 (10)
Age (yr)	
Mean	26.7 ± 4.6
Range	21.5 – 41.1
Height (cm)	
Mean	169.5 ± 8.4
Range	153.5 – 190.0
Weight (kg)	
Mean	148.7 ± 20.2
Range	115.5 – 189.3
BMI (kg/m^2)	
Mean	23.4 ± 2.7
Range	20.2 – 31.5
Waist (cm)	
Mean	76.7 ± 5.6
Range	69.0 – 90.5

Values are presented as means ± SD. BMI: Body-mass index

2.2 Study Set-up

All participants underwent four scans: two MRI and two PET-CT, each acquired on a different day. Both scanning modalities were performed after two hours of exposure to either thermoneutral 24°C (75.2°F) or cold 17°C (62.6°F) conditions. All scans were performed in the morning, with each study day completed by 13:00. Subjects were required to refrain from alcohol, caffeine, medication and exercise or any strenuous activity for 24 hours prior to entering the temperature-controlled room, and to fast overnight (at least 8 hours). The room used as a temperature-controlled environment measured 7’ x 6’ 8” x 8’ (373.33 cu. ft.), was prepared with warm or cold air conditioning at least 60 minutes prior to subject arrival. The room was either cooled using a portable air-conditioning unit (Soleus Air LX-140, 14,000 BTU) and a rotating

floor fan, or was heated using a programmable portable rotating floor heater (Lasko 5536). The room temperature was maintained without air blowing directly on the subject.

On the PET-CT scan days the subjects first went to the PET imaging suite to have a blood sample drawn to test their fasting glucose level, and to have an intravenous (IV) port placed in a vein in the hand or arm. This port allowed the Radiology technician to more easily inject the radiotracer later, when the subject was sitting in the temperature-controlled room. If the subject was female, she also underwent a blood serum pregnancy test to ensure she was not pregnant.

Prior to entering the temperature-controlled room, subjects changed into standardized disposable hospital exam shorts and t-shirts ((MediChoice, Mechanicsville, VA, USA). Subjects also removed socks and shoes, keeping on their underwear, resulting in a total clothing insulation (clo) factor[161] of 0.19 clo (female: underwear 0.03 clo, bra 0.01 clo, shorts 0.06 clo, t-shirt 0.09 clo; male: briefs 0.04 clo, shorts 0.06 clo, t-shirt 0.09 clo). Subjects' height, weight, and waist circumference measurements were then taken after they changed into standard clothing. The subjects' body temperature was measured using a sublingual thermometer at four time points: prior to entering the temperature-controlled room, after one hour in the room, at the end of two hours in the room and after acquiring the scan (hours 0, 1, 2 and 3, respectively). Coronal thermal infrared (TIR) images of the clavicular skin were also acquired using a FLUKE TIR-125 camera at the same four time points (hours 0, 1, 2, 3). The TIR images covered the clavicular region, including the upper chest and neck, and were acquired with the subject facing the camera. On the PET-CT scan days, after the first hour in the temperature-controlled room a Radiology technician administered the injection of ^{18}F-FDG through the IV port. The injection dosage of

0.14 mCi/kg was calculated based on subject specific weight, for example a dosage of 9.8 mCi would be used for a 70 kg subject.

Once the subjects entered the temperature-controlled room they sat stationary for two hours. In the room they were allowed to read or to watch TV but were not allowed to perform any activity that could change their body temperature, i.e. exercise, or sleep. After two hours in the temperature-controlled room, the subjects were transported by wheelchair to either the MRI or PET-CT scanner. The wheelchair was used on the cold days to minimize any potential warming due to muscular activity, and on the warm days to keep the protocol consistent. On cold MRI scan days the subject put on a cold vest (Polar Products, with Cool58^{TM} packets) immediately prior to leaving the temperature-controlled room. The cold vest was necessary on cold MRI days to keep the subject cool and maintain BAT activation, but was unnecessary on cold PET-CT days. The cold vest during wheelchair transport was not needed on PET-CT days because the ^{18}F-FDG radiotracer was already taken up into the activated BAT, and the tracer would remain present in BAT even if the subject became warm while being transported to the scanner. On warm MRI and PET-CT scan days the subject was wrapped in a blanket to keep the subject warm and to reduce the likelihood of BAT activation.

2.3 Data Acquisition

2.3.1 PET-CT Acquisition

PET-CT scans were acquired on a GE Discovery See and Treat Elite (STE) PET/CT scanner (General Electric Medical Systems, Milwaukee, WI, USA) with a field of view (FOV) covering from the crown of the head to mid-thigh in 7-9 bed positions, depending on subject height (2 minutes per bed position). Scans were acquired in helical mode with a 0.8 second

revolution time, a 1.25 mm single collimation width, and a 1.675 spiral pitch factor. The reconstructed PET-CT voxel sizes were: PET: 5.5 mm x 5.5 mm in-plane, and 3.27 mm through-plane, CT: 1.37 mm x 1.37 mm in-plane, and 3.27 mm through-plane.

The subject was positioned on the bed to enter the scanner head first in a supine position. Once lying down, a small pillow was also placed under their head, and the subject placed both arms inside a bag similar to a pillowcase, and lowered their arms to either side of their body as seen in Figure 2.3-1. This helped ensure the shoulders were positioned in the same manner during each scan, which assisted in better image co-registration in later image analysis steps.

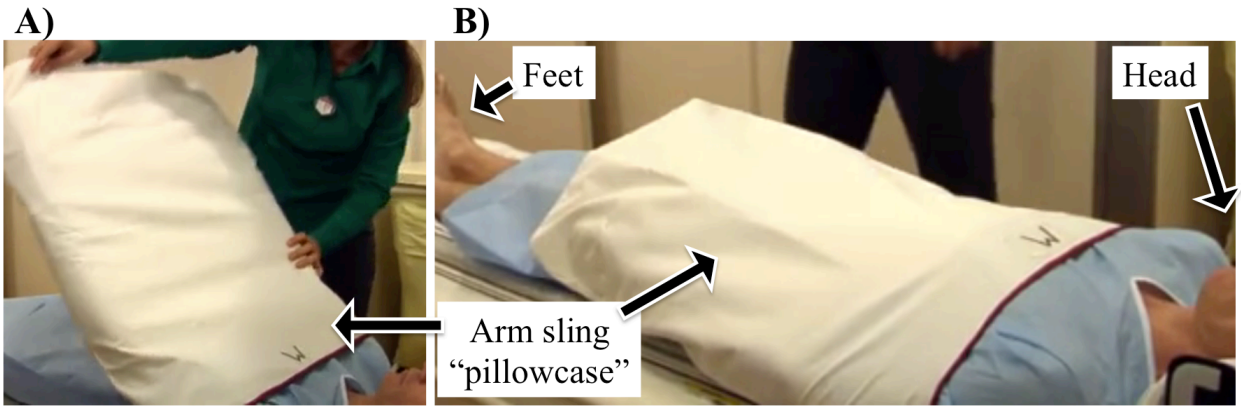

Figure 2.3-1. The "pillowcase," used to keep arms and shoulders in the same position. Placement of both arms inside the pillowcase (A); arms, inside the pillowcase, lowered to either side of the body (B).

2.3.2 MRI Acquisition

MRI scans were acquired using a Philips Achieva 3 Tesla scanner (Philips Healthcare, Best, Netherlands) equipped with two-channel parallel transmit capability, a 16-channel Torso-XL surface coil (Invivo Corp., Gainesville, Florida), and an X-tend tabletop (X-tend ApS, Hornslet, Denmark), as seen in Figure 2.3-2. The anterior portion of the Torso-XL coil hung

from the top of the scanner bore in a fabric sling. The sling was intentionally allowed to hang low enough to slide against the subject's body in order to maximize the SNR. The posterior portion of the Torso-XL coil was placed in the coil wagon between the two layers of the X-tend table (Figure 2.3-2, B). As the X-tend table moved through the scanner bore, the coil was held stationary at isocenter by straps attached to the scanner.

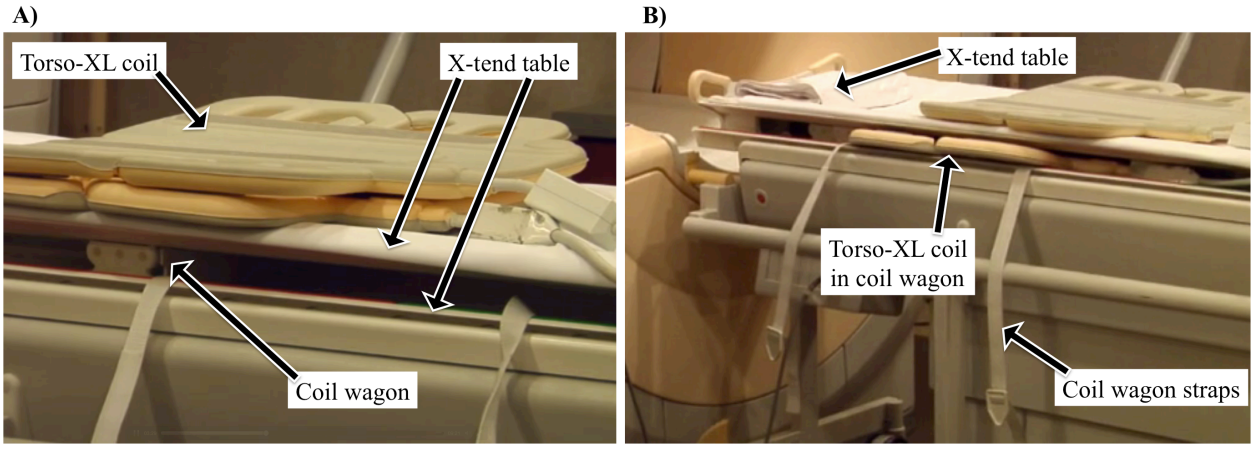

Figure 2.3-2. MRI X-tend table setup. (A) The X-tend table is made of two layers separated by a gap, in which the coil wagon exists. (B) The posterior portion of the Torso-XL coil is placed into the coil wagon between the two layers of the X-tend table. The two coil wagon straps are used to secure the coil wagon to the cover of the MR bore, thus allowing the Torso-XL coil to remain stationary while the table moves over the coil.

The subject was positioned on the bed to enter the scanner feet first in a supine position. Once lying down, the same small pillow used during the PET-CT scan was placed under their head, and the subject placed both arms inside the same pillowcase (Figure 2.3-1), and lowered their arms to either side of their body. This helped ensure that the subject was positioned in a similar manner during both the MRI and PET-CT scans, which was critical to achieve successful image co-registration in later analysis steps.

A total of six different MRI sequences were performed on each subject during the each MRI scan. These sequences are listed in Table 2.3-1. The majority of the data presented in this

work originates from the first sequence listed in Table 2.3-1, and the expanded details of this sequence are further described here. The sequence was a multi-stack, multi-slice, multiple fast field echo (mFFE) acquisition with 7 stacks of 20 contiguous axial slices. As described previously, scanner software was modified to enable the sampling of 8 echoes acquired as two interleaved sets of four echoes with TE_1=1.024 ms and effective ΔTE = 0.779 ms. The interleaved mFFE scans are denoted as imFFE. Preparation phases for each stack included center frequency (F_0) optimization and first order linear shimming. Additional acquisition details include: flip angle = 12º, repetition time (TR) = 83 ms, water fat shift = 0.323 pixels, readout sampling bandwidth = 1346.1Hz/pixel, axial in-plane field of view = 520 mm × 408 mm, acquired voxel size = 2 mm x 2 mm x 7.5 mm, and sensitivity encoding (SENSE) parallel imaging factor = 3 in the anterior-posterior direction. Acquisition time was 25 s per stack, and two breath holds were performed per station, from the neck to the pelvis. Real and imaginary images were saved for off-line processing.

Additional MRI sequences acquired for each stack prior to this 4x2-echo imFFE sequence, included: a dual angle B_1 calibration scan (acquisition time 15.1 s) acquired to enable optimized RF shimming for the two-channel transmit capability of the scanner, and a SENSE reference scan (acquisition time 12.1 s).

Table 2.3-1. MRI Scan sequences acquired.

Sequence	Voxel (mm)	Slices	Time (m:s)	SENSE	Specs
imFFE 4x2 echo	1.81 x 1.81 x 7.5	20	0:25	3	α = 12° (20°) ΔTE = 1.51 ms
HR imFFE 4x3 echo	1.0 x 1.0 x 5.0	30	5:53	1.5	α = 30° ΔTE = 2.35 ms
MFA imFFE 4x2 echo	1.48 x 1.48 x 7.5	20	2:53	3	α = [20,18,16,14,12,10,8,6,4,2]° ΔTE = 1.78 ms
B1 Map	1.48 x 1.48 x 7.7	20	1:16	3	α = 60°
DWI	1.25 x 1.25 x 5.0	30	1:09	2	b = 0, 200, 800
imFFE 32 echo	1.81 x 1.81 x 7.5	3 (1)	0:36 (0:25)	3	α = 12° (20°) ΔTE = 1.51 ms
IVIM	2.0 x 2.0 x 5.0	3	PPU triggered (~17 min)		b = 0, 10, 20, 40, 80, 100, 200, 600, 800, 1200

The flip angle (α) value was adjusted for the 4x2-echo and 32-echo imFFE scans after the first three subjects. The original value is listed in parentheses. The IVIM (intravoxel incoherent motion) sequence was added late in the study and was only acquired on the last 5 subjects.

2.4 Image Processing

2.4.1 MRI Fat-Water Separation Methods

After acquiring the scans, the 4x2-echo imFFE scan was processed, resulting in magnitude images of water, fat, R_2*, and ΔB_0 map. Prior to analysis, the first echo of each 4-echo train was discarded to avoid potential contamination by eddy currents in the complex water-fat signal model.[162] The echoes included for processing are illustrated in Figure 2.4-1.

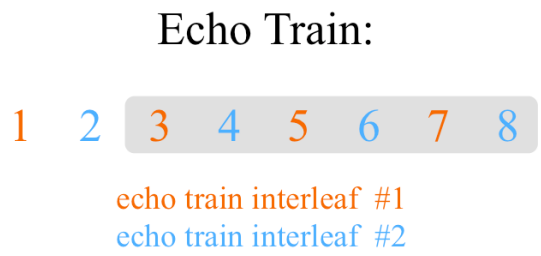

Figure 2.4-1. Echo train interleaves. Echoes shaded with the gray box are included during image analysis.

After discarding the first echo of each TR train the data were reconstructed and fat-water image separation was performed using one of two methods. The first, a complex-based method,[163] was used early in the research. This was later modified to incorporate a more robust hybrid complex- and magnitude-based method.[164] Both methods began by performing fat-water separation using a three-dimensional water/fat separation and R_2* estimation based on a multi-scale whole-image optimization algorithm.[163] The fat spectrum was modeled using either 9-peak[144] spectral model estimated from human liver or 6-peak model previously applied to multiple anatomies and field-strengths.[142,143,165] The frequencies and relative amplitudes of the 6-peak and 9-peak fat spectral models are listed in Table 2.4-1. The frequency and amplitude values are given assuming water is at 4.7 ppm with a relative amplitude of 1000.

Table 2.4-1. Fat-spectral information for the 6- and 9-peak models.

6-peak		9-peak	
Frequency [ppm]	Relative Amplitude	Frequency [ppm]	Relative Amplitude
0.90	87	0.90	8
1.30	693	1.30	642
2.10	128	1.60	58
2.76	4	2.02	62
4.31	39	2.24	58
5.30	48	2.75	6
		4.20	39
		5.19	10
		5.29	37

The fat spectral models listed here assume water has a frequency of 4.7 ppm and relative amplitude of 1000. The relative amplitudes for both the 6- and 9-peak models all sum to 1000.

In addition to better modelling of fat, a multipeak fat spectrum model was used because in the presence of fat, multipeak fat modeling is necessary for robust R_2* mapping.[166] For the first complex-based method, these images concluded the steps necessary to produce the magnitude images of water, fat and R_2*. For the second hybrid complex- and magnitude-based method, these three images (water, fat and R_2*) were then fed back into a second processing step along with the original complex data. This resulted in final magnitude images of water and fat. These final water and fat images were then used to calculate a FSF image using Equations [1.4-20] and [1.4-21] in Section 1.4.3.a). The main difference between the two fat-water separation methods performed occurs in the voxels with low and high fat content. This is because the complex-based methods are susceptible to phase errors, while magnitude-based methods are insensitive to phase errors. In the presence of phase errors, complex fat-water separation may have significant bias estimating FSF at locations with either very low (near 0%) or very high (near 100%) FSF. On the other hand, magnitude-based methods have difficulty correctly separating fat and water when they exist in similar proportions in a voxel (near 50% FSF). Therefore, by combining the

complex and magnitude methods it is possible to take advantage of the strengths of each method. The result is a fat-water separation approach that is robust to phase errors at low and high fat concentrations, while correctly distinguishing between water and fat in the mid-range of fat-fraction. Differences between the two methods are illustrated in low and high fat-fraction tissues, in Figure 2.4-2. In the liver (top panel), the complex method results in high (>10%) FSF values with clear shading across the liver. The hybrid method reduces the shading effect and lowers the FSF value to under 10% FSF. In the subcutaneous WAT (lower panel) it is also possible to see the shading present in the upper right corner of the complex method, resulting in a region of subcutaneous WAT with low FSF (~80%), which is corrected with the hybrid method. This demonstrates the importance of using the hybrid method, especially in quantifying the FSF of tissues with both low and high fat content.

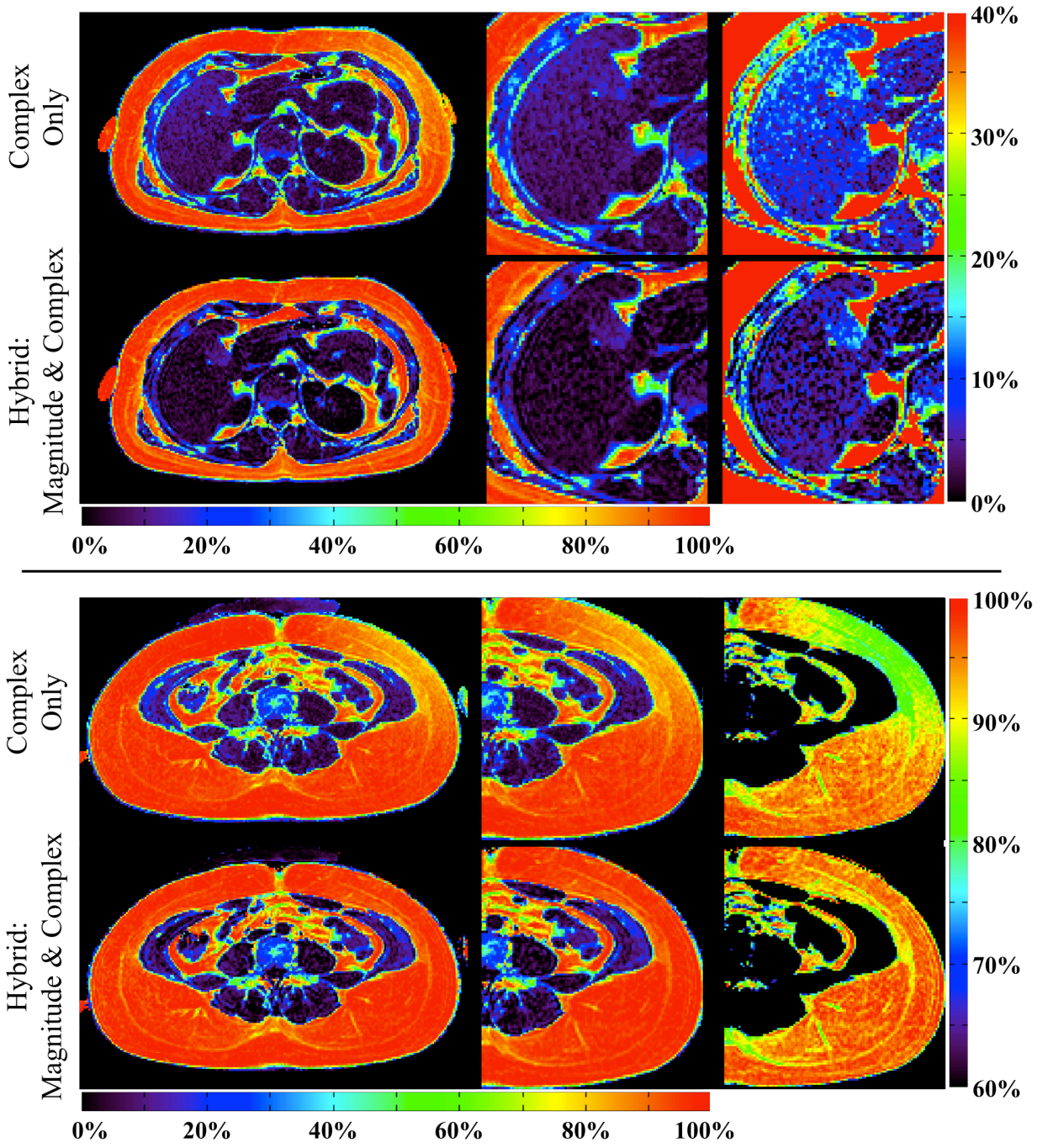

Figure 2.4-2. FSF comparison images resulting from the two fat-water separation methods employed in this research: complex and hybrid (magnitude and complex). The hybrid method is more robust to phase errors at low and high FSF values, as seen in the liver (top panel) and subcutaneous WAT (bottom panel).

Also, it is important to note that although T_1 weighting is possible given the scan parameters used, T_1 bias is worst near 50% FSF. Since this work is focused on FSF of white adipose tissue, T_1 bias is less of a concern. Specifically, given commonly accepted T_1 relaxation values for water and fat signals along with the sequence parameters used in this work, the estimated maximum absolute and mean absolute bias for FSF greater than 90% are 0.46% and 0.26% respectively.

2.4.2 Image Registration

To allow for analyzing the same anatomical region of interest in each of the four images for a given subject, all image volumes were co-registered for each subject individually. Registration was performed using a semi-automated method with in-house developed 3-plane-view software using a rigid body registration algorithm.[167] This registration method ensured registration in all three dimensions. Due to difficulties with registering the entire image volume across all four time-points, focus was placed on registering the anatomy of interest (either the supraclavicular region or the mid-abdominal region) for the study being performed. During registration, the MRI and PET data underwent partial volume interpolation resulting in the same voxel dimensions as the CT data.

2.5 Summary

The study design, data acquisition and image processing methods described in this chapter forms the basis for all the research presented in this dissertation. The work and results presented in each subsequent chapter are derived from the images obtained on these subjects.

CHAPTER 3

WAT – SEGMENTATION AND MRI VERSUS CT CORRELATION

3.1 Introduction

Quantifying imaging-derived properties of adipose tissue (AT) is an important field of research that has received much attention in recent years. The presence of AT can be a factor in many health conditions such as hypertension, diabetes, cardiovascular disease, liver disease, gallbladder disease, musculoskeletal disorders, and several types of cancer.[168] A recent review article by Wang *et al*.[169] expounds upon the importance of imaging AT depots throughout the body to better understand the relationship between obesity and health. His review concludes that the measurements obtained through imaging AT may have the most predictive capability in stratifying health risks. This is partly because of the variation in AT properties both spatially within subject, as well as inter-subject variability. Imaging with CT yields a quantitative measure of tissue radiodensity (HU), which can detect gradations in AT properties. This is demonstrated in one study that compares HU values to tissue lipid content in the BAT of rats.[170] This work showed that the HU values are less negative in cold-activated BAT than in controls, corresponding to a lower relative lipid content in histology. Another study measured the HU values of AT in growing pigs.[171] Their results showed that the HU values decrease for both adipose and non-adipose soft tissue as the pigs age. MRI can also be used to generate a quantitative measure of AT called FSF, (described in detail in section 1.4.3.a). Fat-water MRI has been extensively studied[147,172–175] and is accepted as a reliable quantitative method. MRI-derived FSF values are also sensitive to gradations in AT quality. The MRI-derived FSF values

quantified in this work are particularly reliable because specific steps are taken to ensure that the computed FSF is accurate. Specifically, this work employs time-interleaved gradient-echo scans with short echo time (TE) and high echo count for FWMRI. The robustness of FWMRI results are further strengthened by discarding the first echo of each readout train that may be contaminated by eddy-currents, by using a 9-peak fat model, and by performing a hybrid complex- and magnitude-based fitting of the data.

Several previous AT imaging studies aimed only to separate fatty tissue from lean tissue in order to estimate area and/or volume of visceral and subcutaneous adipose tissue (SAT), often correlating tissue volumes to subject height and weight.[176,177] Work has also been performed showing the high degree of reproducibility in measuring tissue area and volume using CT.[178] Additionally, it has been well studied that various fat depots are associated with metabolic risks. For example, both dual-energy x-ray absorptiometry (DXA) and CT measures of fat have been shown to correlate with measures of metabolic syndrome such as fasting insulin level and blood pressure,[179] and to waist circumference.[180] Other studies have used CT to measure abdominal visceral adipose tissue (VAT) and SAT areas as they correlate to hepatic steatosis,[181] and to measure epicardial fat volume and its relationship to coronary artery disease.[182]

While earlier studies that quantified AT volume are important, few studies measured the quantitative characteristics of these adipose depots. Recent work reported that the stratification of AT quality using both HU and FSF values had a stronger correlation to disease metrics. One such study showed that the properties of abdominal VAT and SAT as assessed using HU had a stronger correlation with higher body mass index (BMI) levels and cardiometabolic risk than total AT volume,[183] and correlated with coronary aortic calcium and abdominal calcium levels.[184] Similar to the research performed with CT to measure *in vivo* quantitative characteristics of AT

as it relates to health issues, MRI was recently used to quantify fat in diseased states, for example to measure the fat content of nonalcoholic fatty livers.[141,185,186]

Although most of the reported research to quantify AT characteristics was performed using CT, it is beneficial to use MRI to study AT for several reasons. Most importantly, MRI does not require any ionizing radiation, and therefore it can be more easily employed in longitudinal studies as well as in pediatric studies. The research performed to measure AT quantitative properties often uses either CT or MRI, and few studies have compared the properties measured by the two imaging modalities. One comparative study published in 1990 by Seidell *et al*.[187] used both CT and 1.5 Tesla MRI to calculate visceral and subcutaneous AT area. Another study from 2009 by Kullberg *et al*.[188] used CT, DXA and 3.0 Tesla MRI to calculate AT volume. While both of these studies compared imaging modalities, neither study correlated the CT quantitative values to MRI quantitative values. If such a correlation exists, it could support further investigation of adipose properties, which may have a stronger correlation to disease than adipose volume alone. Additionally, using MRI to quantify AT metrics would open up the possibility of performing longitudinal studies without the risk of exposing subjects to the ionizing radiation associated with CT.

Therefore, given that both CT HU and MRI-derived FSF are accepted methods for quantifying the properties of AT,[185,189] the research presented here aims to explore how the properties of lower abdominal subcutaneous WAT measured using CT HU correlate to MRI-derived FSF. Data presented here were part of an existing study[190] in which subjects underwent two MRI and two PET-CT scans after being exposed to both warm and cold temperatures. The first aim of this work is to determine if the quantitative properties of WAT measured with MRI and CT are self-consistent (intra-modality). The second aim assesses intermodality correlation of

the quantitative properties of WAT measured by MRI properties to those measured by CT, and investigates if this correlation is affected by BMI or temperature.

3.2 Materials and methods

3.2.1 Subjects

From the enrolled subject cohort described in Section 2.1, twenty-one were included for this project (age range: 21.5 to 34.5 years old, BMI range: 20.2 to 31.5 kg/m^2, 8 males, 13 females). Of these twenty-one, eighteen subjects have a complete dataset consisting of all four scans, two subjects have only cold scan data (PET-CT and MRI), and one subject has only warm scan data (PET-CT and MRI). The three remaining subjects were excluded because their MRI data were acquired with different scan parameters, and the last subject was excluded because no CT scans were acquired.

3.2.2 Sequences Applied

The MRI data processed for this project are taken from the 4x2-interleaved echo imFFE scan previously described in Section 2.3.2. The fat, water, and R_2* maps were reconstructed using the hybrid complex- and magnitude-based method previously described in Section 2.4.1, along with the 6-peak fat model outlined in section 2.4.1.

3.2.3 Mask Generation Method

A depot of subcutaneous WAT large enough to obtain measurements without partial volume effects was distinguishable in the posterior lower abdomen of all subjects, even in subjects with the lowest BMI. Therefore, focus was placed on accurate registration of only the

lower abdomen to ensure the best registration of the subcutaneous WAT depot. By registering the images prior to further analysis, this not only ensured that the same tissue was being analyzed across scans, but also allowed a single mask to be used to extract the subcutaneous WAT region of interest. Registration was performed using the method described in Section 2.4.2.

Image processing was performed using in-house developed MATLAB scripts. After registration, ten slices at the umbilicus level were selected for further processing and analysis. Once the ten slices were selected, a mask of the subcutaneous WAT depot was created for each subject based on the accepted ranges of HU and FSF values for WAT. For CT, the accepted HU values for WAT ranges from -150 HU to -50 HU,[189,191] while the accepted MRI FSF value for WAT is greater than 85% fat, as shown by work in mice,[147,192] postmortem infants and *in vivo* children.[148] Therefore, to generate the subject-specific subcutaneous WAT mask, the voxels on all coregistered scans had to fulfill all of the following requirements:

- MRI FSF values in the range of 85% to 100%, a range set to exclude fascia, (example FSF images seen in Figure 3.2-1a & d);
- CT HU values in the range of -200 HU to 0 HU, a range known to include WAT, (example CT images seen in Figure 3.2-1b & e);
- MRI R_2* values less than 200 s^{-1},[148,192] to exclude the skin/air interface.

These three rules resulted in an initial AT mask from which the subcutaneous WAT depot was manually selected for each of the ten slices for every subject. If any VAT was still included in the subcutaneous WAT mask, it was manually identified and removed, using the MRI FSF and CT HU images as guides. This manual exclusion of VAT was only necessary on a few subjects, and was typically an issue only for subjects with a larger BMI, although it also occurred in a few lean subjects having large amounts of VAT.

The resulting subcutaneous WAT mask was then further refined on a slice-by-slice basis through a single binary erosion of boundary pixels using the MATLAB function *bwperim* with an 8-connected neighborhood rule to define the perimeter to erode. This perimeter erosion both removed small clusters of pixels and contracted the boundary of large ROIs, thereby reducing any partial volume effects. Once the final WAT mask was created, statistical comparison showed the means of the edge voxels and core voxels of each WAT mask were not statistically different for either the FSF or HU values for any subject. This indicated that partial volume effects were absent. These steps resulted in a subject-specific conservative subcutaneous WAT mask. An example slice of the final WAT mask for two subjects is shown in Figure 3.2-1c & f).

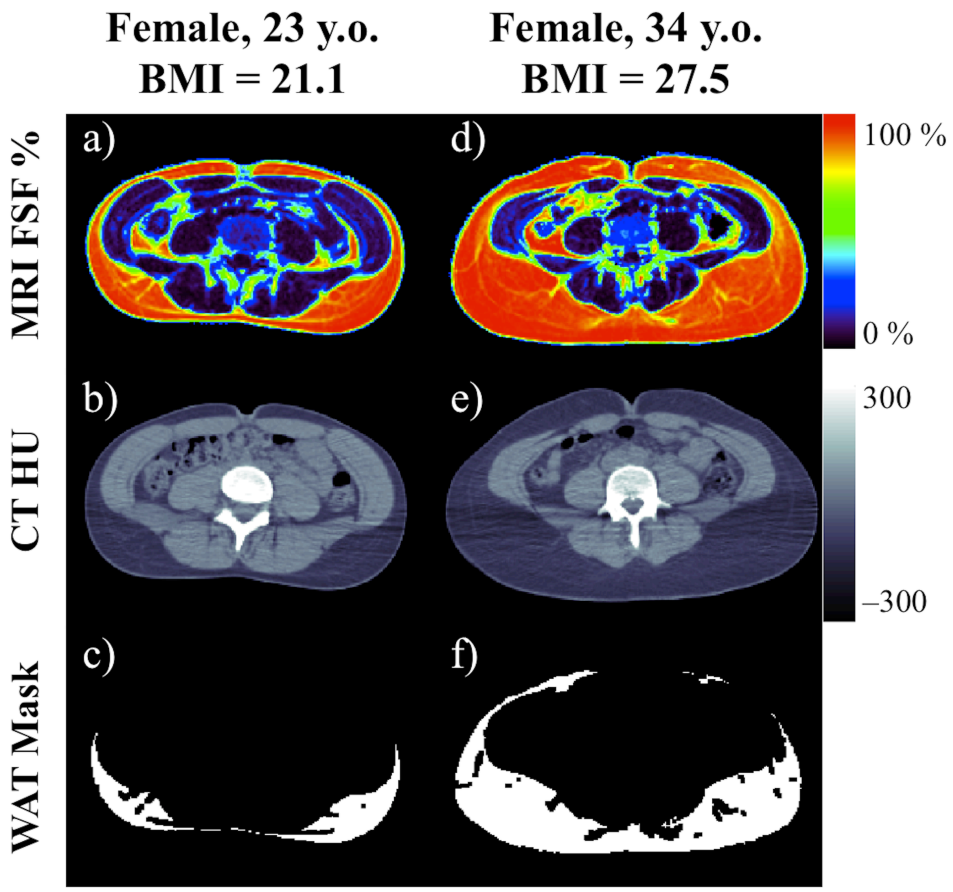

Figure 3.2-1. Axial slices at the umbilicus level of two female subjects, one with normal BMI (a-c) and one with an overweight BMI (d-f). Panels (a) and (d) show the fat-water MRI derived fat signal fraction (FSF) in percent. The coregistered CT Hounsfield Unit [HU] images for each subject are shown in panels (b) and (e). The corresponding subcutaneous white adipose tissue masks are shown in panels (c) and (f). The rules used to generate the WAT masks are based on FSF and HU values, may exclude fascia and use boundary erosion to reduce partial volume effects, thereby resulting in a conservative estimate of WAT.

After creating the subject-specific WAT mask, the mask was applied to the coregistered MRI FSF and CT HU images to obtain the FSF and HU values for each voxel in the masked regions. For each subject, the ten slices of data were averaged to obtain a single MRI FSF and CT HU value for both the warm and cold conditions. All statistical analyses were performed using RStudio (v0.98.1091; RStudio, Inc, Boston, MA). The FSF and HU values obtained were

plotted, and linear regression was performed to determine the correlation (R^2), slope and intercept. For all significance tests a *P*-value lower than 0.05 was considered significant.

3.3 Results

The subjects were divided into groups based on BMI: All BMI (n = 21, 8 male), BMI < 25 kg/m^2 (n = 15, 5 male, BMI range: 20.2 – 24.7 kg/m^2), and BMI ≥ 25 kg/m^2 (n = 6, 3 male, BMI range: 25.3 – 31.5 kg/m^2). The normal BMI and overweight BMI groups are statistically different from each other ($p < 0.0001$), while the age distributions of the two groups are not statistically significantly different. Dividing the subjects by BMI allows a comparison of data for different BMI levels, as previous groups have shown a correlation of HU values to BMI level.[176,183] Figure 3.2-1 shows images from two subjects, one with a low BMI (Female, 23 y.o., BMI = 21.1) and one with a high BMI (Female, 34 y.o., BMI = 27.5). This figure shows for each subject an axial slice of the registered MRI FSF (Figure 3.2-1a & d), and CT HU (Figure 3.2-1b & e), and the generated WAT mask (Figure 3.2-1c & f).

3.3.1 Intra-Modality Correlation

To assess the level of correlation using the same imaging modality, the cold values are plotted against the warm values for the same modality. Comparisons of FSF values are shown in Figure 3.3-1, and HU values are shown in Figure 3.3-2. In Figure 3.3-1, the plots show the FSF values are strongly correlated with each other when all subjects are considered as a group (R^2 = 0.92, $p<0.0001$ Figure 3.3-1a), with a slope and 95% Confidence Interval (95% CI) of 0.9 [0.7, 1.0], and y-intercept and 95% CI of 11.5 [-1.6, 24.5]. Plotting only those subjects with BMI < 25 also shows strong correlation (R^2 = 0.91, $p<0.0001$ Figure 3.3-1b). However when considering

the higher BMI subjects alone (Figure 3.3-1c), the correlation is weakly significant ($R^2 = 0.92$, $p = 0.04$). Figure 3.3-2 shows the comparison of cold HU to warm HU values. Plotting all subjects as a single group shows strong correlation between HU temperatures ($R^2 = 0.70$, $p<0.0001$ Figure 3.3-2a), with a slope and 95% CI of 0.9 [0.6, 1.3] and y-intercept with 95% CI of -5.0 [-38.3 28.3]. Additionally, separating the subjects by BMI results in strong correlation between HU values for the low BMI group ($R^2 = 0.67$, $p<0.001$ Figure 3.3-2b), and no significant correlation for the high BMI ($R^2 = 0.54$, $p>0.05$ Figure 3.3-2c) group. A full listing of the regression slope and y-intercept values and corresponding 95% CI values are in Table 3.3-1.

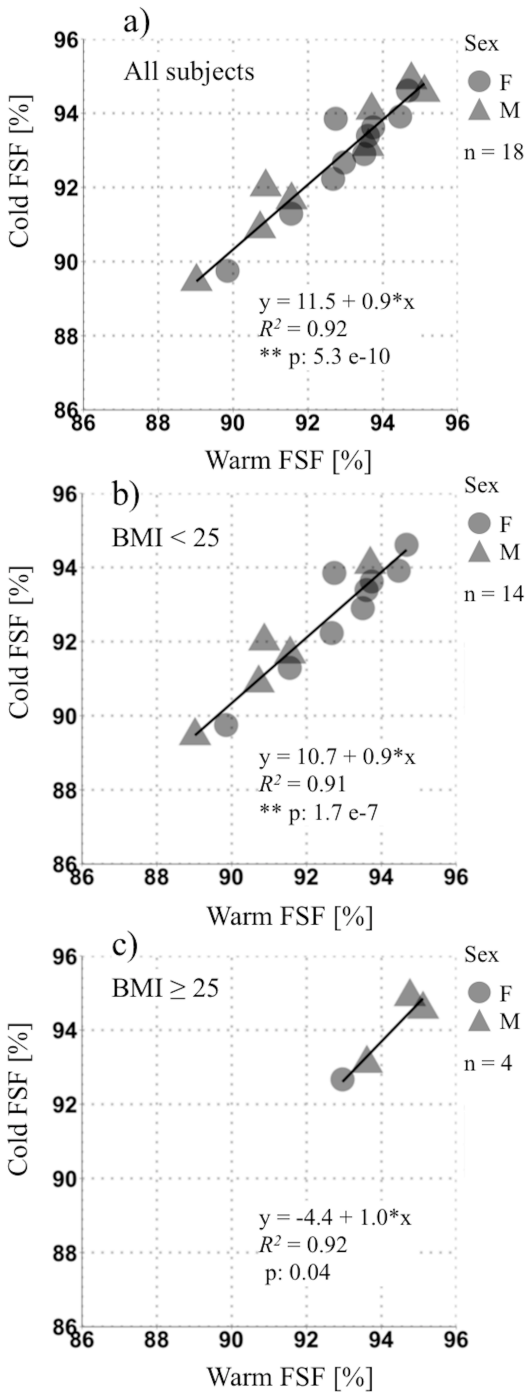

Figure 3.3-1. Plots of the cold and warm fat-water MRI derived fat signal fraction (FSF) values plotted against each other to investigate the intra-modality correlation. Panel (a) shows the result of plotting all subjects together, panel (b) is the values for the subjects with BMI < 25, and panel (c) is the plot of subjects with a BMI ≥ 25. FSF values are generally self-consistent for all the subjects, showing that for a given value of warm FSF, the corresponding cold FSF is slightly lower. Note that some symbols appear darker because of the overlap of multiple symbols.

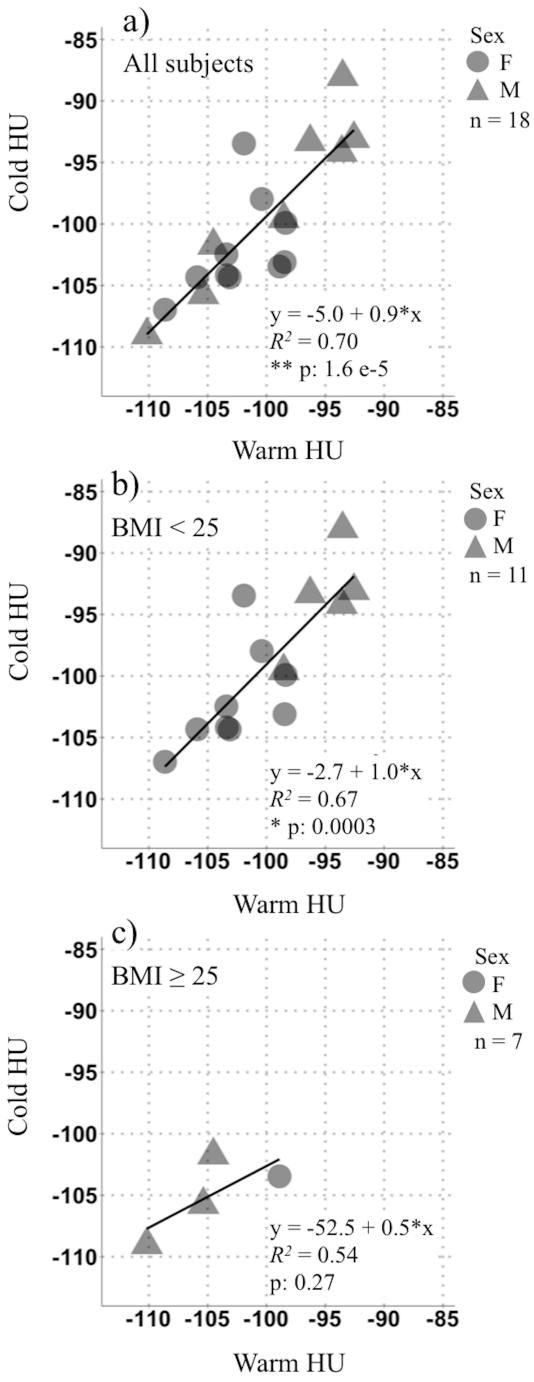

Figure 3.3-2. Plots of the cold and warm CT Hounsfield Units (HU) values plotted against each other to investigate the intra-modality correlation. Panel (a) shows the result of plotting all subjects together, panel (b) is the values for the subjects with BMI < 25, and panel (c) is the plot of subjects with a BMI ≥ 25. The HU values of both the plot of all subjects and the subjects with BMI < 25 are self-consistent, whereas for the subjects with BMI ≥ 25 the cold HU values are lower than the warm HU values. Note that some symbols appear darker because of the overlap of multiple symbols.

3.3.2 Inter-Modality Correlation

Assessments of the correlation between the properties of adipose tissue as measured by CT HU and MRI FSF values are presented in Figure 3.3-3 - Figure 3.3-5. Initial analysis was performed on both the cold and warm data keeping all the subjects as one group, as plotted in Figure 3.3-3. In this plot, a single subject has two data points, one for the cold data and one for the warm data. This plot shows a significant correlation between the CT HU and MRI FSF values (R^2 = 0.54, $p < 0.0001$), with a slope and 95% CI of -2.6 [-3.3, -1.8], indicating that a change of 1 HU corresponds to a change of 0.38% [0.30%, 0.56%] FSF. Additionally the y-intercept value and 95% CI of 136.9 [64.1, 209.6], is representative of the HU value expected when the fat content is zero. Comparing the y-intercept value to muscle tissue values (healthy muscle being a tissue with very low fat content) the value of 136.9 is contained within the range of normal muscle attenuation of 30 to 150 HU,[193] and falls far below that of bone.

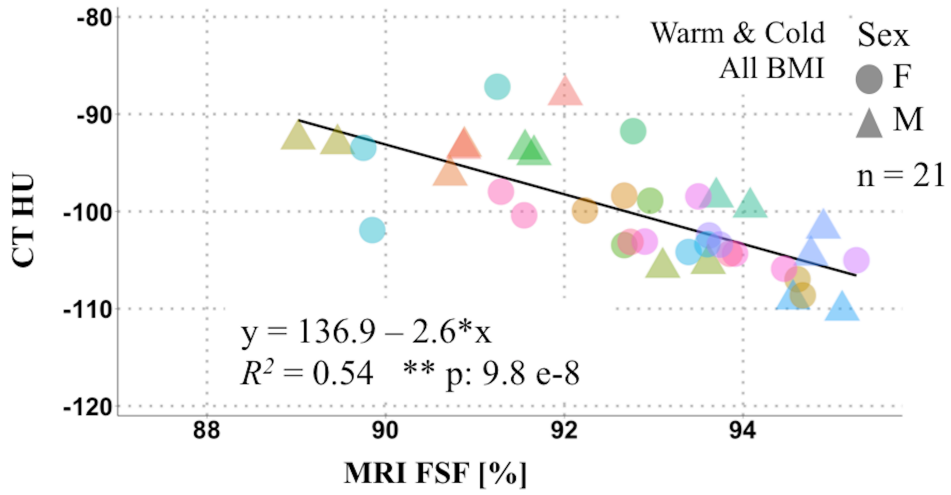

Figure 3.3-3. Plot of CT HU versus fat-water MRI FSF of both the warm and cold data for all 21 subjects. This shows a strong correlation between the HU and FSF measures of abdominal subcutaneous white adipose tissue quality. Note: the same color marker represents the same subject under warm and cold conditions.

To investigate any effects of temperature and BMI, the data were split two ways. First the data were split by BMI, as seen in Figure 3.3-4a & b), and then the data were split by temperature, as seen in Figure 3.3-4c & d). Grouping the warm and cold data together, but separating the subjects by BMI level shows that the low BMI data are significantly correlated (R^2 = 0.52, p<0.0001 Figure 3.3-4a), while the high BMI data are not significantly correlated (R^2 = 0.32, p = 0.09 Figure 3.3-4b). The results from dividing the data by temperature while keeping all the subjects as one group are plotted in Figure 3.3-4c & d. These plots show that both the cold and warm data show significant correlation between the CT HU and the MRI FSF values (R^2 = 0.54, p < 0.001 Figure 3.3-4 d) than the warm data (R^2 = 0.54, p < 0.001 Figure 3.3-4c).

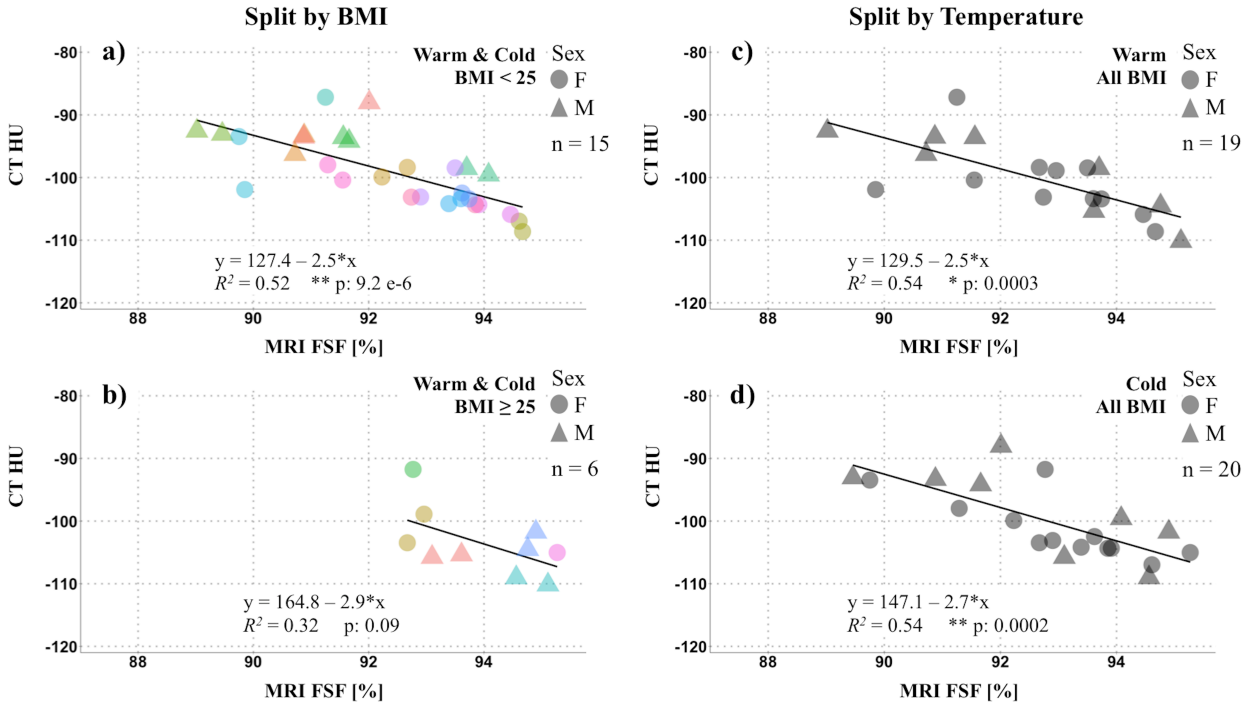

Figure 3.3-4. Separating the entire dataset either by BMI level as seen in panels (a) and (b), or by temperature (c) and (d). Plotting the warm and cold data together shows a strong correlation between CT HU and MRI FSF for the subjects with BMI < 25 (a), but not for subjects with BMI ≥ 25 (b). Splitting all the subjects by temperature results in a correlation between the HU and FSF measures of adipose tissue quality for both warm (c) and cold (d) data. Note that within panels (a) and (b) the same color marker represents the warm and cold data for one subject. However, the color of the markers is self-contained to each plot.

To further explore how the measure of adipose tissue properties compare between CT HU and MRI FSF, the data were split by both temperature and BMI level, as shown in Figure 3.3-5. Here the data for the low BMI group show significant correlation both under warm (R^2 = 0.45, $p < 0.01$ Figure 3.3-5a) and cold, (R^2 = 0.62, $p < 0.001$ Figure 3.3-5b) conditions. The data for the high BMI group do not show significant correlation for either warm (R^2 = 0.71, $p > 0.05$ Figure 3.3-5c) or cold (R^2 = 0.20, $p > 0.05$ Figure 3.3-5d) temperatures. The data for the cold low BMI group have the highest R^2 value of 0.62 out of all the groups comparing CT HU and MRI FSF, with a mean slope and 95% CI of -2.7 [-4.1, -1.4] and mean y-intercept and 95% CI of 154.8 [30.8, 278.7]. A full listing of the regression slope and y-intercept values and corresponding 95% CI values for all plots are in Table 3.3-1.

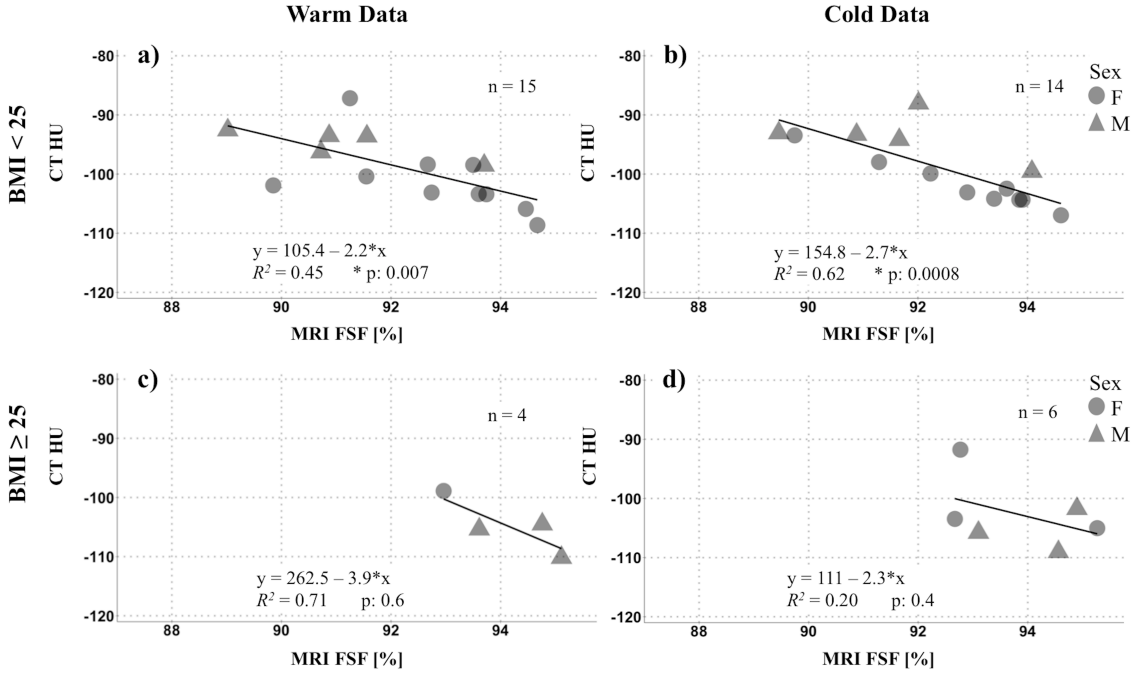

Figure 3.3-5. Plots of the dataset split by both BMI level and scan temperature. This split reveals the strongest correlation between the two measures of adipose tissue quality for the subjects with BMI < 25 exposed to cold (b). The warm data for subjects with BMI < 25 (a) is also significant, though the correlation is slightly weaker. However, neither the warm (c) nor cold (d) plots are significantly correlated for subjects with BMI ≥ 25.

Table 3.3-1. The slope and y-intercept values including 95% Confidence Intervals (CI displayed as [2.5%, 97.5%]) for each plot in **Figure 3.3-3** - **Figure 3.3-5**.

	Slope			Y-Intercept		
FSF v FSF: All BMI	0.9	[0.7	1.0]	11.5	[-1.6	24.5]
FSF v FSF: BMI < 25	0.9	[0.7	1.1]	10.7	[-5.9	27.4]
FSF v FSF: BMI ≥ 25	1.1	[0.1	2.0]	-4.4	[-94.2	85.4]
HU v HU: All BMI	0.9	[0.6	1.3]	-5.0	[-38.3	28.3]
HU v HU: BMI < 25	1.0	[0.5	1.4]	-2.7	[-45.0	39.5]
HU v HU: BMI ≥ 25	0.5	[-0.9	1.9]	-52.5	[-200.3	95.3]
HU v FSF: All temp & All BMI	-2.6	[-3.3	-1.8]	136.9	[64.1	209.6]
HU v FSF: All temp & BMI < 25	-2.5	[-3.4	-1.5]	127.4	[42.1	212.7]
HU v FSF: All temp & BMI ≥ 25	-2.9	[-6.2	0.5]	164.8	[-152.2	481.8]
HU v FSF: Warm & All BMI	-2.5	[-3.6	-1.3]	129.5	[21.9	237.1]
HU v FSF: Cold & All BMI	-2.7	[-3.9	-1.5]	147.1	[35.1	259.1]
HU v FSF: Warm & BMI < 25	-2.2	[-3.7	-0.7]	105.4	[-31.2	242.1]
HU v FSF: Warm & BMI ≥ 25	-3.9	[-11.4	-3.6]	262.5	[-447.6	972.7]
HU v FSF: Cold & BMI < 25	-2.7	[-4.1	-1.4]	154.8	[30.8	278.7]
HU v FSF: Cold & BMI ≥ 25	-2.3	[-8.6	4.1]	111.0	[-484.4	707.8]

3.3.3 Testing Additional Fat-Water Separation Models

To demonstrate that the fat-water separation parameters are important to producing a reliable quantification of the FSF of tissue, the MRI data was reprocessed three additional times using alternative parameters. The parameters used in the three models are listed in Table 3.3-2. Each of the three models was processed using the complex fat-water separation method described in Section 2.4.1.

Table 3.3-2. Parameters for three fat-water MRI separation models.

	Total Echoes	Echo train interleaf #1 Echo train interleaf #2	Fat-peak model	R_2* Correction
Model A	6	1 2 **3 4 5 6 7 8**	9-peak	Yes
Model B	8	**1 2 3 4 5 6 7 8**	9-peak	Yes
Model C	3	**1 2 3** 4 5 6 7 8	3-peak	No

The echoes used in the fat-water separation for each model are highlighted with a gray box.

The results from each of these three models were plotted versus the CT HU values to assess how the model affected the correlation between the CT HU and MRI FSF values, as seen in Figure 3.3-6.

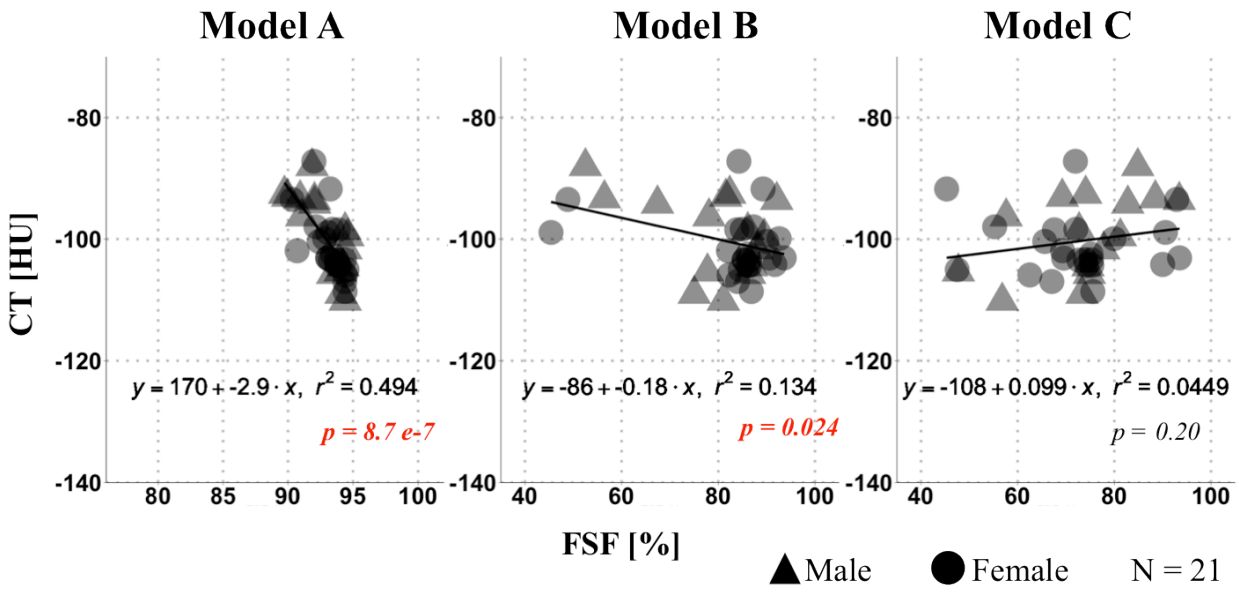

Figure 3.3-6. CT HU versus fat-water MRI FSF of both warm and cold data for all 21 subjects, plotted for models A, B and C, as described in **Table 3.3-2**.

From these plots it is clear that the fat-water separation approach affects quantification of FSF. Model A, which differs from the original method in fat-peak spectral model and fat-water

separation method, is the only model comparable to the original method (Figure 3.3-3). The plot of Model A also shows a significant correlation between the CT HU and MRI FSF values (R^2 = 0.49, $p < 0.0001$), with a slope of -2.9, indicating that a change of 1 HU corresponds to a change of 0.34% FSF. However, perhaps of more significance than the lack of correlation to CT HU values, is that the FSF values resulting from Models B and C range from 40-95% FSF, whereas both the original method and Model A only range from 88%-95% FSF. Because the tissue analyzed in this work is subcutaneous WAT, these values are not physiologically plausible. The main difference affecting the drastic differences seen in Models B and C is likely the inclusion of the first echoes from each echo-train, which contain eddy-current contamination. From these results it is possible to conclude that the parameters used when performing fat-water separation matter, particularly excluding the first echoes.

3.4 Discussion

In this study we measured the properties of abdominal subcutaneous WAT in 21 healthy adults with a range of BMI levels using both CT Hounsfield Units and fat-water MRI-derived fat signal fraction. Both the CT and MRI scans were performed twice for each subject, once after exposing the subject to warm temperatures, and once after exposure to cold temperatures. This enabled the values to be compared both intra-modality, as well as correlating the two modalities to each other. When comparing intra-modality data, both the FSF and HU values demonstrated strong consistency between scans. It is possible that one reason for disagreement is a result of a resonant frequency shift of the water peak due to temperature. This is not accounted for in the FWMRI reconstruction in this study because of insufficient spectral resolution (too few echoes) in the acquired data. Another possibility is that there may be a physiological factor occurring that

accounts for the difference in fat measured at the two temperatures. Despite the possibility for physiological differences at the different temperatures, the difference in values for both FSF and HU data is only very slight. Because this dataset does not include two scans at the same temperature, an intra-modality comparison could not be made within temperature.

After determining that the HU and FSF measures were self-consistent, the two values were correlated to each other. This correlation was first performed disregarding the potential influence of either subject BMI or scan temperature on the measured properties, followed by separating the data by BMI and temperature independently, and finally separating the data by both BMI and temperature. The data were separated by BMI to determine if there was a difference in the subcutaneous WAT quantitative properties based on BMI as has been previously reported. Interestingly, the correlation between the FSF and HU values is strongest for subjects with lower BMI who have been exposed to cold temperatures immediately prior to scanning (Figure 3.3-5b). There are several factors that may explain this connection.

First, it is possible that there is a difference in physiologic response after exposure to cold between the leaner and heavier subjects. The subjects with lower BMI may be more susceptible to cold, while those with higher BMI may have less of a response to the cold and therefore the data will not differ as greatly from their warm data. Cold-induced vasoconstriction causes a redistribution of blood from the periphery to the core, particularly in leaner subjects.[194] Therefore the SAT may become less perfused with flowing blood in the leaner subjects. Because flowing blood may not be detected fully by fat-water MRI FSF while still affecting radiodensity measured by CT HU, the cold condition with less blood perfusion is likely a more direct comparison of tissue adiposity between FSF and HU. It is interesting to note that previous work by Kern et al.[195] showed an increase in UCP1 and PGC1α mRNA in the winter compared to the

summer from biopsies of subcutaneous abdominal WAT. Although it is likely not the case that the FSF and HU values are detecting these changes, it is noteworthy that other research also shows differences in the subcutaneous WAT depot due to exposure to cold temperatures. Because these data were acquired as part of a separate study where biopsies were not acquired, histological confirmation of the changes in tissue composition cannot be assessed in this report.

Second, the range of both HU and FSF values is reduced for high BMI subjects compared to subjects with low BMI. The subjects with higher BMI have reduced variability in both HU and FSF values, which can result in weaker correlations because the data is tightly clustered. As seen in Figure 3.3-1, the FSF range for subjects with low BMI is 5.7%, ranging from 89.0% to 94.7% fat, whereas for subjects with high BMI, the FSF range is much smaller at only 2.3%, ranging from 92.6% to 94.9% fat. Similar to the trend of values seen in FSF, the HU range for subjects with low BMI spans a wider range than the HU values of the higher BMI subjects. The low BMI subjects show a range of 20.6 HU (from -108.6 to -88.0 HU), while the subjects with high BMI span only 11.3 HU (from -110.2 to -98.9 HU). The variation in the range of adipose tissue property values for the different levels of BMI is in agreement with previous research showing a correlation between high BMI and lower (more negative) CT HU values.[183] Though it is possible the this broader range of FSF values in the WAT of leaner subjects is due to factors such as cell size,[196–198] without tissue biopsy to confirm we currently do not have an explanation of this observation. This finding warrants further investigation, especially in regards to the connection between FSF and BMI, as this appears to be unexplored in the current literature.

While this study reports promising initial findings in the correlation between MRI FSF and CT HU values, this work suffers from a few limitations. Due to the limited enrollment of overweight subjects in this study, there is low power for detecting the correlation between high

BMI versus either FSF or HU values. However, because of the connection between BMI and the properties of adipose tissue, this study could be improved by including a wider range of BMI values in a larger cohort. There is also the weakness that this study does not include repeated (a.k.a. test-retest) scans from the same imaging modality under the same temperature. Therefore, intra-subject variability within imaging modality cannot be estimated for this study. However, this study does begin to explore the correlation of MRI-derived FSF of adipose tissue to CT HU values, and uncovers temperature as a potential factor affecting quantitative measurements of subcutaneous WAT in the lower back. Our findings could also be enhanced by future comparison of FSF to HU values from a multi-spectral CT unit. This is because measurements from more than one energy level provide additional information about tissue composition that is not available using a single energy source.

3.5 Conclusion

This work demonstrates that fat signal fraction obtained using quantitative fat-water MRI at 3.0 Tesla is significantly correlated with CT HU. Additionally, the finding that HU values of subcutaneous adipose tissue are inversely related to BMI is supported by the current literature,[183] serving to verify in part, our results. Though the finding of a correlation between CT HU and MRI-derived FSF values is perhaps not a surprise, little work currently exists in the literature to demonstrate this correlation. The work here shows that given the correlation of MRI FSF to CT HU, FSF could be used as an alternative to CT HU for assessing metabolic risk factors via the impact on adipose tissue quality. Furthermore, spatial mapping of quantitative adipose tissue properties, in addition to the assessment of adipose distribution and volume, could enhance understanding of health factors affected by adipose tissue.

CHAPTER 4

BAT – SEGMENTATION AND CHARACTERIZATION

4.1 Introduction

Partly due to the role BAT plays in energy expenditure, as well as other potential areas of impact such as maintenance of insulin levels,[11,199] and countering obesity,[83,200–202] interest in studying and understanding BAT has increased greatly in the past few years. However, the study of BAT in humans is limited because apart from biopsy and histological staining, the currently accepted unequivocal method for detecting BAT is through ^{18}F-FDG PET-CT scans. When activated by cold exposure BAT takes up the ^{18}F-FDG radiotracer, a metabolic analogue of glucose, and becomes visible on PET images, in comparison to the much lower level of ^{18}F-FDG uptake in inactive BAT.[12–14,157] Although a useful technique for detecting the glucose metabolism of active BAT, ^{18}F-FDG PET does not reveal the primary substrate fuel, fatty acids.[15,16] Additionally, CT images acquired during a PET exam on a PET-CT scanner help to differentiate between tissues with high ^{18}F-FDG uptake by providing anatomical information. This use of PET-CT imaging exposes the subject to ionizing radiation (predominately from PET, though the dose from the CT scan is not negligible), and is therefore an undesirable method for BAT detection.

One difficulty of using imaging methods to study BAT is related to performing image segmentation to define the boundaries of tissue depots. Currently, segmentation of BAT in human studies often relies on some degree of manual image segmentation and is therefore vulnerable to misidentification of BAT depots, as well as inter-rater variability. Reliable spatial

mapping techniques that can distinguish BAT from WAT distributions, along with automated segmentation methods, would provide investigators with a powerful new tool with which to study BAT. MRI has already been proposed as an alternative BAT imaging technique.[17] MRI is useful partly because it is nonionizing and therefore longitudinal studies are possible. Additionally, unlike PET, MRI can detect BAT under thermoneutral (non-activated) conditions, and has been used to measure BAT volume and activity.[203–205] Using MRI to detect the differences between BAT and WAT is possible because BAT and WAT have unique characteristics, as outlined in Section 1.2.1.

One aim of our research is to develop a method for automated classification of BAT using statistical analysis of biomedical imaging properties of known BAT and non-BAT voxels. Many previous studies have investigated BAT, but often each study uses a different method for determining what constitutes BAT.[11,148,206,207] The second aim of this research is to quantify the PET-CT and MRI characteristics of active and inactive clavicular BAT in normal weight and overweight adult subjects, and to compare these to the values in subcutaneous WAT. Additionally, this work aims to determine if MRI is capable of detecting a difference between active and inactive BAT. This would prove useful as ^{18}F-FDG PET can only detect activated BAT. Finally, this work quantifies image-based adipose tissue metrics in both PET-positive and PET-negative subjects. Here "PET-positive" indicates subjects whose clavicular BAT had increased ^{18}F-FDG levels after exposure to cold, and "PET-negative" indicates subjects who did not.

We hypothesize that these quantitative FWMRI metrics, in conjunction with other quantitative MRI metrics, can reliably visualize and quantify BAT depots in humans. This would

provide the research community with a powerful tool with which to study BAT's influence on metabolism and energy expenditure without the use of ionizing radiation.

4.2 Subjects and Image Acquisition

Out of the enrolled subjects described in Section 2.1, twenty-four are included for this investigation. The only subject excluded was the subject who withdrew from the study prior to completing any PET-CT scans. A complete flow chart explaining the breakdown of all 25 subjects is given in Figure 4.2-1.

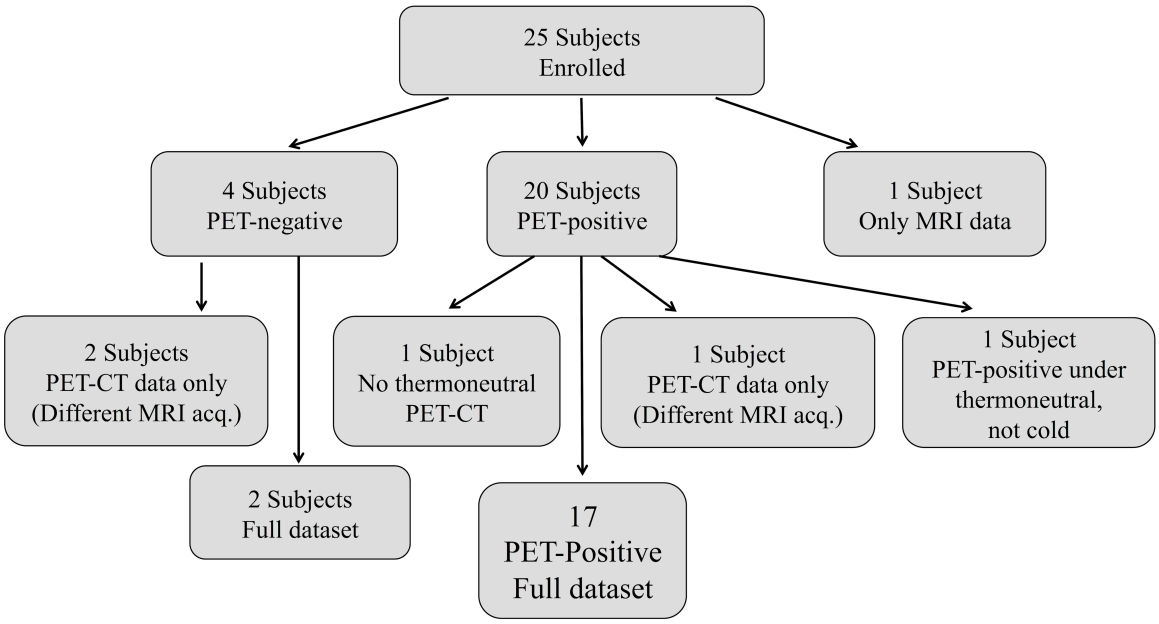

Figure 4.2-1. Flow chart of subject recruitment.

Of the 25 subjects enrolled, 19 showed increased ^{18}F-FDG uptake in the clavicular adipose tissue after exposure to cold, and low ^{18}F-FDG uptake after thermoneutral exposure. In this work we refer to these subjects as PET-positive for BAT, corresponding with previously

published findings.[12,14] Of these, seventeen PET-positive subjects are included in this study (6 male), mean ± SD: age: 25.1 ± 2.9 years, and BMI: 23.9 ± 2.9 kg/m^2 (Table 4.2-1).

The MRI data processed for this project is taken from the 4x2-interleaved echo imFFE scan previously described in Section 2.3.2. The fat, water, and R_2* maps were reconstructed using the hybrid complex- and magnitude-based method previously described in Section 2.4.1, using the 6-peak fat model outlined in section 2.4.1. From these fat and water maps, the FSF images were calculated using Eqns. [1.4-17] and [1.4-21].

Table 4.2-1. PET-positive subject characteristics.

Characteristic	**Normal BMI ≤ 24.9**	**Overweight BMI ≥ 25**
N (male)	12 (4)	5 (2)
Age (yr.)		
Mean	24.5 ± 1.8	26.5 ± 4.1
Range	21.6 – 27.9	23.1 – 34.5
Height (cm)		
Mean	167.7 ± 6.2	166.1 ± 8.9
Range	157.0 – 176.5	153.5 – 176.5
Weight (kg)		
Mean	63.2 ± 6.6	75.9 ± 8.4*
Range	52.4 – 74.7	64.9 – 85.9
BMI (kg/m^2)		
Mean	22.4 ± 1.4	27.5 ± 2.1**
Range	20.2 – 24.7	25.3 – 31.5
Waist (cm)		
Mean	73.8 ± 2.3	82.0 ± 6.6*
Range	69.0 – 78.8	73.0 – 89.3

Values are means ± SD. * p-value < 0.05, ** p-value < 0.001, using the Mann-Whitney U test to compare normal to overweight subjects. BMI: body-mass index; Waist: waist circumference measured at umbilicus. This shows that the age and height are not different between the normal and overweight subjects. Therefore age is not a confounding factor in considering which properties may affect brown adipose tissue characteristics between subjects. However, the population distribution of weight, BMI, and waist circumference are right-shifted (larger valued) in overweight subjects compared to normal weight subjects.

4.3 BAT Mask Generation Method

Though BAT depots exist in several locations throughout the human body,[23] the largest depot is found in the clavicular region. Therefore, the research performed in this study aims to focus on identifying, segmenting and defining the characteristics of only the clavicular BAT depot. This region of interest is highlighted in Figure 4.3-1, which shows a coronal PET MIP of a subject after exposure to cold. In addition to the increased ^{18}F-FDG uptake in the brain, heart and kidneys, as indicated by the solid black regions, there are symmetrical regions of uptake in the shoulders and along the vertebral column. The clavicular BAT depots are circled in red in Figure 4.3-1.

Figure 4.3-1. Coronal PET maximum intensity projection (MIP) image from a cold PET scan displayed in reverse gray scale. The clavicular BAT depot, which is of interest for this work, is highlighted with a red circle.

Generating a mask of the clavicular BAT depot enables analysis of the same anatomical region of interest in each image for a given subject. Therefore, all image volumes were co-registered for each subject individually using the method described in Section 2.4.2. The image registration workflow is depicted in Figure 4.3-2 a). Due to difficulties with registering the entire

image volume across all four scans, emphasis was placed on registering the region covering the chin to heart. During registration, the MRI and PET data underwent interpolation resulting in the same voxel dimensions as the CT data.

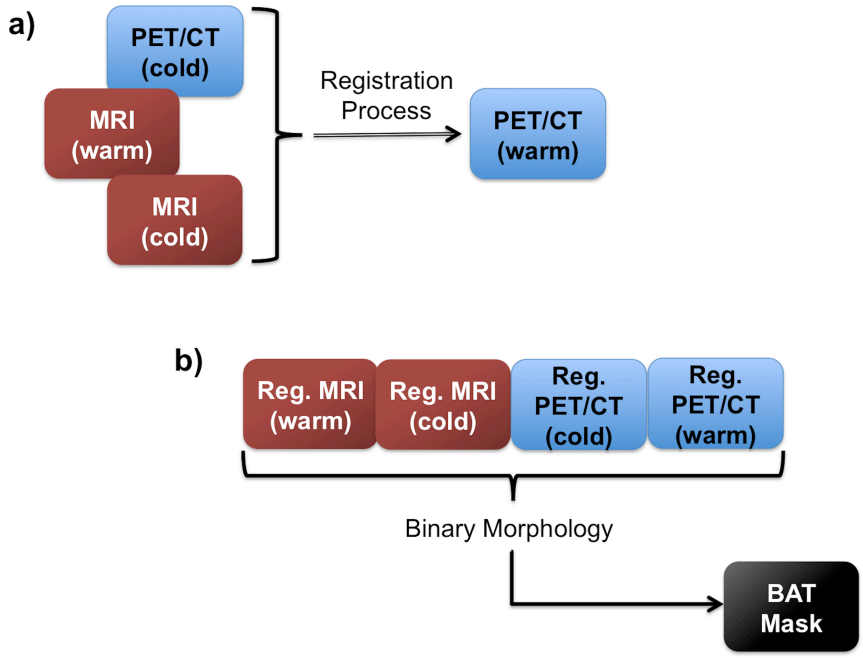

Figure 4.3-2. Flow charts showing the registration step (A), in which the images are all registered to the same image space. Following the registration, all four images are used in the BAT mask creation (B).

Example clavicular level axial slices of the registered thermoneutral (TN) and cold (CA) CT HU, PET SUV and MRI FSF images are displayed in Figure 4.3-3.

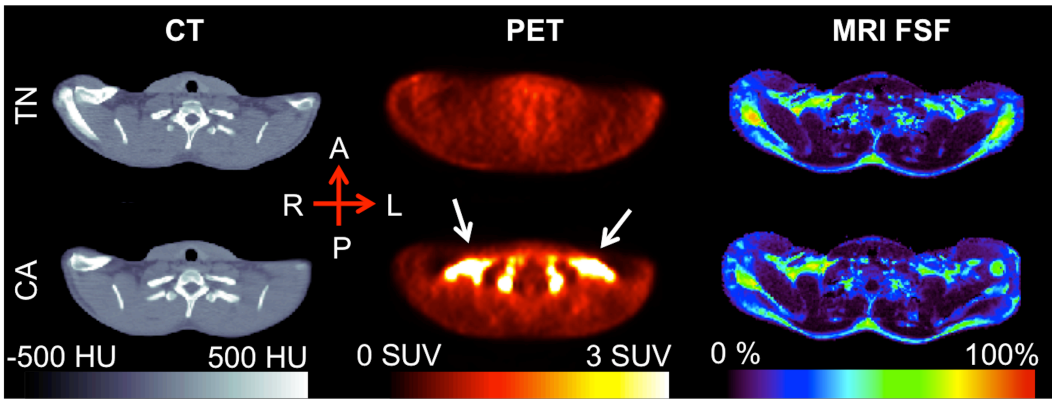

Figure 4.3-3. Clavicular-level axial slices, post-registration. The increased ^{18}F-FDG uptake seen in the CA PET scan (white arrows), occurs in the supraclavicular region of adipose tissue as determined by the CT Hounsfield Unit values. The MRI fat signal fraction (FSF) in this region falls in the 50-80% range, similar to that of previous research.

Following image registration, a subject-specific binary mask of the clavicular BAT depot in PET-positive subjects was created using the quantitative properties of the images. To be included in the mask, a voxel had to fulfill all the following requirements:

- CT HU values between -200 and -1 HU
- Cold PET SUV > 2.0
- SUV signal fraction > 55%
- MRI FSF > 20% fat

SUV signal fraction is defined as: $\frac{Cold\ SUV}{Cold\ SUV + Warm\ SUV}$. This SUV signal fraction (seen in Figure 4.3-4) rule was added in place of the rule that the warm SUV must be < 2.0, as is the common rule used in other human BAT PET imaging studies. This rule was necessary because the BAT in one subject activated under thermoneutral conditions, which would have eliminated this subject from analysis. The CT HU and MRI FSF rules must hold true for both the cold and

thermoneutral data. Example axial slices from the cold and thermoneutral scans can be seen in Figure 4.3-3.

The BAT ROI was further refined by requiring that more than 15 immediately neighboring voxels (in 3D) must be part of the initial rule-based ROI. This 15-voxel-neighborhood rule both removed small clusters of voxels and contracted the boundary of large ROIs, ensuring that the resulting ROIs focused primarily on the center of BAT depots, thereby reducing partial volume and edge effects. The resulting ROIs formed subject-specific "BAT masks", as seen in Figure 4.3-4.

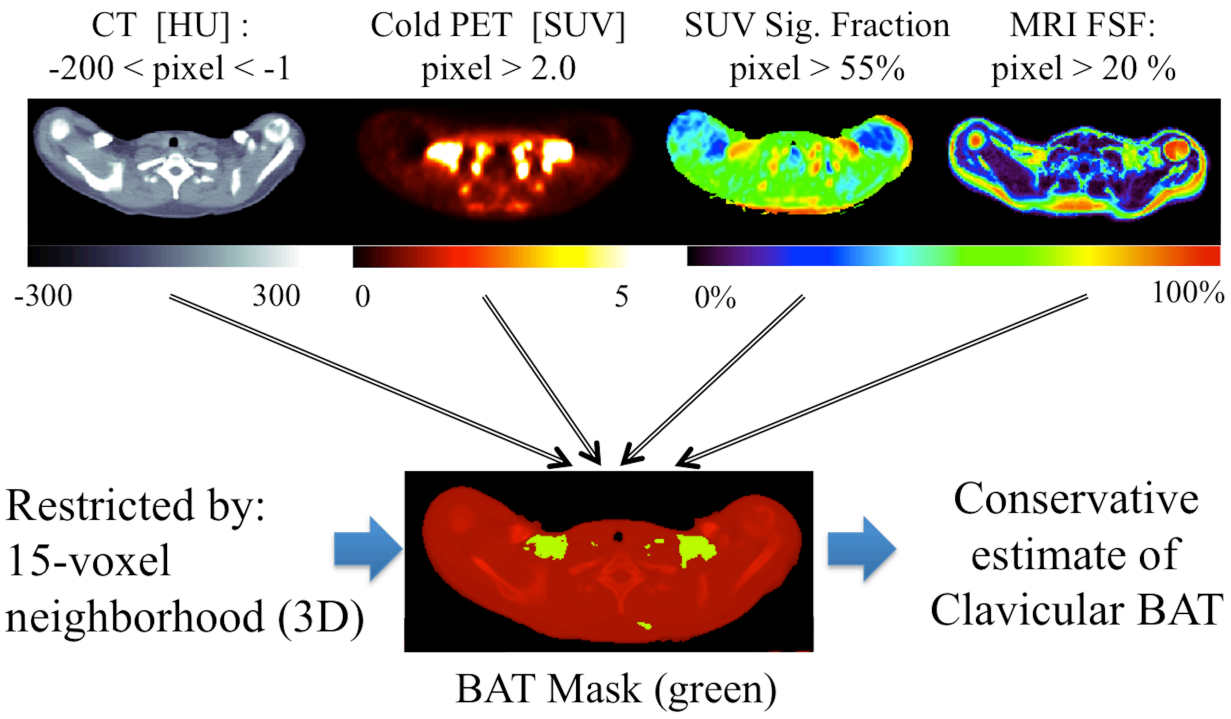

Figure 4.3-4. Pictorial depiction of the rules used to generate a BAT mask, based on the quantitative properties of the CT, PET, and MRI scans. To be considered part of the BAT mask each voxel in the image must satisfy these four rules, as determined on a slice-by-slice basis. If a voxel fulfills all these criteria, it is included in the binary mask of BAT identity.

The mask was limited for each subject to only include slices that covered, at most, from the C3 vertebrae to the aortic arch. The cropped BAT mask was then applied to all the co-registered images to evaluate the HU, SUV, FSF, and R_2* values in the BAT depots for both the thermoneutral and cold scan. Using this automated method minimized the effect of rater subjectivity and boundary ambiguity thus enabling objective analysis of the same region of tissue in all co-registered images for a given subject.

4.4 Results

4.4.1 Data Analysis

Except where noted, image analysis was performed using in-house developed MATLAB 2014a (Mathworks, Natick, MA, USA) scripts, and statistical analysis was performed in RStudio v0.98.1091 (RStudio, Boston, MA, USA). Analysis was conducted two ways: keeping the 17 subjects as one group, and dividing the subjects into two groups based on BMI: normal (BMI $\leq$ 24.9) and overweight (BMI $\geq$ 25.0). Prior to comparing thermoneutral and cold data for the whole group, the data were first tested for normalcy to determine if a parametric or nonparametric statistical test should be used. Testing for normalcy was performed using three methods. First a histogram of the data was plotted and visually inspected to determine if the histogram appeared normally distributed. Second, a Quantile-Quantile (QQ) plot of the data was visually inspected for linearity, and third, the Shapiro-Wilk test was used to test for normalcy, given the null hypothesis that the data are normal and a p-value > 0.05 indicating that the null hypothesis cannot be rejected. When comparing thermoneutral and cold data for the normal and overweight BMI groups, nonparametric tests are used because it is not meaningful to test for normalcy in groups with small numbers. Data are presented as mean ± SD, unless otherwise noted.

4.4.2 BAT Properties

Analysis of the PET-positive subject characteristics revealed that neither age nor height is different between the normal and overweight groups. This removes both age and height as confounding factors when determining which characteristics may affect the differences in BAT between these two groups. However, weight, BMI and waist circumference are significantly higher in the overweight subjects (Table 4.2-1). Other potential contributors to BAT activation were also analyzed for differences between the subjects. These potential contributors are: fasting glucose level, body temperature and outdoor temperature.[158,208] Fasting blood glucose levels were not significantly different between the thermoneutral and cold PET-CT scans for all 17 subjects (89.6 ± 6.1 mg/dL (thermoneutral) and 86.5 ± 8.4 mg/dL (cold), p-value = 0.52), or for the normal weight (90.8 ± 5.4 mg/dL (thermoneutral) and 85.8 ± 7.5 mg/dL (cold), p-value = 0.19) and overweight (85.8 ± 7.1 mg/dL (thermoneutral) and 88.4 ± 11.1 mg/dL (cold), p-value = 0.27) groups. However the subjects' body temperature after two hours in the temperature controlled room ($\Delta T = T_{hour\text{-}2} - T_{hour\text{-}0}$) increased significantly in the thermoneutral room (mean ± SD): ($\Delta T = 0.29 \pm 0.68$ °F, p-value = 0.02), and decreased significantly in the cold room: ($\Delta T = -0.15 \pm 0.53$°F, p-value = 0.02). Outdoor temperature was not significantly different for the week prior to thermoneutral scans versus the week prior to cold scans (thermoneutral scan week: 34.6 ± 16.0°F vs. cold scan week: 34.4 ± 15.5°F, p-value = 0.9).

Coronal PET-CT and MRI images from a representative normal weight and overweight subject are shown in Figure 4.4-1 and Figure 4.4-2, respectively. The normal weight subject shows areas of increased SUV on the cold PET MIP image (Figure 4.4-1 E, red arrows) compared to the warm PET MIP (Figure 4.4-1 A). While not as intense as the normal weight

subject, the overweight subject also shows increased SUV on the cold PET MIP (Figure 4.4-2 E, red arrows). The regions also appear smaller with no accompanying paraspinal depots, which are visible on the normal weight subject. Single coronal slices of CT HU, PET SUV, and MRI FSF (Figure 4.4-1 & Figure 4.4-2: B&F, C&G, and D&H, respectively) are also displayed. The clavicular regions of elevated SUV during the cold scan (Figure 4.4-1 & Figure 4.4-2: G) correspond to regions with the radiodensity of adipose tissue on the CT images (Figure 4.4-1 & Figure 4.4-2: B&F). The same region of adipose tissue is clearly visible on the corresponding MRI FSF images (Figure 4.4-1 & Figure 4.4-2: D&H, white ovals), with FSF values in the range of 50-70% fat. Unlike the uptake of ^{18}F-FDG in the PET images, this region of tissue is visible under both thermoneutral and cold conditions.

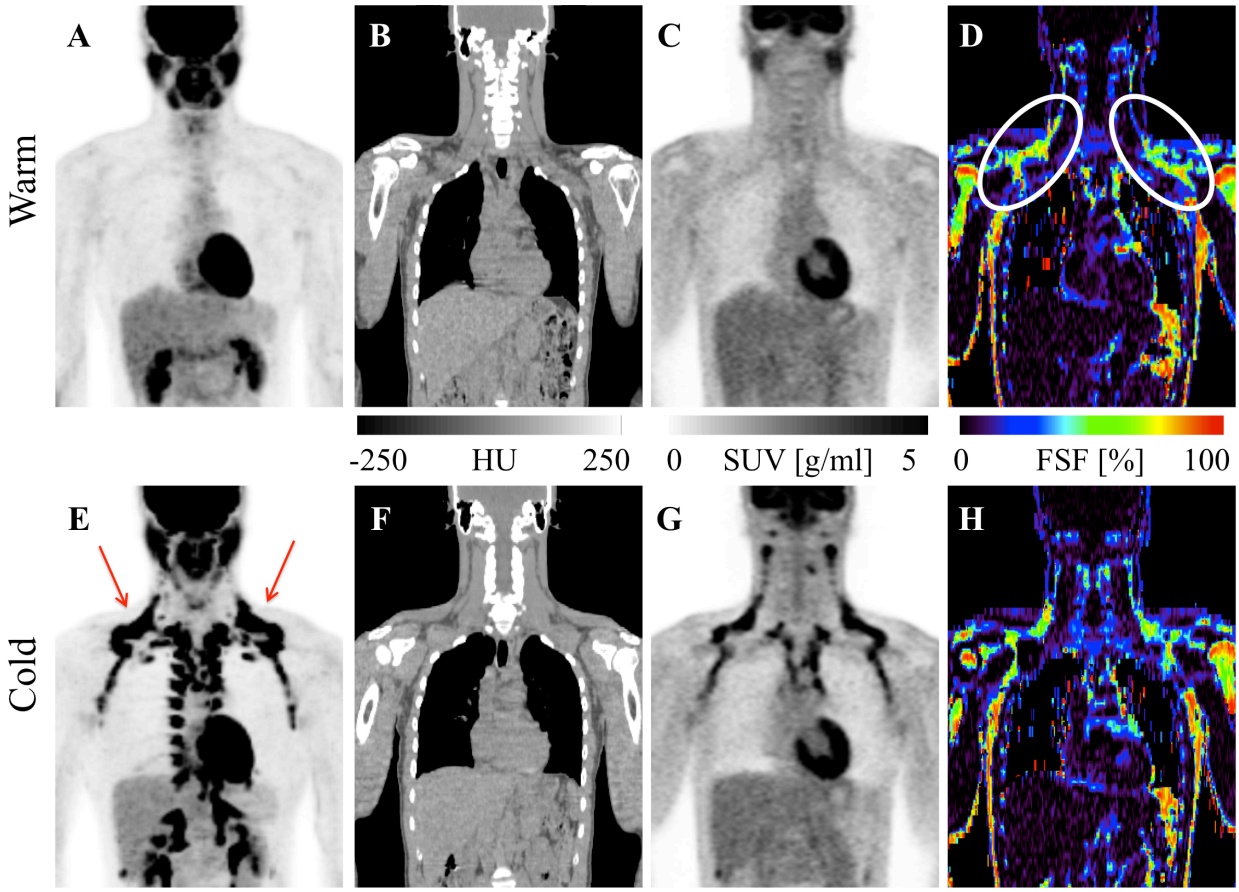

Figure 4.4-1. Example images from the thermoneutral (*A-D*) and cold (*E-H*) scans of a subject from the normal weight group: male, 22 years old, BMI = 20.2 kg/m^2. Uptake of ^{18}F-FDG characteristic of brown adipose tissue is visible in the clavicular area in the cold PET maximum intensity projection (MIP) (red arrows, *E*) and is distinctly absent from the warm PET MIP (*A*). Coronal CT slice shows the region of clavicular tissue with adipose Hounsfield Units (HU) in both the warm and cold scans (*B;F*). The corresponding coronal PET slices (*C;G*) shows the increased standardized uptake value (SUV) in the clavicular adipose tissue after exposure to cold. Coronal slices of the MRI derived fat-signal fraction [%] maps (*D;H*) show clavicular depots with FSF in the range of 60-70% corresponding to the clavicular regions with high SUV on the cold PET scan. This FSF range corresponds to previously published values of BAT. Unlike in the PET scan, this region of tissue is visible on MRI regardless of temperature.

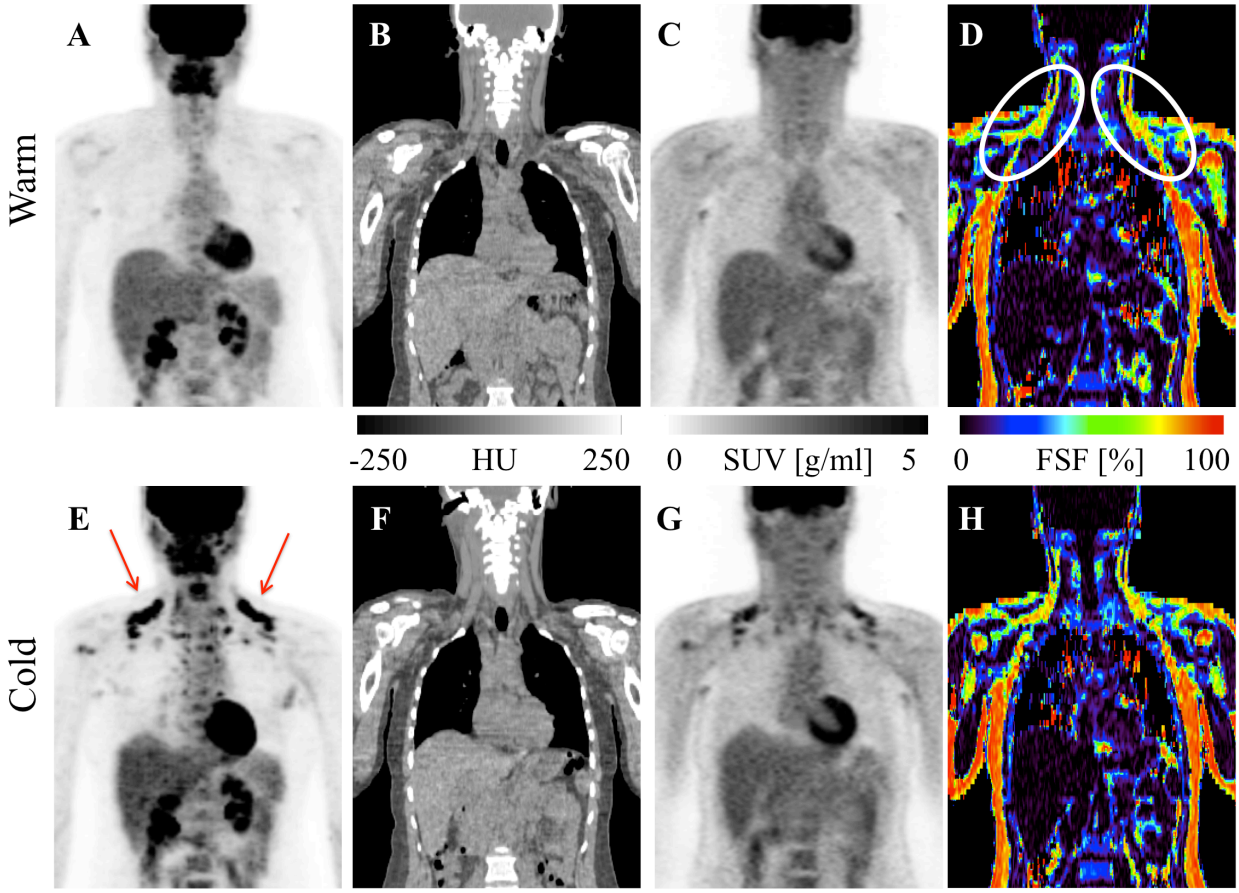

Figure 4.4-2. Example images from the thermoneutral (*A-D*) and cold (*E-H*) scans of a subject from the overweight group: female; 34 years old; BMI = 27.5 kg/m^2. Characteristic uptake of ^{18}F-FDG in brown adipose tissue is visible in the clavicular area in the cold PET maximum intensity projection (MIP) (red arrows, *E*) and is distinctly absent from the warm PET MIP (*A*). Coronal CT slice shows the region of clavicular tissue with adipose Hounsfield Units (HU) in both the warm and cold scans (*B;F*). The corresponding coronal PET slices (*C;G*) shows the increased standardized uptake value (SUV) in the clavicular adipose tissue after exposure to cold. Coronal slices of the MRI derived fat-signal fraction [%] maps (*D;H*) show clavicular depots with FSF in the range of 60-70% corresponding to the clavicular regions with high SUV on the cold PET scan. This FSF range corresponds to previously published values of BAT. Unlike in the PET scan, this region of tissue is visible on MRI regardless of temperature.

Axial slices from the cold scan of the subjects depicted in Figure 4.4-1 and Figure 4.4-2 can be seen in Figure 4.4-3. Though the clavicular BAT volume in the normal and overweight subject are very similar, 25.4 cm^3, and 20.8 cm^3 respectively, the average and maximum BAT SUV for the normal subject is much higher than the overweight subject: normal weight mean

SUV: 7.1 ± 2.8 g/ml, and max SUV: 14.3 g/ml, versus overweight mean SUV: 3.9 ± 1.3 g/ml, and max SUV: 9.32 g/ml. Additionally, the HU values of the normal weight subject are less negative after cold exposure (-59.9 ± 26.9 HU) than after the thermoneutral exposure: (-74.4 ± 31.5 HU). However, this difference in HU values between the two temperatures is not apparent for the overweight subject: cold (-76.1 ± 26.3 HU) versus thermoneutral (-74.6 ± 28.2 HU).

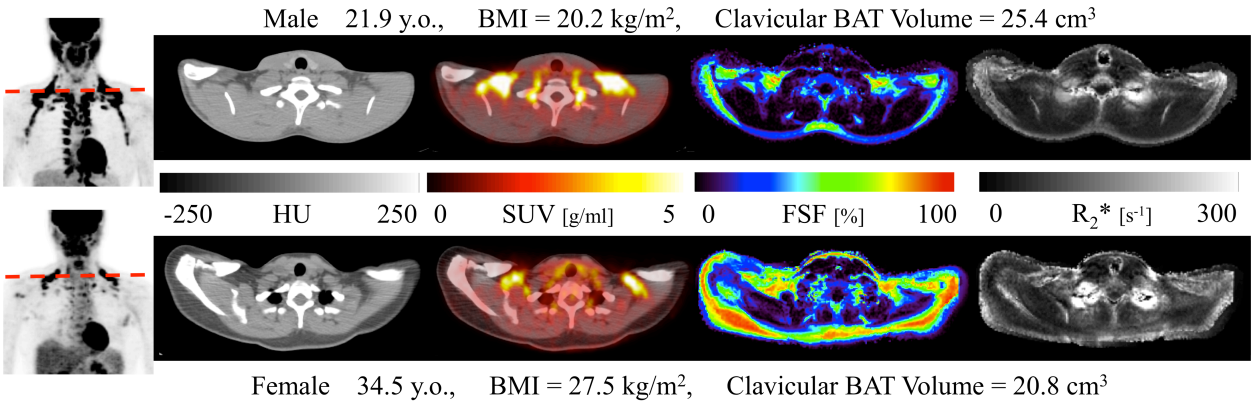

Figure 4.4-3. Clavicular level axial slices from the cold scan of the subjects in **Figure 4.4-1** (top row) and **Figure 4.4-2** (bottom row). The dashed red line on the PET maximum intensity projection (MIP) (left column) indicates the slice of interest. The following four axial images are, in order: CT Hounsfield Unit (HU), PET standardized uptake value (SUV) [g/ml] overlaid on the HU image, MRI derived fat-signal fraction (FSF) map [%], and MRI derived R_2* map [s^{-1}]. Note that while the region of clavicular adipose tissue is of comparable size on the CT HU image for both the normal (top row) and overweight (bottom row) subject, the clavicular adipose tissue in the normal subject has higher SUV over the entire region compared to the lower SUV in the overweight subject. Additionally, the region of tissue on the MRI FSF map corresponding to the adipose tissue on the HU image with increased SUV has a slightly lower FSF in the normal compared to the overweight subject.

The thermoneutral and cold MRI FSF and R_2*, CT HU, and PET SUV values of clavicular BAT from the 17 PET-positive subjects are plotted in Figure 4.4-4. The data are plotted keeping all subjects as a group, as well as for the normal weight and overweight groups. These results show that the FSF, HU, and SUV values are distinct between the thermoneutral and cold scans for the whole group. Specifically, the FSF of clavicular BAT is higher in the

thermoneutral compared to the cold scan for all subjects: thermoneutral: 62.4 ± 6.8% and cold: 60.2 ± 7.6% (p-value < 0.05). Additionally, the mean FSF for normal weight subjects is slightly lower than overweight subjects in both the thermoneutral and cold scans: thermoneutral: 61.0 ± 5.9% vs. 65.7 ± 8.5%, and cold: 59.2 ± 7.0% vs. 62.6 ± 9.4%, respectively. In a similar manner, the mean HU of clavicular BAT for normal weight subjects is slightly less negative than that of overweight subjects in both the thermoneutral and cold scans: thermoneutral: -71.2 ± 10.6 HU vs. -76.7 ± 4.7 HU, and cold: -66.6 ± 10.9 HU vs. -71.5 ± 14.4 HU respectively. Additionally, as expected since it is the currently used definition of BAT, the mean clavicular BAT SUV was significantly higher in all subjects after exposure to cold (5.0 ± 2.0 g/ml) compared to after thermoneutral exposure (0.6 ± 0.5 g/ml, p-value < $1e^{-5}$). Although it tends to be higher, the SUV was not significantly greater in normal weight subjects (5.4 ± 2.1 g/ml) compared to overweight subjects (4.1 ± 1.4 g/ml) after cold exposure (p-value = 0.16).

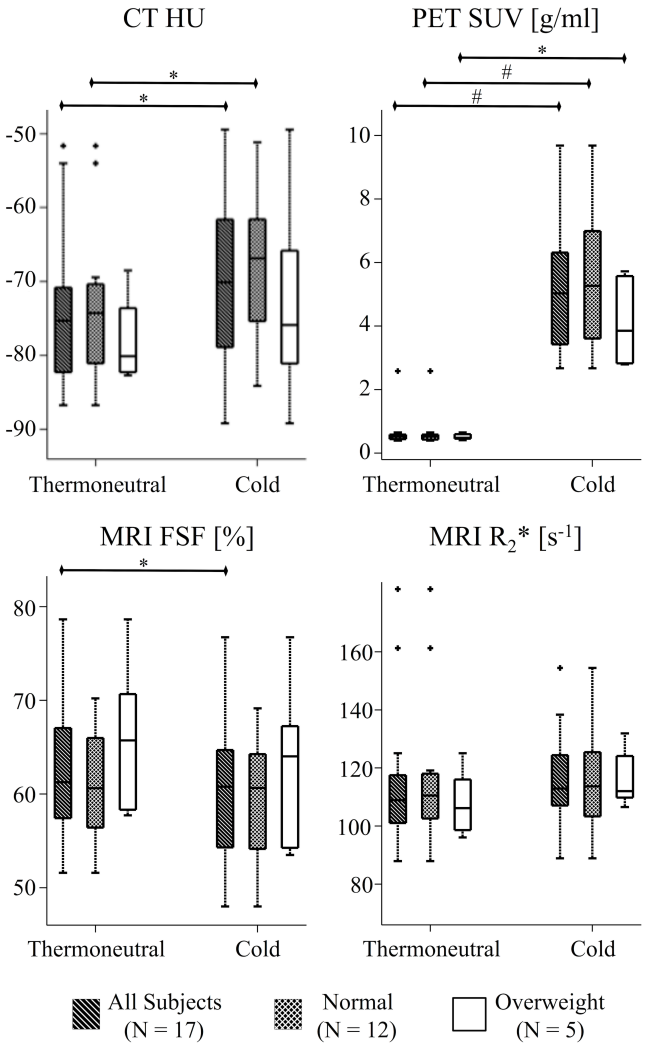

Figure 4.4-4. Box and whisker plots showing the spread of the CT Hounsfield Units [HU], PET Standardized Uptake Value (SUV) [g/ml], Fat-Water MRI derived fat-signal fraction (FSF) [%] and MRI R_2* values from both warm and cold scans. Data values more than 1.5 times the interquartile range are displayed as individual data points either above or below the box and whisker plot. Statistical comparison performed using Wilcoxon signed rank test, * p-value < 0.05, # p-value < 0.01. However, after Bonferroni correction only the comparison of cold PET SUV to warm PET SUV remains significantly different.

The volume of clavicular BAT in the PET-positive subjects was also calculated, and ranged from 1.4 to 57.5 cm^3. Figure 4.4-5 shows the BAT volume plotted versus both age and BMI. Although not significantly different, the volume is slightly greater in normal weight females (32.3 ± 15.6 cm^3) than in normal weight males (21.6 ± 12.5 cm^3), p-value = 0.09.

Multiple linear regression of BAT volume using BMI, sex and waist circumference as predictors, indicates that BMI and sex are significantly correlated to BAT volume (BMI: p-value = 0.04, slope = -5.2; sex: p-value = 0.03, slope = -21.9), but waist circumference and age are not (waist circumference: p-value = 0.07, slope = 6.0; age: p-value = 0.57, slope = 0.8). These results indicate that for example, if all else were held constant, then in males one could expect a 21.9 cm^3 decrease in BAT volume.

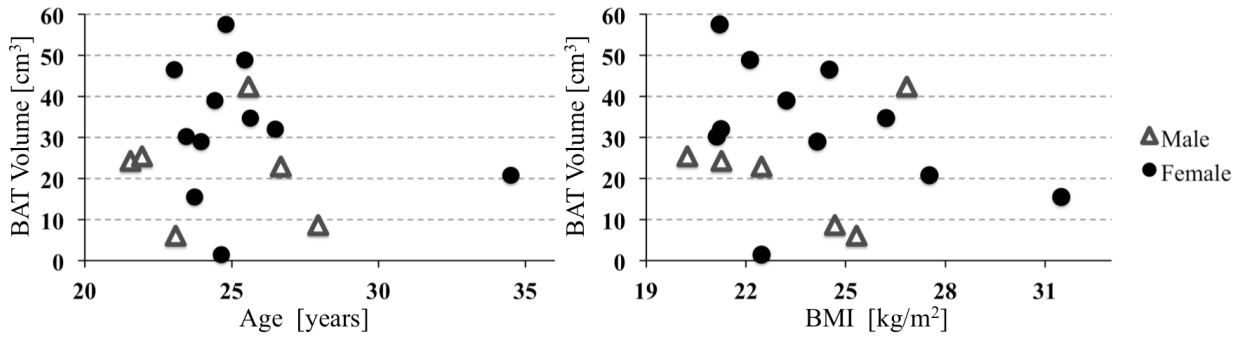

Figure 4.4-5. Clavicular BAT volume versus age (left panel) and BMI (right panel) for all 17 PET-positive subjects. Though there is no statistically significant difference between the volume of BAT in males and females, it appears that females tend to have a larger volume of BAT than men, especially when delineated by BMI.

4.4.3 BAT Compared to WAT

The clavicular BAT values from the 17 PET-positive subjects are plotted in comparison to their subcutaneous WAT values for both the thermoneutral and cold scans in Figure 4.4-6. The work to generate the subcutaneous WAT values is described in CHAPTER 3.

The HU, FSF and R_2* values are all significantly different between the two adipose tissues: the HU values are significantly higher (less negative), the FSF values are significantly lower, and the R_2* values are significantly higher in BAT than WAT. Additionally, the range of

FSF values in BAT is much greater than WAT in both the thermoneutral and cold scans. For example thermoneutral BAT ranges from 51.6% to 78.7% FSF, while thermoneutral WAT ranges from 89.0 to 95.1% FSF.

These results confirm previously published work. For example, the difference in HU values between BAT and WAT was demonstrated in a retrospective study of pediatric patients admitted for PET-CT scans.[209] The results show that in all patients the WAT was more negative than the supraclavicular BAT, specifically in those patients who showed elevated ^{18}F-FDG levels in the clavicular BAT (n=48), the values were -86.7 ± 7.0 HU in WAT, and -62.4 ± 5.3 HU in BAT.

4.4.4 Clavicular Adipose Tissue in PET-Negative Subjects

Also plotted in Figure 4.4-6 are the values of the supraclavicular adipose tissue and subcutaneous WAT from the PET-negative subjects. Their results are plotted next to the BAT and WAT of all 17 PET-positive subjects for comparison. Interestingly, the PET-negative subjects' HU values of both the supraclavicular adipose tissue and subcutaneous WAT are spread across the full range of values seen in the PET-positive subjects (Figure 4.4-6 A). However, both the FSF and R_2* values of the two tissue regions are more tightly clustered and distinguishable for the PET-negative subjects (Figure 4.4-6 B&C). The FSF values of the PET-negative supraclavicular adipose tissue are in the upper quartile of the PET-positive BAT values, indicating a trend towards the WAT values. The R_2* values also reflect this trend, where the PET-negative supraclavicular adipose tissue R_2* values occupy the lower quartile of the PET-positive BAT values, trending towards the lower values seen in WAT. This trend is consistent for both thermoneutral and cold conditions of the FSF and R_2* values.

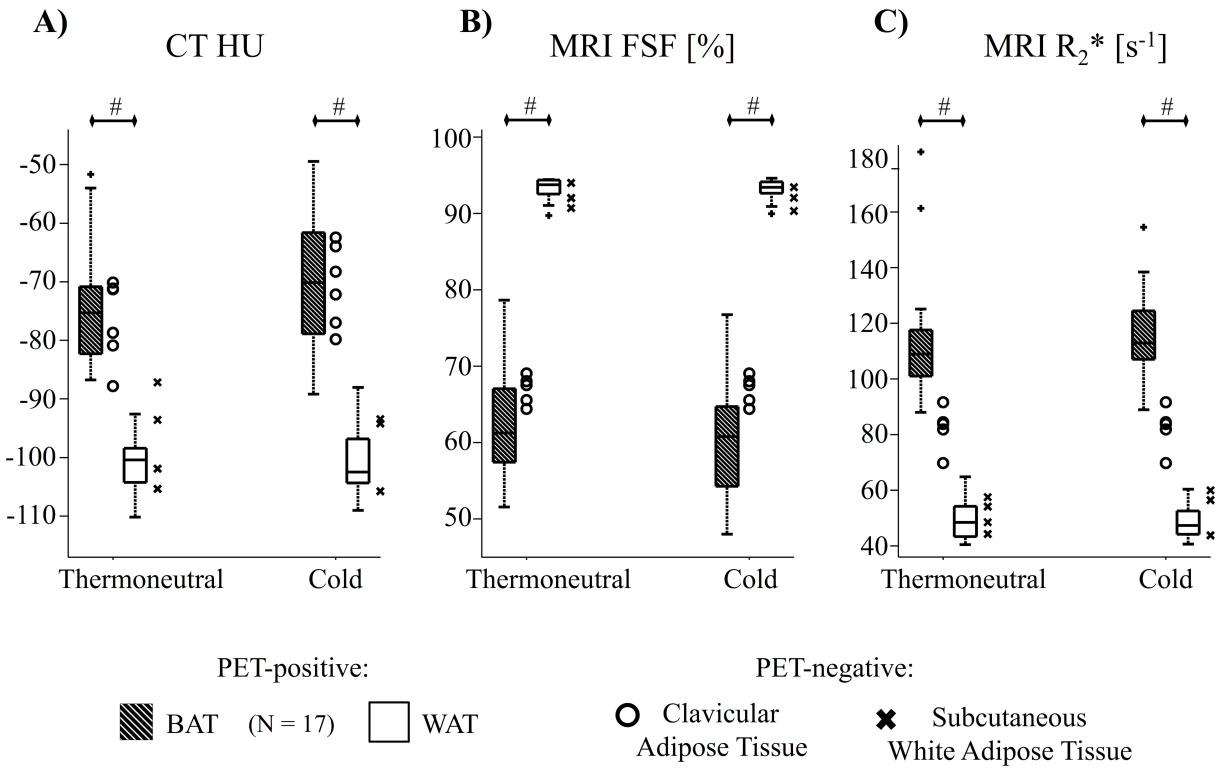

Figure 4.4-6. Comparison of clavicular adipose tissue to umbilicus level subcutaneous white adipose tissue (WAT) in both PET-positive and PET-negative subjects. Data from the clavicular brown adipose tissue (BAT) and subcutaneous WAT of the 17 PET-positive subjects are displayed in box and whisker plots showing the spread of (A) CT Hounsfield Units [HU], (B) MRI derived fat-signal fraction (FSF) [%] and (C) MRI R_2* [s^{-1}] values from both thermoneutral and cold scans. Data values more than 1.5 times the interquartile range are displayed as individual data points either above or below the box and whisker plot. Statistical comparison of BAT to WAT for the 17 PET-positive subjects was performed using Wilcoxon rank sum test: # p-value < 0.001. Data from the PET-negative subjects' clavicular adipose tissue and umbilicus level subcutaneous WAT are plotted to the right of each corresponding box and whisker plot, as black circles and x's, respectively.

4.5 Discussion

Our data suggest that MRI FSF can be used to detect brown adipose regardless of activation status. Furthermore small but significant reductions in the FSF of BAT can be detected

following activation. These findings support MRI as a viable option for studying BAT in adult humans. Additionally, this study extends previous MRI research to quantitatively measure differences in FSF and R_2* values in supraclavicular and subcutaneous adipose tissue depots.[148,210] To the best of our knowledge, this work represents the first study to obtain PET-CT and MRI scans of the same healthy adults after exposure to both thermoneutral and cold temperatures. Our findings support the use of these metrics to characterize and distinguish between BAT and WAT, and lay the foundation for future MRI analysis with the hope that someday MRI-based delineation of BAT can stand on its own. For example, an MRI profile of BAT could be compiled by combining the FSF and R_2* values here described with other previously described metrics such as T_1 (longitudinal relaxation)[211] triglyceride saturation[212] and blood perfusion.[213]

MRI-based detection and delineation of BAT from WAT is advantageous because MRI can detect BAT under thermoneutral conditions, which is not feasible with ^{18}F-FDG PET. MRI-based detection of inactive BAT is possible because the morphological characteristics such as a lower fat fraction and greater mitochondrial content are present even when not active. Our results support this, as both the FSF and R_2* values are statistically different between BAT and WAT even under thermoneutral conditions. Additionally, MRI is capable of distinguishing between active and inactive BAT. For example, the consumption of fatty acids by active BAT may be detected as a decrease in FSF value. This decrease in FSF is seen in our results, where the FSF is on average 2.2% lower after exposure to cold than to warm temperatures, similar to previously published results.[210]

This decrease in FSF is also reflected as a statistically significant increase in the HU values after exposure to cold, as has been previously reported.[170,209] These FSF and HU results

are consistent because as adipose tissue reduces in fat content the HU values become less negative. Additionally, it is interesting to note that the average HU of BAT in overweight subjects are more negative, i.e. more fat-like, than in normal weight subjects, though not significantly different. This difference is again reflected in the FSF values, where the FSF of BAT in overweight subjects is on average higher than that of normal weight subjects. Although many studies report differences in BAT glucose uptake, to our knowledge this is the first report comparing FSF and HU values of clavicular BAT in normal weight to overweight adults.

Additionally, as expected given that increased SUV is the currently accepted biomedical-imaging indicator for activated BAT, the SUV in clavicular BAT is significantly higher after exposure to cold temperatures. Also, though not significantly different, the normal weight subjects show higher mean SUV than the overweight subjects. This may indicate that the BAT in overweight subjects is less responsive to cold stimulus, or that the overweight subjects did not get cold enough to show increased SUV, as has been previously shown.[58,62,63]

Although we measured a significant decrease in the FSF values, the difference was slight. Therefore we note that for future research calculating MRI FSF it is important to reduce the degree to which other factors may contribute to the change in FSF. This can be accomplished in several ways. First, reducing partial volume effects is beneficial. Partial volume effects occur when the tissue of interest (BAT) is averaged with other tissues due to limited imaging resolution. The clavicular adipose depot is very heterogeneous, containing blood vessels, fascia and other tissues. This may contribute to partial volume effects, which can be reduced in part with smaller voxels. The BAT mask applied here was eroded at the outer boundary, helping to mitigate any partial volume effect at the boundary of the adipose depot. Second, to obtain a more accurate fat-water separation, the chemical shift of water due to temperature must be taken into

account. Because BAT releases heat when activated, the tissue becomes warmer than standard body temperature, and the magnetic resonance frequency of water shifts accordingly. Accounting for this chemical shift is not possible with this dataset due to insufficient spectral resolution, i.e., low number of acquired echoes. Third, recent publications indicate the importance of individualized cooling protocols, especially for subjects with higher BMI.[17,214] The cold temperature and cold exposure time duration used here was consistent for all subjects regardless of BMI, and may not have been low enough or long enough to sufficiently cool the overweight subjects. Therefore the BAT in overweight subjects may not have activated, or was not activated for long enough to detect significant lipid oxidation. This is supported in the measurement of the subjects' change in body temperature (ΔT). After two hours of exposure to cold, the body temperature decreased in normal weight subjects (-0.19 ± 0.57, p-value = 0.03) but not in overweight subjects (-0.06 ± 0.40, p-value = 0.34). Taking these three factors into account would help ensure that the measured difference between the thermoneutral and cold FSF values is a result of a true metabolic change in the tissue.

The results of this research show that the MRI properties of FSF and R_2* are capable of distinguishing between clavicular BAT and subcutaneous WAT in adults. Additionally, the separation between the MRI values of BAT and WAT are more clearly distinguishable than the HU values. The R_2* could be detecting blood perfusion in the tissue, or iron content due to higher levels of mitochondria, both of which are significantly higher in BAT compared to WAT.[1,2] These findings support the potential ability of MRI to distinguish BAT from WAT without the use of PET or CT.

In this research, the prevalence of clavicular BAT as determined using the elevated ^{18}F-FDG levels is 20/24 = 83%. This is derived from the 20 PET-activators out of a total of 24

subjects (PET-CT data was not acquired in one subject). Analyzing the clavicular adipose tissue from the PET-negative subjects shows the values in their clavicular adipose depots are more similar to the values seen in the PET-positive subjects. Therefore, if we instead use the FSF and R_2* values to determine the presence of suspected BAT, the prevalence could be closer to 100%. Without biopsy samples of the tissue it is not possible to determine the true prevalence of BAT in this cohort. This illustrates one of the main issues with using PET-CT imaging to detect BAT: it relies on the uptake of ^{18}F-FDG by active brown adipocytes to determine the presence of BAT. Therefore, if no uptake occurs, it is assumed that BAT does not exist in that subject. Previous research shows this is untrue, and that brown adipocytes are present in the supraclavicular adipose depot of subjects who are PET-negative.[110] Biopsy samples of the clavicular adipose depot in these subjects mainly contained unilocular adipocytes, but there existed a scattering of multilocular cells, which stained positive for BAT specific markers such as UCP1.[110] Furthermore, other work shows that the supraclavicular adipose tissue of PET-negative subjects is capable of differentiating *in vitro* into brown adipocytes.[111] These two findings demonstrate that the prevalence of BAT in adults may be higher than PET scans indicate, which is exciting when considering the possible role BAT may play in mitigating the metabolic syndromes.

In conclusion, the present study extends the application of MRI to quantifying the MRI FSF and R_2* properties of BAT in adults. Building on these results with additional MRI-derived properties such as temperature, diffusion, perfusion, and T_1, MRI will likely be able to distinguish BAT without human subjectivity, even if the tissue is not active. Because some subjects that are PET-negative do have BAT, it is important to develop a technique for detecting BAT that does not rely solely on the rate of glucose metabolism. Additionally, the ability to distinguish BAT without ionizing radiation would enable BAT to be studied in larger cohorts, in

longitudinal studies, and in difficult populations such as pediatrics, which could further our understanding of the role BAT plays in humans.

CHAPTER 5

PROGRESS TOWARDS AUTOMATIC CLASSIFICATION

5.1 Introduction

One aim of our research is to develop a method for automated classification of BAT using statistical analysis of biomedical imaging properties of known BAT and non-BAT voxels. Many previous studies have investigated BAT, but often each study uses a different method for determining what constitutes BAT.[11,148,206,207] In this study we acquire four quantitative measurements for each subject: Fat-water MRI derived FSF and R_2* relaxation rate, CT HU, and PET SUV, with the purpose of determining what combination of these four quantitative measurements can be used to reliably and automatically classify BAT. While uptake of the radiotracer ^{18}F-FDG is accepted as an indication of BAT there are several drawbacks[17] of using this as a sole indicator of BAT. One reason is due to elevated ^{18}F-FDG uptake in tissues other than BAT, such as the heart, salivary glands, and muscles. Furthermore, exploring the ability of quantitative MR properties to classify BAT could reduce radiation exposure in future studies using only MRI, as well as support investigations using emerging PET-MR systems.

5.2 Subjects and Image Acquisition

Out of the enrolled subjects described in Section 2.1, ten PET-positive subjects were included for this study (2 males, 8 females, aged 22 to 41 years, with a BMI of 20.24 to 27.52 kg/m^2).

The MRI data processed for this project are taken from the 4x2-interleaved echo imFFE scan previously described in Section 2.3.2. The fat, water, and R_2* maps were reconstructed using the complex method previously described in Section 2.4.1, using the 9-peak fat model outlined in section 2.4.1. Image registration was performed using the method described in Section 2.4.2.

5.3 Random Forest Machine Learning

5.3.1 Random Forest Algorithm

The training algorithm for the random forest was performed using the MATLAB function *TreeBagger*. This function creates an ensemble of bagged decision trees, in this case using 100 trees, for predicting the "BAT" and "not-BAT" classification using the four values (FSF, R_2*, HU, SUV) from images of the three training subjects. This training ensemble was calculated for all 15 combinations of the four predictors (FSF, R_2*, HU and SUV). The list of these 15 combinations is presented in Table 5.3-1. Results from training with these 15 combinations of data were then applied to the unclassified data from the remaining seven subjects to predict the probability of voxels being classified as either BAT or not-BAT.

Table 5.3-1. Random forest data combinations.

Image Type Combination	MPaKmax	AUC
R	0.033	0.632
FR	0.094	0.705
H	0.096	0.882
RH	0.103	0.785
F	0.109	0.842
FH	0.181	0.860
FRH	0.188	0.900
S	0.491	0.972
RS	0.555	0.977
FS	0.701	0.984
FRS	0.704	0.985
HS	0.760	0.994
RHS	0.774	0.994
FRHS	0.796	0.995
FHS	0.832	0.996

The 15 combinations of data (F = FSF, R = R_2*, H = HU and S = SUV) and the corresponding results acquired by applying the random forest regression analysis for each image type combination to the unclassified data for all seven subjects. For each image type combination the mean precision at Kmax (MPatKmax), where Kmax is the total number of true voxels in the BAT mask, and the corresponding area under the curve (AUC) is reported, showing the varying degrees of reliability in predicting BAT. The data combinations are sorted by increasing values of MPatKmax.

5.3.2 Training Data

The resulting ROIs formed subject-specific "BAT masks". After creating the BAT masks, a range of seven slices was selected at the clavicular level for each subject, covering the main site of supraclavicular BAT. All data presented here comes from these seven slices for each subject. After using all four scans to create the BAT mask for each subject, the data used for all further analysis reported here comes from the cold PET-CT and cold MRI scans only.

The second step was to select three of the ten subjects to form the training dataset for use with a random forest machine-learning algorithm.[215] For each of these three subjects a second

mask of “not-BAT” voxels was created for the selected range of seven slices per subject. This mask was formed by taking the union of all voxels containing signal on both the coregistered FWMRI and PET-CT scans, creating a “foreground” image. Then using binary morphology, the previously created BAT mask was dilated by 5 voxels and subtracted from this “foreground” image. This generated a mask that did not include the original BAT-mask voxels, i.e. the “not-BAT” mask, as seen in Figure 5.3-1.

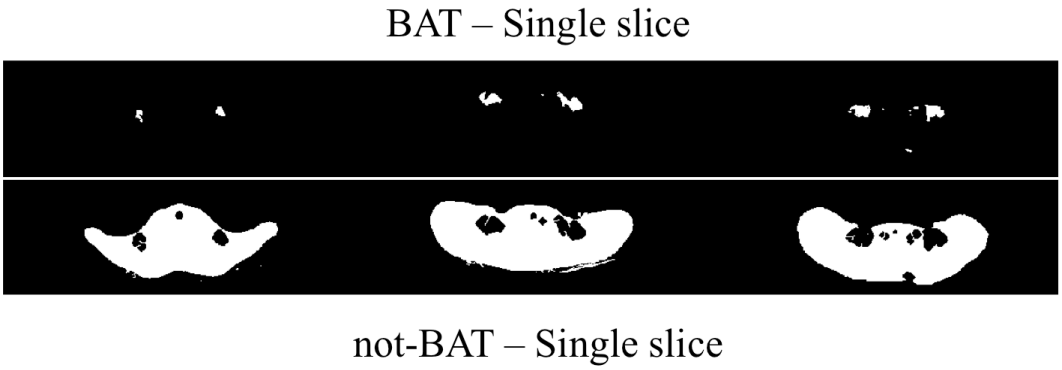

Figure 5.3-1. Random forest training masks of the “BAT” (top row) and “not-BAT” (bottom row) regions from three example subjects. These show single axial slices of the BAT masks and corresponding “not-BAT” masks for three subjects.

The BAT and not-BAT masks were then applied to the coregistered images of the three selected subjects to obtain the FSF, R_2* relaxation rate, HU and SUV values for each voxel within the BAT and not-BAT regions. These four quantitative values of BAT and not-BAT voxels were then used as the training data in a random forest analysis.

5.4 Results

All data presented here are the result of processing all seven subjects as a unit. To analyze this unclassified data, only the union of all voxels that contain signal on both the coregistered FWMRI and PET-CT scans were considered. This mask, which was formed from a

union of foreground voxels, was applied to the coregistered data to obtain the FSF, R_2*, HU and SUV in an unclassified state. These four values were combined in 15 ways (as listed in Table 5.3-1) and predictions were calculated based on the corresponding tree bagging ensemble results from the training data. This calculated the predicted probability (from 0 to 1) for each voxel to be BAT. The resulting mean precision at K (MPatK), where K is the total number of voxels in the BAT mask, and area under the curve (AUC) were calculated for the seven slices from all 10 subjects combined (Kmax = 18,902 voxels).

5.4.1 Predictions

Table 5.3-1 shows the list of data pairings (F = FSF, R = R_2*, S = SUV, H = HU), with each corresponding MPatK and AUC. From these results the combination of FHS produces the best MPatK (0.832) with a corresponding AUC of 0.996. While relying on either R_2*, HU or FSF alone results in a low probability of correctly predicting BAT voxels (MPatK of 0.033, 0.096, and 0.109 respectively), combining any one of these values to SUV results in a higher MPatK (0.555, 0.760, and 0.701 respectively) than using SUV alone which results in a MPatK of 0.491. Example plots of the MPatK for increasing values of K for the SUV and HU-SUV, and FSF-HU-SUV combinations are shown in Figure 5.4-1.

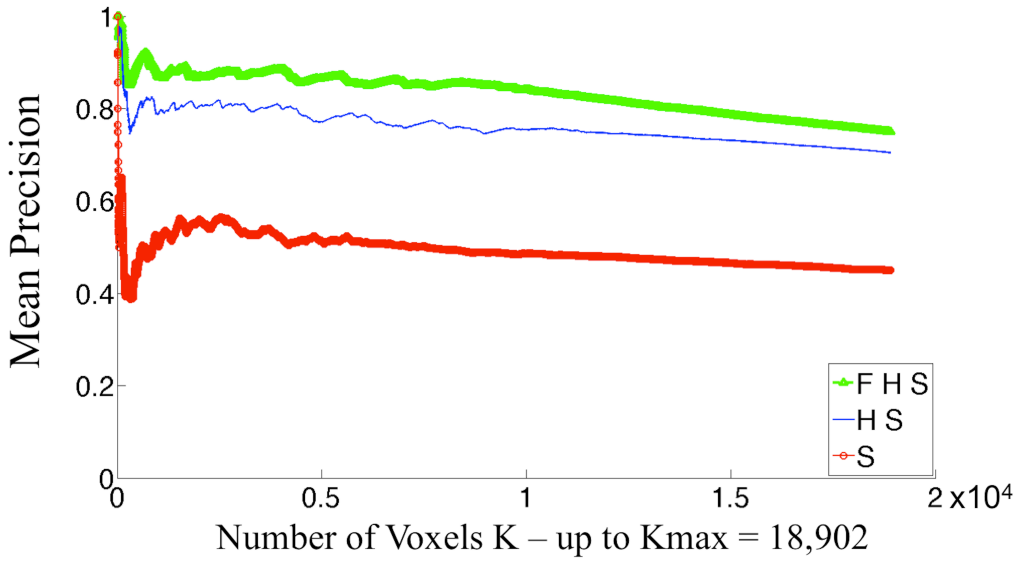

Figure 5.4-1. Plots of the mean precision at K (MPatK) for increasing values of K up to Kmax = 18,902, where Kmax is the total number of voxels in the supraclavicular BAT masks for all 7 subjects processed together. The lowest calculated precision plotted here results from processing SUV data alone. Adding HU data to SUV (the HS line) increases the precision, with the highest precision coming from combining the FSF, HU and SUV (FHS) data.

5.4.2 Anatomically Difficult Regions

Due to the lack of elevated ^{18}F-FDG uptake in tissue other than BAT, this classification method may be expected to perform well in the limited clavicular region analyzed here. However, BAT depots can extend both up into the neck and down into the torso. Both of these regions are potentially more difficult to classify due to additional elevated ^{18}F-FDG uptake in tissues besides BAT, such as the heart and salivary glands. Therefore, in order to test the robustness of this analysis method, the same random forest predictor applied in the clavicular region was also applied to a challenging slice in both the neck and upper torso of one subject. Figure 5.4-2 shows the axial slice through the neck of one subject, showing regions of elevated SUV in both the jaw and back of the neck. None of the regions of elevated SUV seen in Figure 5.4-2c) are considered BAT using the same rules that created the BAT mask in the clavicular

region. However, processing these data using SUV alone falsely calculates a high probability that this is BAT, as seen in Figure 5.4-2d). By adding FSF to SUV in the analysis lowers the probability (Figure 5.4-2e), and adding R_2* to FSF and SUV lowers the probability even further (Figure 5.4-2f). These promising results demonstrate that adding FWMRI-derived metrics to the analysis gives additional information to correctly lower the probability of classifying this region as BAT in a difficult anatomical slice.

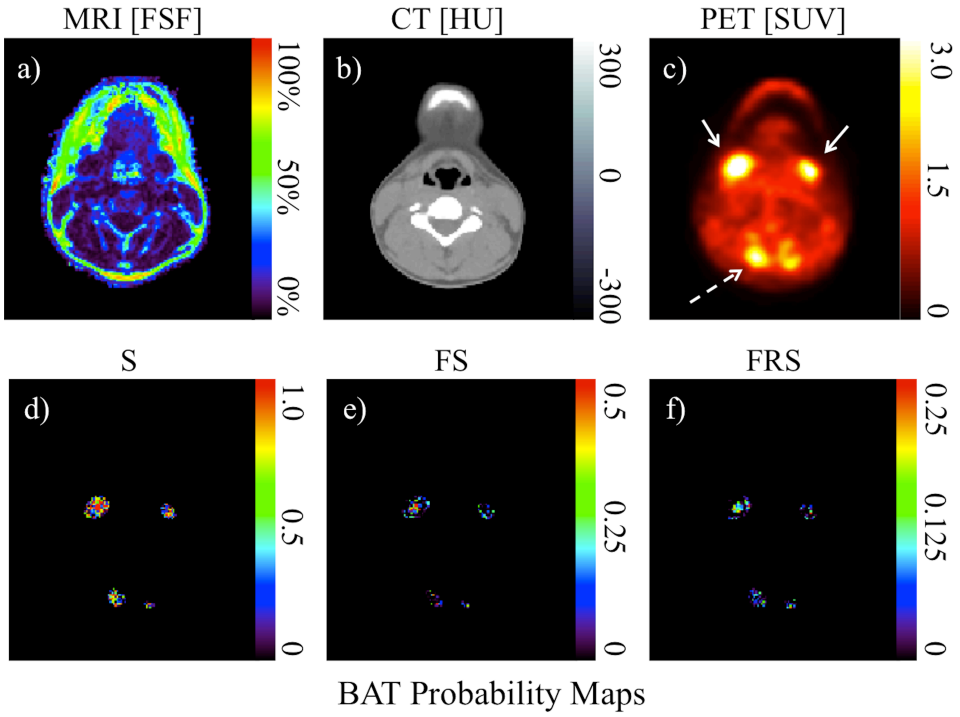

Figure 5.4-2. Axial images and BAT probability maps in the neck of one subject. The axial images are a) MRI [FSF], b) CT [HU] and c) PET [SUV] from the coregistered cold scans. The regions of increased SUV in both the jaw (solid white arrows) and back of the neck (dashed white arrow) are not included in the originally created BAT mask. However, after application of the random forest predictor, these regions have a high probability of being BAT as determined by SUV alone (d). Analysis using FSF and SUV combined lowers the probability greatly (e), and analysis using FSF, R_2* and SUV together lowers the probability even further. Note the differences in scale on the probability maps.

Analysis of the slice in the upper torso shows similarly encouraging results, as seen in Figure 5.4-3. The BAT and not-BAT masks generated for this slice using the rules described above are shown in Figure 5.4-3a) and 3b) respectively. The regions of increased SUV in the axilla seen in Figure 5.4-3f) (white arrows) are identified as BAT in the BAT mask. These correspond to areas of FSF in the 60-80% range as seen in the MRI FSF image in Figure 5.4-3c), which matches known BAT values. Additionally, the region of increased SUV near the spinal column marked by the dashed white arrow in Figure 5.4-3e) could be BAT, as it has both elevated SUV and adipose tissue HU values, and this is a known location for BAT to exist. This region near the spinal cord was likely not included in the BAT mask in Figure 5.4-3a) because it was eliminated from the mask due to the 15-voxel-neighborhood rule. Analyzing this slice using the same random forest predictor used in the supraclavicular BAT depots shows promising results. Using SUV alone in the analysis correctly predicts the two BAT depots with a relatively high degree of certainty as seen in the probability map in Figure 5.4-3f). Analysis of FSF and SUV together (Figure 5.4-3g) and FSF, R_2* and SUV (Figure 5.4-3h) shows an increase in the probability that these axilla regions are BAT compared to analysis with SUV alone. Additionally, the region of increased SUV located next to the spinal column is detected in all cases, however with a lower probability. Note that all three probability maps in Figure 5.4-3 are displayed using the same scale.

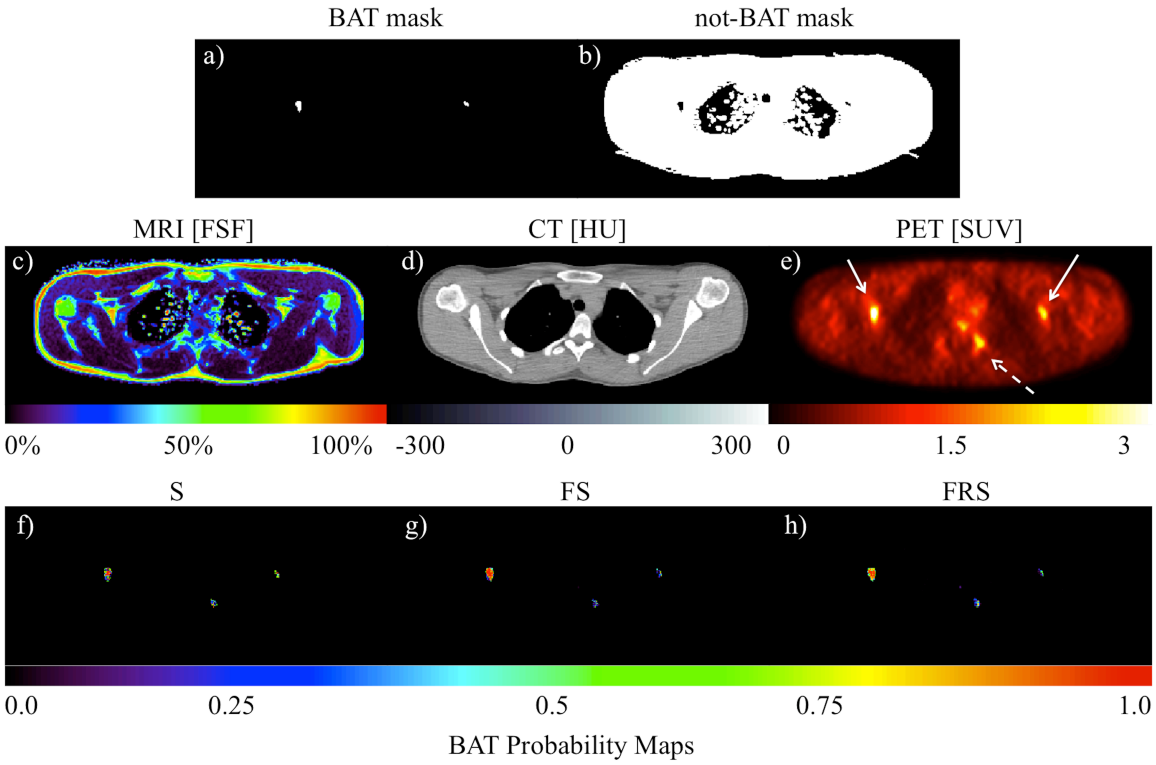

Figure 5.4-3. Axial images and BAT probability maps in the chest of one subject. The axial images are c) MRI [FSF], d) CT [HU] and e) PET [SUV] maps. Panels a) and b) show the corresponding slice of the automatically generated BAT and "not-BAT' masks respectively. When the random forest predictor is applied, the regions of increased SUV in the axilla region (solid white arrows) should be categorized as BAT as seen in the BAT mask (a). The depots indicated by the white arrows are successfully determined to be BAT by f) SUV alone, but the probability is increased by analyzing either e) FSF and SUV together, or f) FSF, R_2* and SUV. The smaller nodule (dashed white arrow) along the spine is also classified as BAT, although with a lower probability. Note that all three probability maps have the same scale.

5.5 Conclusion

In this study we developed a prototype automated segmentation method based on properties obtained from fat-water MRI and PET-CT scans acquired on ten healthy adult subjects. A random forest machine-learning algorithm using combinations of metrics from Fat-Water MRI and PET-CT was able to successfully classify voxels as BAT. When applied to unclassified data in the supraclavicular region, these ensembles successfully predict the same regions that are previously determined to be BAT. Additionally, analysis in more challenging

anatomical regions also produce promising results, both successfully predicting low probabilities for regions which are not BAT as well as predicting regions which are BAT with high probability. Hence, given various combinations of FSF, R_2*, HU and SUV data it is possible to segment BAT in a purely automated fashion with varying degrees of precision.

These preliminary results demonstrate the potential for successful automatic segmentation of human brown adipose tissue using MRI and PET-CT properties. Although this method relies heavily on accurate registration between datasets, it shows promise for the ability to segment BAT from other tissues without manual intervention. Furthermore, results indicate the possible utility of emerging PET-MR systems. Given that the regression analysis performed here was on cold scans only, future work should include determining the ability to segment BAT using only thermoneutral data. This is a more challenging problem, as the BAT depots are not as easily determined because the SUV is not elevated in the BAT depots when they are not exposed to cold. Therefore, it may be useful to include additional quantitative MRI measurements such as diffusion, temperature, and T_1 values to enhance the performance of segmentation based on MRI alone. Doing so could ultimately eliminate the need to include PET or CT data in order to successfully classify and segment BAT depots.

CHAPTER 6

ADDITIONAL MRI PROPERTIES OF BAT

6.1 Triglyceride Mapping

In the ongoing effort to quantify the MRI-derived characteristics of BAT, one area of interest is quantifying triglyceride characteristics. This work aims to develop and improve methods based on fat-water MRI (FWMRI) for triglyceride characterization in vivo. Previous work in murine models shows differences in triglyceride characteristics in various adipose tissue depots. To expand upon this previous work, the aim of this research is to use FWMRI methods to characterize triglycerides properties in human adipose tissue. Characterizing the triglyceride properties of BAT could provide an additional metric for distinguishing BAT from WAT, adding to the MRI "fingerprint" of BAT properties, which would allow segmentation of BAT without additional imaging such as PET.

Previous work in humans shows that the composition of stored lipids in adipose tissue is related to diet,[216] and in rabbits the ratio of polyunsaturated to saturated fatty acids (SFA) is related to the unsaturation level of dietary fat.[217] Additionally, it is important to understand the spatial distribution of polyunsaturated fatty acids (PUFA) as they stimulate BAT to activate,[218] and rats fed fish oil, which is highly unsaturated, show a difference in PUFA distribution between BAT and WAT.[219] It is also important to understand the spatial location of PUFAs and SFAs, as work has shown that PUFAs limit adipocyte lipid droplet size and differentiation in comparison to SFAs.[220]

This work aims to quantify the saturation fraction (SF), mono-unsaturated fraction (MUF), and poly-unsaturated fraction (PUF) of triglycerides. The triglyceride in Figure 6.1-1 shows a saturated fatty acid (top fatty acid), and a mono- and poly-unsaturated fatty acid (middle and bottom fatty acid, respectively).

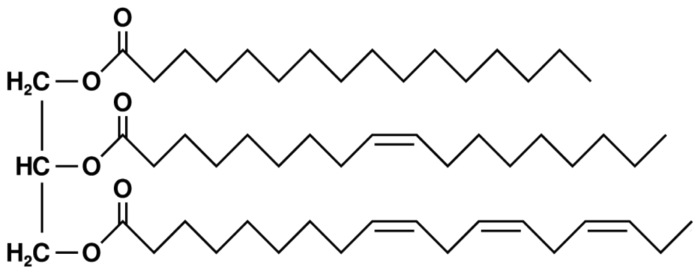

Figure 6.1-1. Triglyceride representation, showing three types of fatty acids: Saturated (top), mono-unsaturated (middle), and poly-unsaturated (bottom).

Of the many differences between BAT and WAT, it appears from previous research that the triglyceride content of the two adipose tissues is also different. Two studies of excised murine BAT and WAT were conducted using spectroscopy.[211,221] In 1994, Zancanaro et al. used MR spectroscopy to study BAT from two groups of rats, one group housed at normal room temperature (20-23°C) for two weeks, and one group housed at 4°C for two weeks.[221] Their results showed that BAT harvested from rats kept in the cold was more saturated than the BAT harvested from rats at room temperature. In 2011 Hamilton et al. also acquired MR spectroscopy data on BAT and WAT harvested from mice housed at 22°C.[211] Their results indicated that BAT was more saturated than WAT, even though the animals were not housed in cold conditions. Building off these previous results, we aim to characterize the triglyceride content of BAT and WAT in humans using MRI.

6.1.1 Phantom and Subject Setup

The data for this study was acquired in both a phantom and healthy adult humans using the same MRI sequence. The phantom, pictured in Figure 6.1-2, was made using seven oils: 1-Red Palm, 2-Flax, 3-Olive, 4-Sunflower, 5-Pumpkin, 6-Coconut, and 7-Sesame. This phantom was created to test and verify the scan acquisition and processing methods prior to processing human data. The human data presented here comes from 8 of the PET-positive subjects (4 male), aged 24.5 ± 3.7 years, with a BMI = 25.8 ± 3.6 kg/m^2.

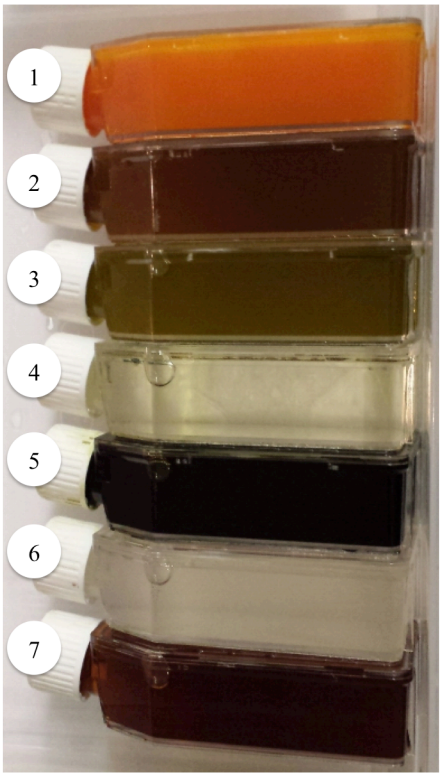

Figure 6.1-2. Seven-oil phantom.

6.1.2 Processing Methods

The MRI sequence acquired was the high-resolution 12-echo (4 echoes x 3 interleaves) imFFE scan, as described in section 2.3.2.

The first step to process the data involved the standard fat-water separation technique, with the 9-peak fat spectral model, as described in 2.4.1. This resulted in an initial R_2*, ΔB_0 and FSF map, as seen in Figure 6.1-3 panel A). These resulting maps, along with the original complex data, were then fed into a voxel-by-voxel non-linear least squares fat-water fitting model. This second fat-water non-linear optimization used a model allowing the fat spectral model to be fit, and again the first echo of each interleave was discarded. This second processing step resulted in updated R_2*, ΔB_0 and FSF maps, as seen in Figure 6.1-3 panel B).

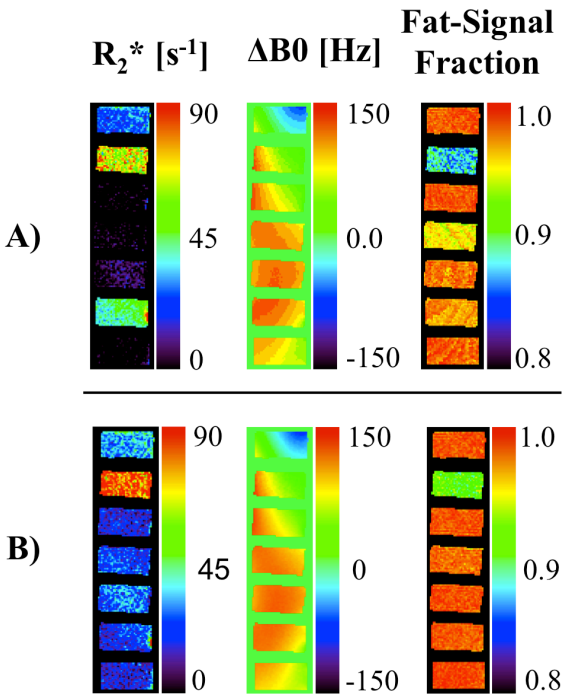

Figure 6.1-3. Results from the two-part fat-water separation processing.

6.1.3 Initial Results

Also resulting from this second least squares fitting process were the triglyceride characterization maps, as seen in Figure 6.1-4.

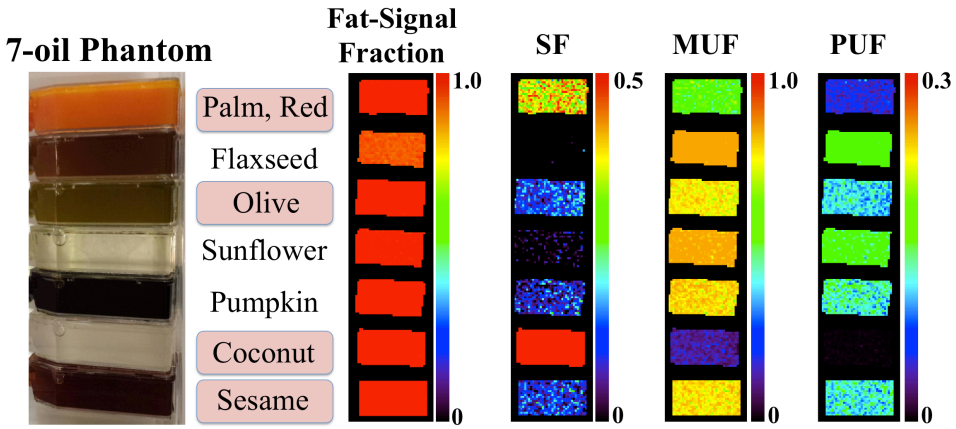

Figure 6.1-4. Resulting fat signal fraction and triglyceride maps from the 7-oil phantom depicted in **Figure 6.1-2**. SF = saturation fraction, MUF = mono-unsaturated fraction, PUF = poly-unsaturated fraction. The four oils highlighted with red squares are compared in **Figure 6.1-5** to both USDA oil values and previous work by Hamilton et al.[211]

To verify our findings, we compared the results from four of the phantom oils to the values found in the United States Department of Agriculture (USDA) database, as well as to gas liquid chromatography work performed by Hamilton et al.[211] The four oils highlighted in red boxes in Figure 6.1-4 are the oils we have comparison data from both the USDA and previous gas liquid chromatography work by Hamilton et al.[211] These results are plotted in Figure 6.1-5.

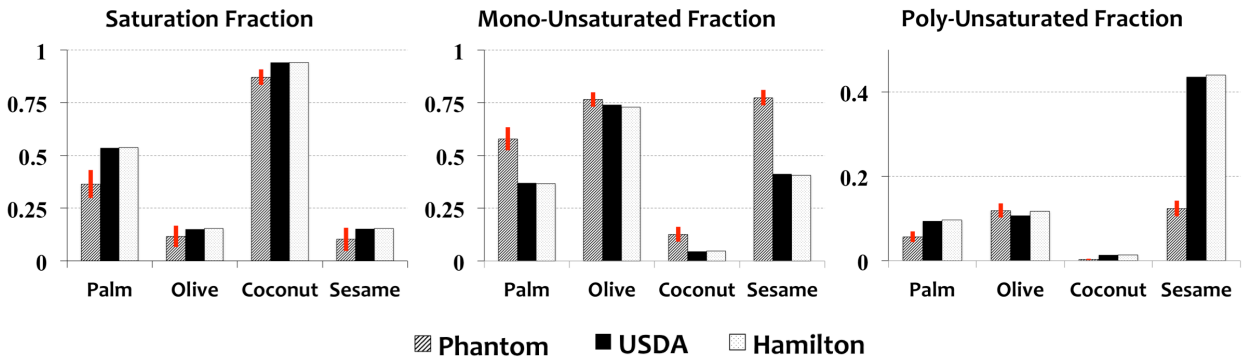

Figure 6.1-5. MRI oil phantom results plotted versus oils from both USDA and Hamilton et al.[211] Values are plotted as means ± SD. Discrepancies between palm and sesame oils are potentially due to slight differences in oil types (ex: red palm vs. palm, toasted sesame vs. sesame).

These phantom results show promise in the ability of MRI-derived triglyceride characterization to distinguish the SF, MUF and PUF values. Because gas-liquid chromatography (GLC) was not performed on these four oils, it is unknown if the discrepancies between our results and the USDA values are due to inherent differences in our oils, or because the MRI analysis was incorrect. This can be addressed in future work by also obtaining GLC values on the oils.

The same 4x3 echo imFFE scan, acquired on the previously described human subjects, was processed in the identical manner as the oil phantom processing. The results images from one subject are displayed in Figure 6.1-6, showing the FSF image along with the triglyceride SF, MUF, and PUF maps. The images are masked to only show pixels with FSF > 40%, as this triglyceride characterization method is only expected to work in pixels with significant fat content.

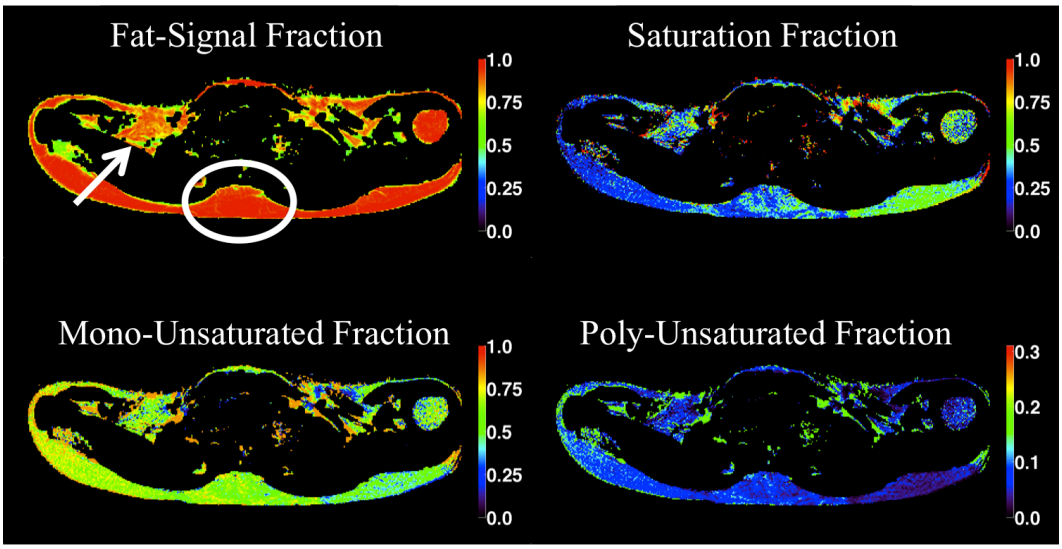

Figure 6.1-6. Clavicular level axial slice showing resulting triglyceride processing maps. The images are masked to show pixels containing >40% fat. BAT data were taken from the clavicular adipose tissue (white arrow) with confirmed elevated ^{18}F-FDG levels. WAT data were taken from the subcutaneous adipose in the mid-back (white circle).

The triglyceride characterization values from regions of interest (ROI) in both BAT and WAT are plotted in Figure 6.1-7. The clavicular BAT ROI was defined using the same BAT mask described in section 4.3, an example BAT region is indicated by the white arrow on the FSF image in Figure 6.1-6. The subcutaneous WAT ROI was taken from the middle of the back, as indicated by the white circle on the FSF image in Figure 6.1-6. The values from the eight subjects are plotted (means ± SD) in comparison to excised murine BAT and WAT tissue scanned at 3.0 Tesla by Hamilton et al.[211]

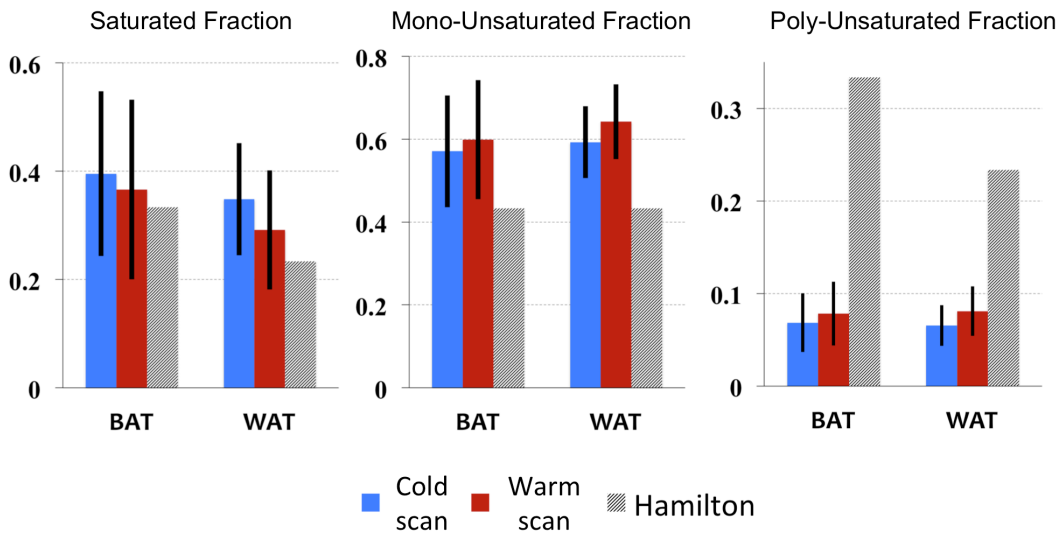

Figure 6.1-7. Human data plotted versus excised murine BAT and WAT scanned at 3.0 Tesla by Hamilton et al.[211] Saturation fraction shows higher mean saturation in BAT compared to WAT, though not statistically significant.

These plots indicate that the MRI-based triglyceride characterization method is promising and potentially capable of enhancing our understanding of BAT and WAT morphology. Because the tissue that we are comparing our results to is excised, not in vivo, murine tissue this complicates the ability to truly compare the results. Therefore it is even more important to ensure the triglyceride characterization method is accurate through validating the results against accepted GLC values.

6.1.4 Discussion and Conclusion

This work shows promising preliminary progress towards characterizing triglycerides using fat-water MRI. Future analysis will include further adjustment of the least-squares fitting parameters in calculating the triglyceride characteristics, and acquiring and processing data with a range of both number of echoes and echo spacing to sample different spectral resolutions and bandwidths. Our results can then be compared to previous reports of triglyceride characterization

using MRI of oils and humans.[144,222,223] This work is novel in the attempt to quantify human BAT and WAT triglyceride characteristics with phantom scan validation.

This study demonstrates the ability to quantify triglycerides in both white and brown adipose tissue in healthy adults with a variety of ages and BMI levels.

6.2 Temperature Mapping

One of the most important aspects of detecting and quantifying the properties of BAT involves detecting differences between the active and inactive states of the tissue. PET imaging with ^{18}F-FDG has become the de facto standard for differentiating between active and inactive BAT. However, as was discussed in section 4.4 there are issues with using ^{18}F-FDG PET as a definitive metric. Additionally, CT has been shown to detect differences between active and inactive BAT. For example in rats scanned once after four hours at room temperature and again after four hours at 4°C. The results showed that after exposure to cold, BAT had a significantly higher HU than after exposure to room temperature: -12.4 ± 22.4HU versus -27.9 ± 9.6HU, respectively.[170]

One definitive result of activated BAT is the release of heat. Therefore the ability to measure a temperature increase of the tissue would enable a clearer and perhaps more reliable distinction between active and inactive BAT. The purpose of this work is to apply a novel FWMRI method with explicit modeling of temperature-dependent water frequency offset to scans of activated and non-activated BAT in adult human subjects to demonstrate the method's ability to distinguish between the BAT states.

6.2.1 Processing Methods

The high-resolution imFFE scan with 12 echoes (4x3 interleaved echoes) was processed for this study (see section 2.3.2). Conventional fat-water separation based on a multi-scale whole-image optimization algorithm[163] was performed for each dynamic. Fat was modeled using a 9-peak spectral model.[144] The first echo of each four-echo train was discarded to avoid potential contamination by eddy currents in the complex fat-water signal model. Results of the conventional fat-water separation were used to initialize a modified version of the mixed (magnitude and complex) signal-fitting algorithm available in the International Society for Magnetic Resonance in Medicine (ISMRM) Fat Water Toolbox.[224] The mixed signal fitting function was then modified to additionally solve for a temperature-dependent frequency shift of the water peak, as shown in Equation [1.4-22].

After completion of the voxel-by-voxel fitting algorithm, a mask was created of the clavicular adipose tissue region. Instead of using the same BAT mask as described in section 0, a new mask was created. This is because the original BAT mask was created using rules which only apply to those subjects showing increased ^{18}F-FDG uptake after exposure to cold, and this temperature mapping method aims to be applicable to all subjects, regardless of the cold PET status. To create the temperature based mapping, the following six rules were applied to each voxel in the MR image: FSF > 40% fat, $R_2^* < 200s^{-1}$, post-fitting residual $< 3*10^7$, -20°C < voxel < 20°C, -1000Hz < B_0 < 1000Hz, and the voxel-fitting exited successfully. This largely limited the mask to the desired clavicular regions, with a few additional regions, as seen in the "Resulting full mask" in Figure 6.2-1. The mask was then cleaned, removing any voxels where the gradient between a voxel and its neighbor was greater than 10%. This helped remove the partial voluming present at the boundary between fatty and lean tissue. If these steps did not

completely remove all the undesired regions, then the clavicular regions were manually selected on a slice-by-slice basis using the MATLAB function *bwselect()*. An example single axial slice showing the final clavicular mask is shown in the last panel of Figure 6.2-1.

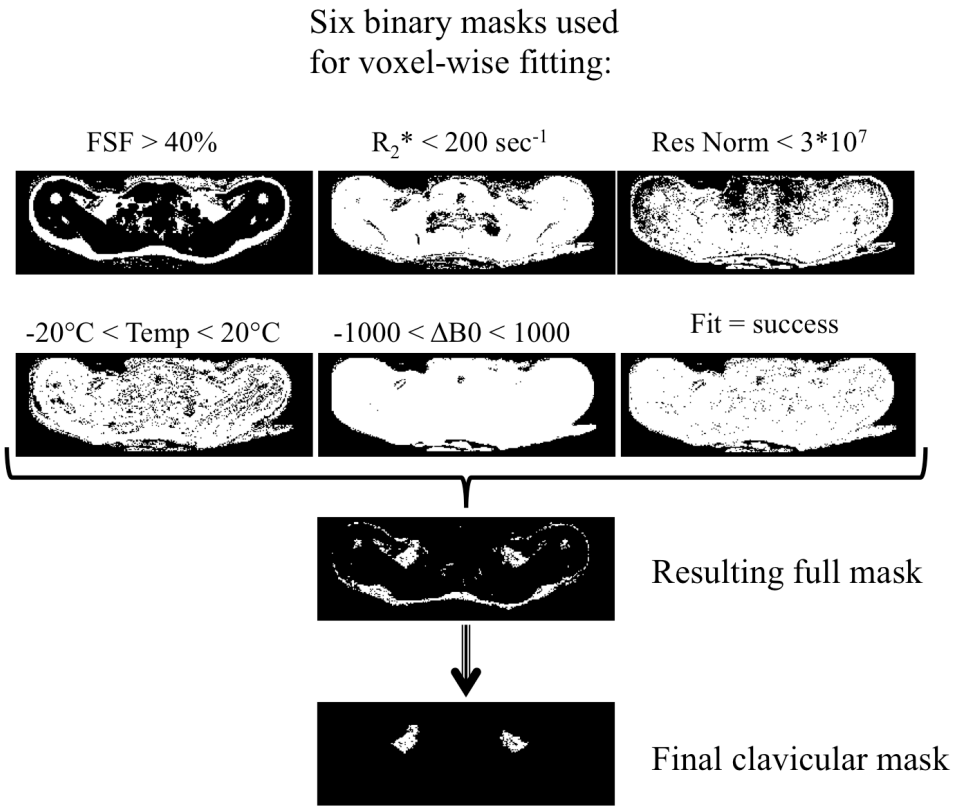

Figure 6.2-1. Automated FWMRI temperature-based mask creation.

6.2.2 Initial Results

Nine of the eleven subjects processed were PET-positive on their cold scan, and two were PET-negative. The results from two example subjects can be seen in Figure 6.2-2. Subject 01 was a PET-negative subject, showing no increased ^{18}F-FDG uptake during the cold (CA) scan (top row, left panel). Subject 02 was a PET-positive subject, showing characteristic increased ^{18}F-FDG uptake in the clavicular region during the CA scan (top row, right panel).

These results show that the FWMRI-derived temperature of the clavicular adipose tissue in the PET-negative subject (S01) is not significantly elevated from 37°C after exposure to either cold or warm temperatures. However, the FWMRI-derived temperature of the clavicular adipose tissue of the PET-positive subject (S02) is significantly elevated from body temperature after exposure to cold (3.73 ± 0.43°C). This is in agreement with the uptake of ^{18}F-FDG in the cold PET scans of S02 but not S01, as seen in the axial slices displayed in the second row of Figure 6.2-2. One hypothesis to explain these results is that the clavicular adipose tissue of S01 is not true BAT, and is potentially more white-like and therefore it did not activate and release heat when exposed to cold. In addition to the difference in temperatures between the two subjects, it is also interesting to note that there is also a difference in the clavicular fat-signal fraction (FSF) between the two subjects. The FSF of S01 (85.23 ± 0.87%) is higher than that of S02 (75.45 ± 0.59%), values seen in Table 6.2-1. This finding also supports the hypothesis that the clavicular adipose tissue of S01 is more white-like, since the fat content is higher.

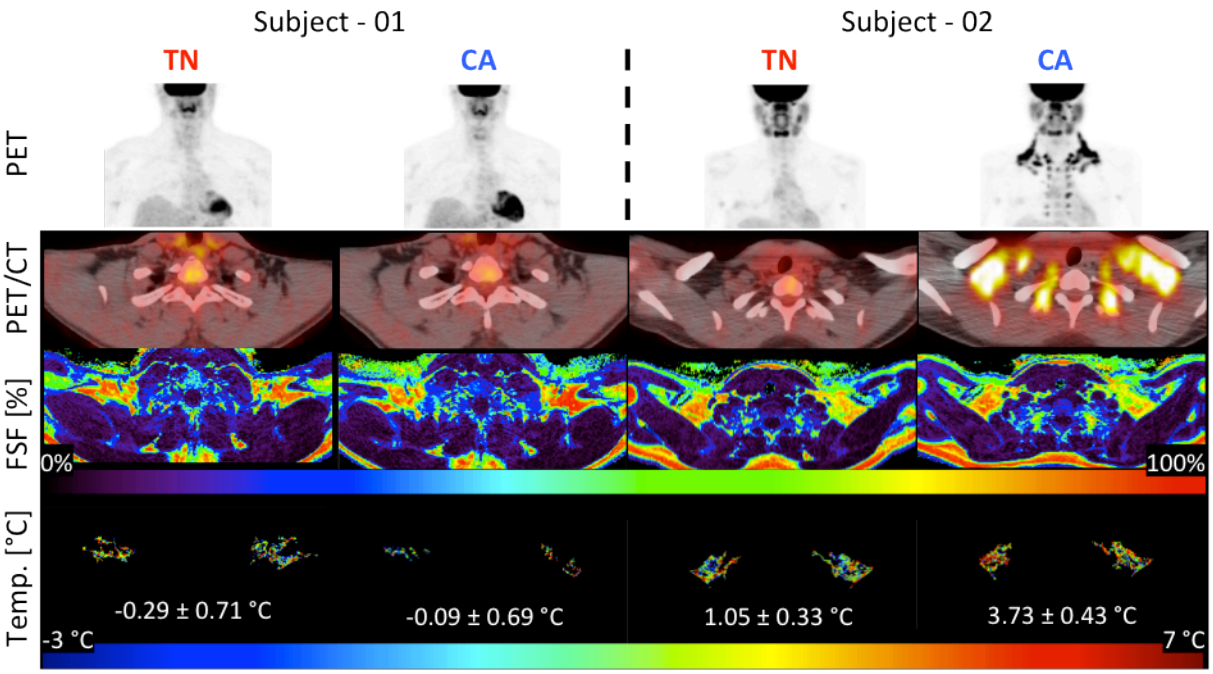

Figure 6.2-2. Temperature mapping results from both a PET-positive and PET-negative subject. Subject 01 is a cold PET-negative subject, and Subject 02 is a cold PET-positive subject, as seen in the top row. Row 3 shows an axial fat-signal fraction map, with the corresponding masked temperature maps shown in row 4, along with the mean ± 95% C.I temperature offsets (°C). The temperature reported is the offset from 37 °C (98.6 °F). TN = Thermoneutral scan, CA = Cold scan.

Results from each of the eleven subjects can be seen in Table 6.2-1. For the nine PET-positive subjects, the resulting temperature of the clavicular adipose tissue after exposure to warm temperatures was only slightly altered from normal body temperature. However, after exposure to cold temperatures the BAT activates and releases heat. This is reflected in the clavicular adipose temperatures elevated to values significantly greater than zero. Contrary to the PET-positive subjects, the two PET-negative subjects, S01 and S06, show only slightly altered temperatures in the clavicular adipose tissue after exposure to both cold and warm conditions. This indicates that their clavicular adipose tissue did not activate and release heat after exposure to cold temperatures. One possibility for this finding is that the adipose tissue present in the clavicular region is not BAT, but instead is a more white-like adipose tissue, and therefore it is

unable to activate and generate heat. A second possibility is that the tissue did activate and release heat, but did not activate to the same degree as the other subjects and therefore the heat released was not as high. This could be because an individualized cooling protocol was not used in this study and therefore S01 did not get cold enough to activate the BAT present.

Table 6.2-1. Results from the warm and cold FWMRI temperature maps.

	TN Scan Temp °C	CA Scan Temp °C	FSF %	CA PET
S 01	-0.29 ± 0.71	-0.09 ± 0.69	85.23 ± 0.87	–
S 02	1.05 ± 0.33	† 3.73 ± 0.43	75.45 ± 0.59	+
S 03	1.13 ± 0.51	† 3.89 ± 0.42	76.21 ± 0.86	+
S 04	-1.93 ± 0.53	† 2.58 ± 0.70	73.14 ± 1.12	+
S 05	0.85 ± 0.54	† 2.75 ± 0.68	76.67 ± 0.92	+
S 06	-0.63 ± 0.72	-0.69 ± 0.26	82.58 ± 0.39	–
S 07	-0.05 ± 0.50	* 1.27 ± 0.96	79.38 ± 0.91	+
S 08	0.50 ± 0.75	† 3.23 ± 0.42	78.48 ± 0.61	+
S 09	-0.72 ± 0.57	† 1.34 ± 0.34	68.41 ± 0.66	+
S 10	0.44 ± 0.96	* 1.07 ± 0.57	74.35 ± 0.89	+
S 11	-0.92 ± 0.94	† 1.64 ± 0.52	72.85 ± 0.72	+

Abbreviations: TN: thermoneutral, CA: Cold-activated. Temperature offset (from 37°C (98.6°F)) is reported as mean ± 95% C.I. in the clavicular ROI from both the TN and CA scans. The CA PET column indicates CA PET activity. '+': Increased ^{18}F-FDG uptake, '–': no ^{18}F-FDG uptake. Right-tail t-test of the CA data shows the mean is significantly greater than zero for all subjects, except the two PET-negative subjects, S01 and S06. (* $p < 0.01$, † $p <$ 1e-6).

6.2.3 Results and Discussion

Though other groups have pursued various FWMRI techniques,[225–227] this technique differs by using a multi-peak iterative method to create absolute thermometry maps without the need for comparative measurements. Additionally, although other FWMRI thermometry work has been performed on various targets,[227] as well as in animal BAT work,[228,229] to the best of our knowledge, this research presents the first report using MRI to determine the relative temperature change in BAT in adult humans.

Despite the small number of subjects, this study demonstrates the possibility to distinguish activated from non-activated BAT in adult humans using FWMRI-derived temperature mapping. The elevated temperature in activated BAT is detectable in FWMRI scans following cold exposure compared to scans following warm conditions. The results of this study demonstrate the potential of MRI to detect the activation state of brown adipose tissue.

CHAPTER 7

CONCLUSION AND FUTURE WORK

The work presented in this dissertation elucidates some of the imaging-derived properties of BAT in adult humans. Our data suggest that MRI FSF can be used to detect brown adipose regardless of activation status. Furthermore small but significant reductions in the FSF of BAT can be detected following activation. These findings support MRI as a viable option for studying BAT in adult humans. Additionally, this study extends previous MRI research to quantitatively measure differences in FSF and R_2* values in supraclavicular and subcutaneous adipose tissue depots.[148,210] To the best of our knowledge, this work represents the first study to obtain PET-CT and MRI scans of the same healthy adults after exposure to both thermoneutral and cold temperatures. Our findings support the use of these metrics to characterize and distinguish between BAT and WAT, and lay the foundation for future MRI analysis with the hope that someday MRI-based delineation of BAT can stand on its own. For example, an MRI profile of BAT could be compiled by combining the FSF and R_2* values here described with other previously described metrics such as T_1 (longitudinal relaxation),[211] triglyceride saturation,[212] and blood perfusion.[213]

Further work demonstrates that quantitative FWMRI derived FSF is significantly correlated with CT HU values in subcutaneous WAT. Additionally, the finding that subcutaneous adipose tissue HU values are inversely related to BMI is supported by the current literature,[230] serving to verify in part, our results. This shows that given the correlation of MRI FSF to CT HU, FSF could be used as an alternative to CT HU for assessing metabolic risk factors via the impact on adipose tissue quality. Additionally, spatial mapping of quantitative

adipose tissue properties, in addition to the assessment of adipose distribution and volume, could enhance understanding of health factors affected by adipose tissue.

The novel BAT segmentation method employed in this work minimizes the affect of rater subjectivity and boundary ambiguity. The rigorously defined MRI properties of BAT presented in this work lay the foundation for MRI-based quantitative imaging of BAT without the need for the ionizing radiation and the radioactive tracers required to obtain PET-CT images.

Future investigations can improve on the work presented in this dissertation. One of the downsides to this research protocol is the "one-size-fits-all" approach to both warming and cooling the subjects. Future work would benefit from using a more individualized approach to maximize non-shivering thermogenesis, and therefore maximize the BAT activation, for each subject. During the course of the research performed for this dissertation, new evidence came to light regarding the use of individualized cooling methods, as summarized in the recent publication by van der Lans et al.[17] Because people respond differently to cold stimuli, and because maximal BAT activation occurs as a form of non-shivering thermogenesis, the physiologic response to cold must be tracked. Instead of exposing all subjects to the same temperature, a temperature at which one subject might shiver violently while another experiences only mild cold, individualized cooling brings all the subjects to the same level of physiologic response. Exposing subjects to a degree of cold stimulus tailored to their physiologic response enables a more controlled response to the method of activation. Additionally, though the main focus is often on causing BAT to activate, it is also important to use an individualized approach to heating the subject to a thermoneutral condition to study inactive BAT.

As discussed in CHAPTER 4, accounting for temperature is important during MRI fat-water separation, as the tissue temperature affects the frequency of water and therefore the

chemical shift. Therefore it is important for future work to account for temperature in the fat-water separation model when calculating the tissue fat, water and R_2* values. Improving the signal model by accounting for temperature has the added benefit of resulting in a temperature map of the tissue. The temperature map can then be used as an additional characteristic of BAT, quantifying the difference in heat released by active and inactive BAT. The MR acquisition protocol can also be modified to determine if more echoes acquired with a smaller interleave – i.e. a smaller temporal resolution – would produce more accurate temperature maps. These protocol modifications can be tested in mixed fat-water phantoms under controlled heating and cooling to verify the temperature results. Other adjustments include increasing the SNR and spatial resolution of the scan.

Further improvements could also be made to the triglyceride mapping research presented in section 6.1. The model employed in this work to estimate mean triglyceride characteristics does not adequately model short-to-mid chain lengths, consistently overestimating chain length values. This can be modified through modeling using a Hill equation, typically applied to ligand-binding kinetics.[231] Hill fitting can also be applied to the triglyceride model used in this work, enabling a more accurate fitting of the short chain lengths. Furthermore, the MRI-based method for mapping triglyceride characteristics should be validated against gas liquid chromatography results of the same oil phantom. Though the oil phantom presented in section 6.1 was acquired and analyzed with the same protocol used for human research, the results of the oil phantom triglyceride characteristics were not verified using gas liquid chromatography.

Future research could also benefit from acquiring additional MR sequences designed to highlight salient features of BAT. For example BAT is a highly perfused tissue, so sequences that characterize properties such as perfusion and blood flow would be useful. One such method,

intravoxel incoherent motion (IVIM), is capable of measuring the microcirculation of blood in the capillary network.[232] Arterial spin labeling (ASL) also has the capability to measure flow per unit tissue.[233,234] Because BAT has rich capillary beds, these methods can measure increased perfusion due to increased blood flow. Another contrast agent, hyperpolarized xenon gas, is soluble in lipids. Because BAT is more highly perfused than WAT, the xenon signal in MRI is detected first in BAT.[124,229] Other MRI methods include hyperpolarized ^{13}C MRI scans, which use pre-polarized [1-^{13}C] pyruvate and are capable of detecting the byproducts of [1-^{13}C] pyruvate in BAT.[235] Intermolecular zero-quantum coherences (IZQC) measured with MRI is able to quantify the spatial correlation between the water and lipid spins. Doing so enables the measurement of the hydrolipidic ratio in BAT.[236,237] MRI quantification of the longitudinal relaxation (T_1) values for water and fat is another method that can be applied in future research. The T_1 values of water and fat are different, therefor by employing a hybrid fat-water imaging and T_1 mapping method it is possible to measure the T_1 of water and lipid protons separately.[141,238]

Beyond acquiring data, future work can also develop more advanced machine learning techniques for segmenting BAT based solely on MR measures. Developing a segmentation technique dependent only on MR-derived values would enable delineation of BAT depots without either rater subjectivity (hand-drawn regions of interest) or ionizing radiation (^{18}F-FDG PET-CT). Building on the preliminary work described in CHAPTER 5, potential avenues for machine learning based segmentation include algorithms such as k-means clustering, density-based spatial clustering of applications with noise (DBSCAN), and expectation–maximization (EM). An example three-dimensional plot of FSF vs. R_2* vs. Temperature is shown in Figure 7-1. These plots show the capability of these three metrics to delineate between WAT, bone, and

BAT voxels, three tissues that can have similar ranges of FSF values. However, the values in these three plots still overlap enough to where it is not entirely possible to distinguish between the three tissues. It is possible that adding other quantitative metrics such as T_1 or diffusion would provide enough additional information that a clearer distinction between the tissues is possible. This work on automated classification is important because reliable identification and spatial mapping methods that can distinguish BAT from other tissue distributions without the use of ionizing radiation will provide investigators with a powerful new tool with which to study BAT in both children and adults. This will in turn have a dramatic positive impact on clinical endocrinology and the pursuit of new avenues of obesity research.

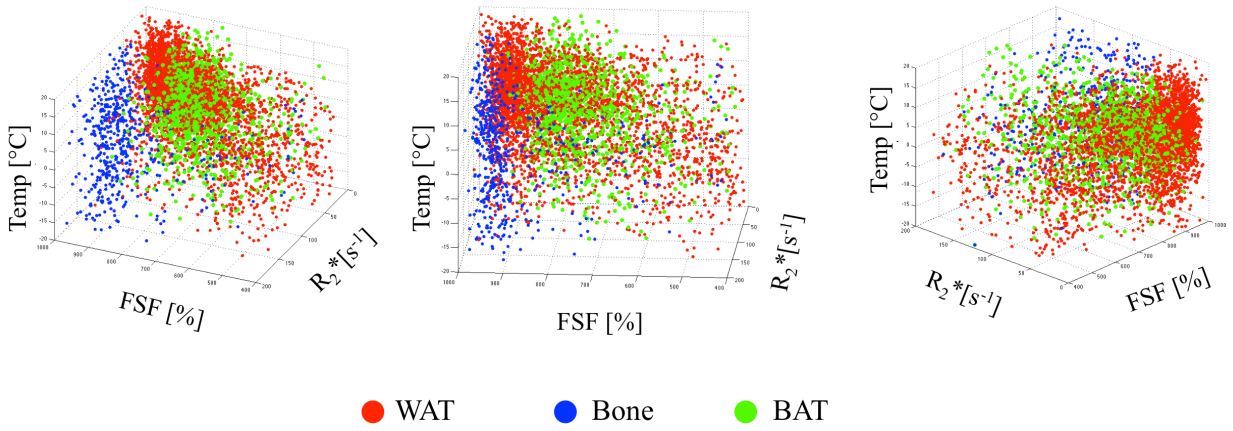

Figure 7-1. Three views of the same three-axis: FSF v. R_2* v. ΔT. These show some separation between the three tissues: red: white adipose tissue (WAT), blue: bone, and green: brown adipose tissue (BAT). By adding the additional quantitative metrics – i.e. T_1, and diffusion – it may be possible to more clearly distinguish between tissue types.

In addition to the previously described PET, CT and MRI methods, there exist several other techniques that can be employed for studying BAT, each offering distinct advantages to characterize the many properties of BAT. Furthermore there are advantages to using multiple imaging methods and/or tracers concurrently to understand the complex metabolic processes in

BAT. For example, using a combined PET-MR system PET allows for imaging the metabolic activity while MR measures the intracellular properties such as fat, water and perfusion. A mapping of several potential methods for characterizing BAT can be seen in Figure 7-2

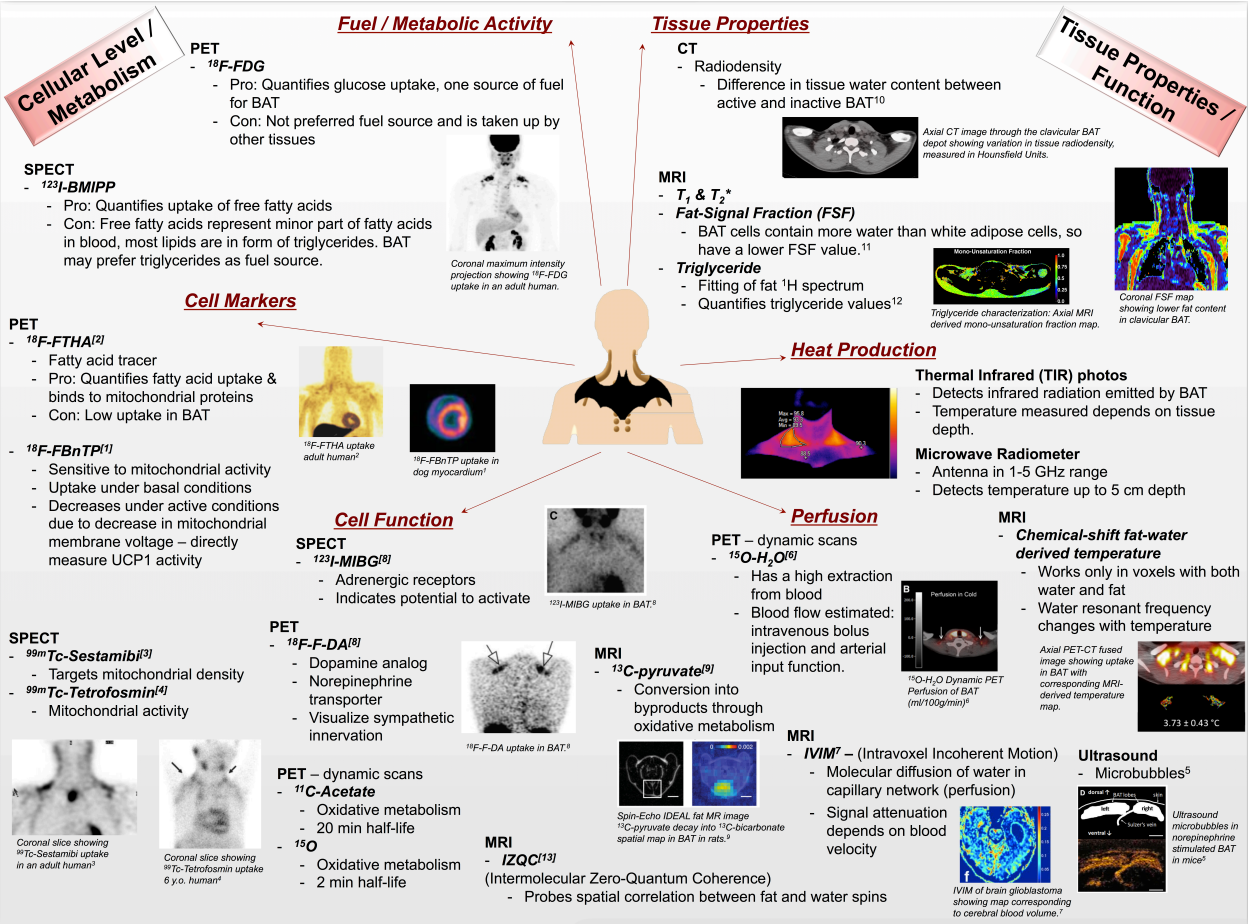

Figure 7-2. Mapping methods to characterize BAT.

As discussed previously, PET imaging depends on selective binding, or uptake and retention, of radiotracers in specific tissues. Arguably the most widely used modality to study BAT, PET imaging combined with various tracers can quantify many properties of BAT. The previously discussed radiotracer, ^{18}F-FDG, is used to visualize glucose uptake, but does not directly reflect mitochondrial activity and may underestimate metabolic activity of BAT. The

radiolabeled fatty acid tracer ^{18}F-fluoro-6-thia-heptadecanoic acid (^{18}F-FTHA) is taken up and bound to mitochondrial proteins, enabling the quantification of fatty acid uptake. Additionally, the tracer ^{18}F-fluorobenzyl triphenyl phosphonium (^{18}F-FBnTP) is sensitive to mitochondrial activity and is currently in pre-clinical trials.[239] It shows uptake under basal conditions and a decrease after cold stimulation. This is potentially due to the decrease in mitochondrial membrane voltage when UCP1 is active. If confirmed, this could be a method to directly measure UCP1 activity. The tracer 6-^{18}F-Fluorodopamine (^{18}F-F-DA) is a dopamine analog transported by the plasma membrane norepinephrine transporter.[240] Accumulation therefore allows visualization of sympathetic innervation, which is prevalent in BAT. In addition to static PET, dynamic PET studies can also be performed. It is possible to quantify oxidative metabolism using ^{11}C-Acetate under dynamic conditions.[132,241] Another tracer, oxygen-15 (^{15}O) also shows an increase in BAT after cold stimulation, but ^{11}C-Acetate and ^{15}O have half-lives of 20 and 2 minutes respectively, restricting research to facilities with in-house cyclotrons.[116,132,241]

Single-proton emission computed tomography (SPECT) is another imaging method that uses radiolabeled tracers for contrast. The fatty acid tracer ^{123}I-beta-methyl-p-iodophenylpentadecanoic acid (^{123}I-BMIPP) quantifies the uptake of free fatty acids,[242] while Technetium-99m (^{99}mTc) ^{99m}Tc-sestamibi and ^{99m}Tc-tetrofosmin measure mitochondrial activity.[243,244] No studies of human BAT have been conducted yet using these tracers, but animal work shows higher uptake under basal conditions compared to FDG; however, uptake does not increase greatly after exposure to cold.[241] This is because sestamibi targets mitochondrial density, which does not change in the short-term. Therefore the slight increase in sestamibi is potentially due to the increase in blood flow to active BAT, which would deliver a greater volume of the tracer to the tissue in a given time. Another tracer, ^{123}I- metaiodobenzylguanidine

(^{123}I-MIBG), is sensitive to adrenergic receptors in BAT, and could therefore be a good indication of the potential for BAT to be activated.[240]

Table 7-1. Imaging modalities for characterizing BAT

	Fuel Source	Cell Markers	Cell Function	Perfusion	Temperature	Tissue
PET (static)	^{18}F-FDG	^{18}F-FTHA & ^{18}F-FBnTP	^{18}F-F-DA			
PET (dynamic)			^{11}C-Acetate & ^{15}O	$C^{15}O$ & $H_2{}^{15}O$		
SPECT	^{123}I-BMIPP	^{99m}Tc-sestamibi & ^{99m}Tc-tetrofosmin	^{123}I-MIBG			
CT						Radiodensity
Thermal					IR & microwave	
Ultrasound				Microbubbles		
MRI			^{13}C pyruvate & IZQC	ASL & IVIM	Chemical-shift	Triglyceride, FSF, T_1 & T_2*

Each modality is listed with a corresponding radiotracer or method used to quantify BAT properties at either the cell or tissue level.

Apart from MRI, ultrasound is another nonionizing imaging modality that can be used to image BAT. Imaging using contrast ultrasound with microbubbles has been successful in quantifying the blood flow in BAT.[133,245] By measuring the signal intensity of continuously infused microbubbles, blood flow in BAT can be measured. Additionally, although currently unused in the study of BAT, it is possible that elastography could detect differences between BAT and surrounding tissue due to differences in tissue stiffness. Transient elastography uses pulse-echo ultrasound signals to measure tissue stiffness. Tissue stiffness is partly a result of the tissue elastin and collagen content. Under small strains or deformations, elastin gives stiffness to the tissue, while large tissue deformations result in collagen stretching in the direction of deformation. Typically fibrous tissue remains deformed for longer than adipose or muscle tissue, and adipose is easier to deform.[246] Elastography has been successfully applied in distinguish

between fibrotic and fatty tissues in breast tumor imaging[247] and in characterizing subcutaneous WAT and livers of obese adults.[248,249] Therefore, it could be possible to characterize BAT using ultrasound elastography.

In addition to using MRI-derived temperature mapping of BAT, there are two main additional methods to detect the heat released by activated BAT: thermal infrared (TIR) photos and microwave radiometers. TIR cameras detect infrared radiation from the tissue, and do not require visible illumination, as seen in Figure 7-3. This provides a fast, easy, completely noninvasive method for measuring the heat released by an object, however there are a few drawbacks. Because the temperature is measured at the surface of the skin, it is an indirect measure of the temperature of BAT. The depth of the BAT depot, and what tissues exist between the BAT and skin also affects the temperature recorded at the skin surface. Therefore TIR temperature measures may be more unreliable in subjects with a higher BMI, and therefore thicker layer of muscle or fat below the skin.

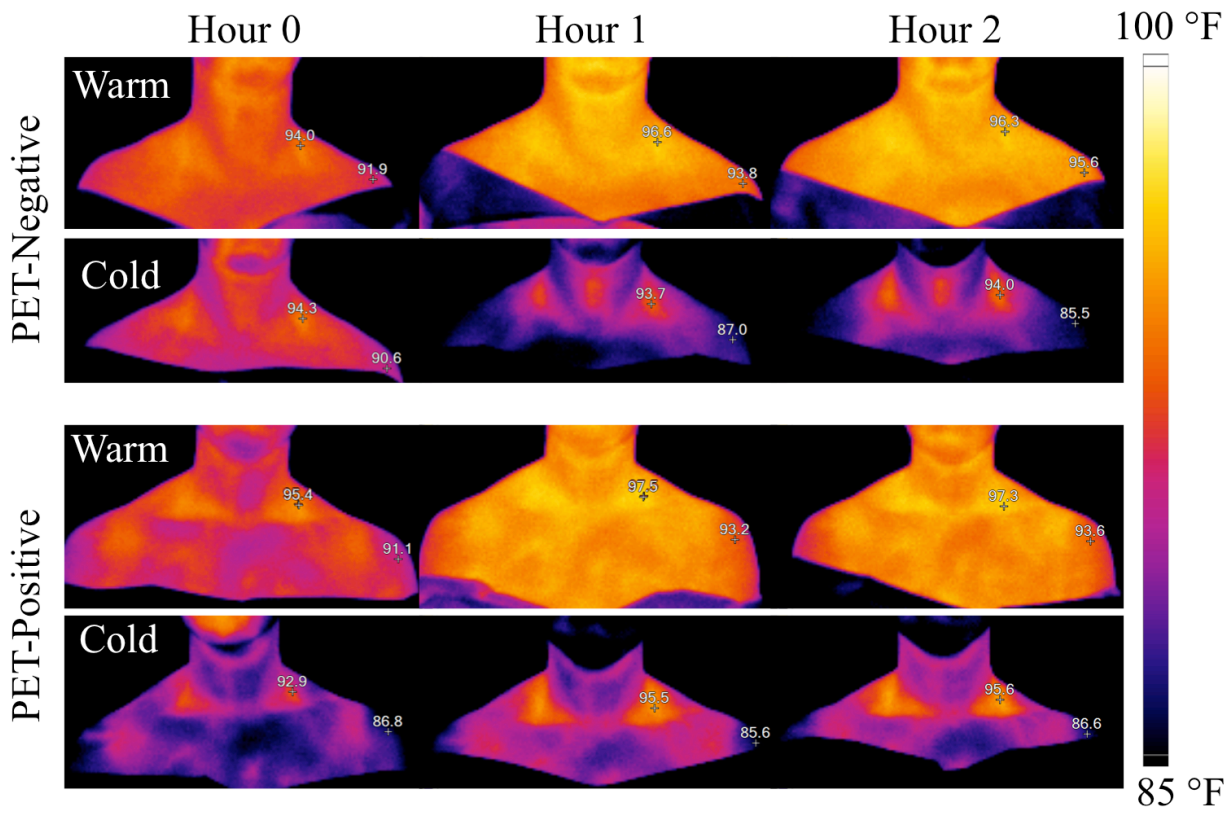

Figure 7-3. Thermal Infrared (TIR) photos of two subjects: one PET-Negative (top panel), and one PET-Positive (bottom panel). The images show skin temperature at three time-points: baseline (hour 0), and after 1 and 2 hours in the temperature-controlled room. After 2 hours of exposure to cold, the clavicular region on the PET-Negative subject is not as warm as that of the PET-positive subject, potentially indicating that the clavicular BAT was not active functioning at the same thermogenic capacity.

The second method, microwave radiometers, are passive devices that receive thermal emissions from tissue using an antenna in the 1-5 GHz range.[250,251] They are capable of detecting small changes in temperature at a depth of up to 5 cm, which is within the range of the depth of clavicular BAT. One potential advantage of microwave radiometers is that they are relatively small portable devices. The radiometers' small size could enable it to be used for continuous monitoring, as is done with other portable physiological monitors.

In conclusion, the present study extends the application of MRI to quantifying the MRI FSF and R_2* properties of BAT in adults. Building on these results with additional MRI-derived properties such as temperature, diffusion, perfusion, and T_1, MRI will be able to distinguish BAT without human subjectivity, even if the tissue is not active. Because some subjects that are PET-negative do have BAT, it is important to develop a technique for detecting BAT that does not rely solely on the rate of glucose metabolism. Additionally, the ability to distinguish BAT without ionizing radiation would enable BAT to be studied in larger cohorts, in longitudinal studies, and in difficult populations such as pediatrics, which could further our understanding of the role BAT plays in humans.

REFERENCES

1. Cinti S. The adipose organ. *Prostaglandins Leukot Essent Fatty Acids*. 2005;73(1):9–15. doi:10.1016/j.plefa.2005.04.010.
2. Porter C, Malagaris I, Sidossis LS. Is the heat surrounding adipose tissue mitochondria warranted? *Curr Opin Clin Nutr Metab Care*. 2014;(409). doi:10.1097/MCO.0000000000000102.
3. Tsiloulis T, Watt MJ. Exercise and the Regulation of Adipose Tissue Metabolism. *Prog Mol Biol Transl Sci*. 2015;135:175–201. doi:10.1016/bs.pmbts.2015.06.016.
4. Hull D. Heat production in adipose tissue. *Proc R Soc Med*. 1966;59(12):1278–80.
5. Smith RE, Horwitz B a. Brown fat and thermogenesis. *Physiol Rev*. 1969;49(2):330–425.
6. Cannon B, Nedergaard J. Brown adipose tissue: function and physiological significance. *Physiol Rev*. 2004;84(1):277–359. doi:10.1152/physrev.00015.2003.
7. Norheim F, Langleite TM, Hjorth M, et al. The effects of acute and chronic exercise on PGC-1α, irisin and browning of subcutaneous adipose tissue in humans. *FEBS J*. 2014;281(3):739–749. doi:10.1111/febs.12619.
8. Lee P, Linderman JD, Smith S, et al. Irisin and FGF21 are cold-induced endocrine activators of brown fat function in humans. *Cell Metab*. 2014;19(2):302–309. doi:10.1016/j.cmet.2013.12.017.
9. Wang G-X, Zhao X-Y, Meng Z-X, et al. The brown fat-enriched secreted factor Nrg4 preserves metabolic homeostasis through attenuation of hepatic lipogenesis. *Nat Med*. 2014;20(12):1436–43. doi:10.1038/nm.3713.
10. Chondronikola M, Volpi E, Borsheim E, et al. Brown Adipose Tissue Improves Whole-Body Glucose Homeostasis and Insulin Sensitivity in Humans. *Diabetes*. 2014;63(12):4089–4099. doi:10.2337/db14-0746.
11. Lee P, Smith S, Linderman J, et al. Temperature-acclimated brown adipose tissue modulates insulin sensitivity in humans. *Diabetes*. 2014;177(11):1–59. doi:10.2337/db14-0513.
12. Saito M, Okamatsu-Ogura Y, Matsushita M, et al. High incidence of metabolically active brown adipose tissue in healthy adult humans: effects of cold exposure and adiposity. *Diabetes*. 2009;58(7):1526–31. doi:10.2337/db09-0530.
13. Virtanen KA, Lidell ME, Orava J, et al. Functional brown adipose tissue in healthy adults. *N Engl J Med*. 2009;360(15):1518–25. doi:10.1056/NEJMoa0808949.
14. van Marken Lichtenbelt WD, Vanhommerig JW, Smulders NM, et al. Cold-activated brown adipose tissue in healthy men. *N Engl J Med*. 2009;360(15):1500–8. doi:10.1056/NEJMoa0808718.
15. Bartelt A, Bruns OT, Reimer R, et al. Brown adipose tissue activity controls triglyceride clearance. *Nat Med*. 2011;17(2):200–5. doi:10.1038/nm.2297.

16. Ouellet V, Labbé SM, Blondin DP, et al. Brown adipose tissue oxidative metabolism contributes to energy expenditure during acute cold exposure in humans. *J Clin Invest*. 2012;122(2):545–52. doi:10.1172/JCI60433.

17. van der Lans A a JJ, Wierts R, Vosselman MJ, Schrauwen P, Brans B, van Marken Lichtenbelt WD. Cold-activated brown adipose tissue in human adults: methodological issues. *AJP Regul Integr Comp Physiol*. 2014;307(2):R103–R113. doi:10.1152/ajpregu.00021.2014.

18. Lowry DW, Tomiyama a J. Air displacement plethysmography versus dual-energy x-ray absorptiometry in underweight, normal-weight, and overweight/obese individuals. *PLoS One*. 2015;10(1):e0115086. doi:10.1371/journal.pone.0115086.

19. Virtanen KA, Nuutila P. Brown adipose tissue in humans. *Curr Opin Lipidol*. 2011;22(1):49–54. doi:10.1097/MOL.0b013e3283425243.

20. Zancanaro C, Carnielli VP, Moretti C, Benati D, Gamba P. An ultrastructural study of brown adipose tissue in pre-term human new-borns. *Tissue Cell*. 1995;27(3):339–348. doi:10.1016/S0040-8166(95)80055-7.

21. Avram MM, Avram AS, James WD. Subcutaneous fat in normal and diseased states: 1. Introduction. *J Am Acad Dermatol*. 2005;53(4):663–70. doi:10.1016/j.jaad.2005.05.014.

22. Avram AS, Avram MM, James WD. Subcutaneous fat in normal and diseased states: 2. Anatomy and physiology of white and brown adipose tissue. *J Am Acad Dermatol*. 2005;53(4):671–83. doi:10.1016/j.jaad.2005.05.015.

23. Heaton JM. The distribution of brown adipose tissue in the human. *J Anat*. 1972;112(Pt 1):35–9.

24. Rylander E, Pribylová H, Lind J. A thermographic study of infants exposed to cold. *Acta Paediatr Scand*. 1972;61(1):42–8.

25. Merklin RJ. Growth and distribution of human fetal brown fat. *Anat Rec*. 1974;178(3):637–45. doi:10.1002/ar.1091780311.

26. Rousset S, Alves-Guerra M-C, Mozo J, et al. The biology of mitochondrial uncoupling proteins. *Diabetes*. 2004;53 Suppl 1:S130–5. doi:10.2337/diabetes.53.2007.S130.

27. Seale P, Bjork B, Yang W, et al. PRDM16 controls a brown fat/skeletal muscle switch. *Nature*. 2008;454(7207):961–967. doi:10.1038/nature07182.

28. Sanchez-Gurmaches J, Guertin D a. Adipocyte lineages: Tracing back the origins of fat. *Biochim Biophys Acta - Mol Basis Dis*. 2014;1842(3):340–351. doi:10.1016/j.bbadis.2013.05.027.

29. Ishibashi J, Seale P. Medicine. Beige can be slimming. *Science*. 2010;328(5982):1113–4. doi:10.1126/science.1190816.

30. Waldén TB, Hansen IR, Timmons JA, Cannon B, Nedergaard J. Recruited vs. nonrecruited molecular signatures of brown, “brite,” and white adipose tissues. *Am J Physiol Endocrinol Metab*. 2012;302(1):E19–31. doi:10.1152/ajpendo.00249.2011.

31. Cinti S. Between brown and white: novel aspects of adipocyte differentiation. *Ann Med*.

2011;43(2):104–15. doi:10.3109/07853890.2010.535557.

32. Nedergaard J, Bengtsson T, Cannon B. Three years with adult human brown adipose tissue. *Ann N Y Acad Sci*. 2010;1212(1):E20–36. doi:10.1111/j.1749-6632.2010.05905.x.

33. Wu J, Spiegelman BM. Irisin ERKs the Fat. *Diabetes*. 2014;63(2):381–3. doi:10.2337/db13-1586.

34. Lo KA, Sun L. Turning WAT into BAT: a review on regulators controlling the browning of white adipocytes. *Biosci Rep*. 2013;33(5):711–719. doi:10.1042/BSR20130046.

35. Medina-Gómez G. Mitochondria and endocrine function of adipose tissue. *Best Pract Res Clin Endocrinol Metab*. 2012;26(6):791–804. doi:10.1016/j.beem.2012.06.002.

36. Wronska a., Kmiec Z. Structural and biochemical characteristics of various white adipose tissue depots. *Acta Physiol*. 2012;205(2):194–208. doi:10.1111/j.1748-1716.2012.02409.x.

37. Lee YH, Mottillo EP, Granneman JG. Adipose tissue plasticity from WAT to BAT and in between. *Biochim Biophys Acta - Mol Basis Dis*. 2014;1842(3):358–369. doi:10.1016/j.bbadis.2013.05.011.

38. Harms M, Seale P. Brown and beige fat: development, function and therapeutic potential. *Nat Med*. 2013;19(10):1252–63. doi:10.1038/nm.3361.

39. Peirce V, Carobbio S, Vidal-Puig A. The different shades of fat. *Nature*. 2014;510(7503):76–83. doi:10.1038/nature13477.

40. Pfeifer A, Hoffmann LS. Brown, Beige, and White: The New Color Code of Fat and Its Pharmacological Implications. *Annu Rev Pharmacol Toxicol*. 2014;(August 2014):1–21. doi:10.1146/annurev-pharmtox-010814-124346.

41. Pisani DF. Differentiation of human adipose-derived stem cells into “brite” (brown-in-white) adipocytes. *Front Endocrinol (Lausanne)*. 2011;2. doi:10.3389/fendo.2011.00087.

42. Ussar S, Lee KY, Dankel SN, et al. ASC-1, PAT2, and P2RX5 are cell surface markers for white, beige, and brown adipocytes. *Sci Transl Med*. 2014;6(247):247ra103–247ra103. doi:10.1126/scitranslmed.3008490.

43. Obregon M-J. Adipose tissues and thyroid hormones. *Front Physiol*. 2014;5(December):479. doi:10.3389/fphys.2014.00479.

44. Suter ER. The fine structure of brown adipose tissue. *J Ultrastruct Res*. 1969;26(3):216–41. doi:10.1016/S0022-5320(69)80003-1.

45. Roberts J, Hock R, Smith R. Effects of altitude on brown fat and metabolism of the deer mouse, Peromyscus. *Fed Proc*. 1969;28(3).

46. Kawate R, Talan MI, Engel BT. Sympathetic nervous activity to brown adipose tissue increases in cold-tolerant mice. *Physiol Behav*. 1994;55(5):921–5.

47. Davy KP, Orr JS. Sympathetic nervous system behavior in human obesity. *Neurosci Biobehav Rev*. 2009;33(2):116–24. doi:10.1016/j.neubiorev.2008.05.024.

48. Collins S, Surwit RS. The beta-adrenergic receptors and the control of adipose tissue

metabolism and thermogenesis. *Recent Prog Horm Res*. 2001;56:309–28.

49. Flatmark T, Ruzicka FJ, Beinert H. The pattern of iron sulfur centers in Brown adipose tissue mitochondria: preponderance of ETF dehydrogenase and invariance with the thermogenic state. *FEBS Lett*. 1976;63(1):51–55. doi:10.1016/0014-5793(76)80192-5.

50. Lidell ME, Betz MJ, Enerbäck S. Brown adipose tissue and its therapeutic potential. *J Intern Med*. 2014. doi:10.1111/joim.12255.

51. Roman S, Agil A, Peran M, et al. Brown adipose tissue and novel therapeutic approaches to treat metabolic disorders. *Transl Res*. 2015;165(4):464–479. doi:10.1016/j.trsl.2014.11.002.

52. Matthias a., Ohlson KBE, Fredriksson JM, Jacobsson a., Nedergaard J, Cannon B. Thermogenic responses in brown fat cells are fully UCP1-dependent. UCP2 or UCP3 do not substitute for UCP1 in adrenergically or fatty acid-induced thermogenesis. *J Biol Chem*. 2000;275(33):25073–25081. doi:10.1074/jbc.M000547200.

53. Tatsumi M, Engles JM, Ishimori T, Nicely O, Cohade C, Wahl RL. Intense (18)F-FDG uptake in brown fat can be reduced pharmacologically. *J Nucl Med*. 2004;45(7):1189–1193.

54. Gelfand MJ, O'hara SM, Curtwright LA, Maclean JR. Pre-medication to block [(18)F]FDG uptake in the brown adipose tissue of pediatric and adolescent patients. *Pediatr Radiol*. 2005;35(10):984–90. doi:10.1007/s00247-005-1505-8.

55. Chaffee RR, Allen JR, Arine RM, Fineg a J, Rochelle RH, Rosander J. Studies on thermogenesis in brown adipose tissue in temperature-acclimated Macaca mulatta. *Comp Biochem Physiol A Comp Physiol*. 1975;50(2):303–306. doi:10.1016/0300-9629(75)90017-1.

56. Chaffee RR, Allen JR. Effects of ambient temperature on the resting metabolic rate of cold- and heat-acclimated Macaca mulatta. *Comp Biochem Physiol A Comp Physiol*. 1973;44(4):1215–1225. doi:10.1016/0300-9629(73)90260-0.

57. Génin F, Nibbelink M, Galand M, Perret M, Ambid L. Brown fat and nonshivering thermogenesis in the gray mouse lemur (Microcebus murinus). *Am J Physiol Regul Integr Comp Physiol*. 2003;284(3):R811–R818. doi:10.1152/ajpregu.00525.2002.

58. Blondin DP, Labbé SM, Tingelstad HC, et al. Increased brown adipose tissue oxidative capacity in cold-acclimated humans. *J Clin Endocrinol Metab*. 2014;99(3):438–446. doi:10.1210/jc.2013-3901.

59. Young P, Arch JR, Ashwell M. Brown adipose tissue in the parametrial fat pad of the mouse. *FEBS Lett*. 1984;167(1):10–4. doi:10.1016/0014-5793(84)80822-4.

60. Cousin B, Cinti S, Morroni M, et al. Occurrence of brown adipocytes in rat white adipose tissue: molecular and morphological characterization. *J Cell Sci*. 1992;103 (Pt 4):931–42.

61. Sidossis LS, Porter C, Saraf MK, et al. Browning of Subcutaneous White Adipose Tissue in Humans after Severe Adrenergic Stress. *Cell Metab*. 2015;22(2):219–27. doi:10.1016/j.cmet.2015.06.022.

62. Yoneshiro T, Aita S, Matsushita M, et al. Recruited brown adipose tissue as an antiobesity agent in humans. *J Clin Invest*. 2013;123(8):3404–8. doi:10.1172/JCI67803.

63. van der Lans AAJJ, Hoeks J, Brans B, et al. Cold acclimation recruits human brown fat and increases nonshivering thermogenesis. *J Clin Invest*. 2013;123(8):3395–403. doi:10.1172/JCI68993.

64. Boström P, Wu J, Jedrychowski MP, et al. A PGC1-α-dependent myokine that drives brown-fat-like development of white fat and thermogenesis. *Nature*. 2012;481(7382):463–8. doi:10.1038/nature10777.

65. Fisher FM, Kleiner S, Douris N, et al. FGF21 regulates PGC-1α and browning of white adipose tissues in adaptive thermogenesis. *Genes Dev*. 2012;26(3):271–81. doi:10.1101/gad.177857.111.

66. Emanuelli B, Vienberg SG, Smyth G, et al. Interplay between FGF21 and insulin action in the liver regulates metabolism. *J Clin Invest*. 2014;124(2):515–27. doi:10.1172/JCI67353.

67. Trayhurn P, Beattie JH. Physiological role of adipose tissue: white adipose tissue as an endocrine and secretory organ. *Proc Nutr Soc*. 2001;60(3):329–39. doi:10.1079/PNS200194.

68. Giordano A, Smorlesi A, Frontini A, Barbatelli G, Cinti S. MECHANISMS IN ENDOCRINOLOGY: White, brown and pink adipocytes: the extraordinary plasticity of the adipose organ. *Eur J Endocrinol*. 2014;170(5):R159–R171. doi:10.1530/EJE-13-0945.

69. Elmquist JK, Elias CF, Saper CB. From lesions to leptin: hypothalamic control of food intake and body weight. *Neuron*. 1999;22(2):221–32. doi:S0896-6273(00)81084-3 [pii].

70. Elias CF, Aschkenasi C, Lee C, et al. Leptin differentially regulates NPY and POMC neurons projecting to the lateral hypothalamic area. *Neuron*. 1999;23(4):775–86. doi:10.1016/S0896-6273(01)80035-0.

71. Petersen KF, Oral EA, Dufour S, et al. Leptin reverses insulin resistance and hepatic steatosis in patients with severe lipodystrophy. *J Clin Invest*. 2002;109(10):1345–50. doi:10.1172/JCI15001.

72. Díez JJ, Iglesias P. The role of the novel adipocyte-derived hormone adiponectin in human disease. *Eur J Endocrinol*. 2003;148(3):293–300. doi:10.1530/eje.0.1480293.

73. Gustafson B, Hammarstedt A, Andersson CX, Smith U. Inflamed adipose tissue: a culprit underlying the metabolic syndrome and atherosclerosis. *Arterioscler Thromb Vasc Biol*. 2007;27(11):2276–83. doi:10.1161/ATVBAHA.107.147835.

74. Lee P, Brychta RJ, Linderman J, Smith S, Chen KY, Celi FS. Mild cold exposure modulates fibroblast growth factor 21 (FGF21) diurnal rhythm in humans: Relationship between FGF21 levels, lipolysis, and cold-induced thermogenesis. *J Clin Endocrinol Metab*. 2013;98(1):E98–E102. doi:10.1210/jc.2012-3107.

75. Villarroya J, Cereijo R, Villarroya F. An endocrine role for brown adipose tissue? *Am J Physiol Endocrinol Metab*. 2013;305(5):E567–72. doi:10.1152/ajpendo.00250.2013.

76. Sarruf D a, Thaler JP, Morton GJ, et al. Fibroblast growth factor 21 action in the brain

increases energy expenditure and insulin sensitivity in obese rats. *Diabetes*. 2010;59(7):1817–24. doi:10.2337/db09-1878.

77. Wu J, Boström P, Sparks LM, et al. Beige adipocytes are a distinct type of thermogenic fat cell in mouse and human. *Cell*. 2012;150(2):366–76. doi:10.1016/j.cell.2012.05.016.

78. Sharp LZ, Shinoda K, Ohno H, et al. Human BAT possesses molecular signatures that resemble beige/brite cells. *PLoS One*. 2012;7(11):e49452. doi:10.1371/journal.pone.0049452.

79. Lee P, Werner CD, Kebebew E, Celi FS. Functional thermogenic beige adipogenesis is inducible in human neck fat. *Int J Obes (Lond)*. 2014;38(2):170–6. doi:10.1038/ijo.2013.82.

80. Burýsek L, Houstek J. beta-Adrenergic stimulation of interleukin-1alpha and interleukin-6 expression in mouse brown adipocytes. *FEBS Lett*. 1997;411(1):83–6. doi:10.1016/S0014-5793(97)00671-6.

81. Stanford KI, Middelbeek RJW, Townsend KL, et al. Brown adipose tissue regulates glucose homeostasis and insulin sensitivity. *J Clin Invest*. 2013;123(1):215–23. doi:10.1172/JCI62308.

82. Poekes L, Lanthier N, Leclercq IA. Brown adipose tissue: a potential target in the fight against obesity and the metabolic syndrome. *Clin Sci (Lond)*. 2015;129(11):933–49. doi:10.1042/CS20150339.

83. Stephens M, Ludgate M, Rees DA. Brown fat and obesity: the next big thing? *Clin Endocrinol (Oxf)*. 2011;74(6):661–70. doi:10.1111/j.1365-2265.2011.04018.x.

84. Birerdinc A, Jarrar M, Stotish T, Randhawa M, Baranova A. Manipulating molecular switches in brown adipocytes and their precursors: A therapeutic potential. *Prog Lipid Res*. 2013;52(1):51–61. doi:10.1016/j.plipres.2012.08.001.

85. Timmons J a., Baar K, Davidsen PK, Atherton PJ. Is irisin a human exercise gene? *Nature*. 2012;488(7413):E9–E10. doi:10.1038/nature11364.

86. Hecksteden A, Wegmann M, Steffen A, et al. Irisin and exercise training in humans - results from a randomized controlled training trial. *BMC Med*. 2013;11(1):235. doi:10.1186/1741-7015-11-235.

87. Albrecht E, Norheim F, Thiede B, et al. Irisin - a myth rather than an exercise-inducible myokine. *Sci Rep*. 2015;5:8889. doi:10.1038/srep08889.

88. Kraemer RR, Shockett P, Webb ND, Shah U, Castracane VD. A transient elevated irisin blood concentration in response to prolonged, moderate aerobic exercise in young men and women. *Horm Metab Res*. 2014;46(2):150–4. doi:10.1055/s-0033-1355381.

89. Aydin S, Aydin S, Kuloglu T, et al. Alterations of irisin concentrations in saliva and serum of obese and normal-weight subjects, before and after 45 min of a Turkish bath or running. *Peptides*. 2013;50:13–8. doi:10.1016/j.peptides.2013.09.011.

90. Jedrychowski MP, Wrann CD, Paulo JA, et al. Detection and Quantitation of Circulating Human Irisin by Tandem Mass Spectrometry. *Cell Metab*. 2015;22(4):734–40.

doi:10.1016/j.cmet.2015.08.001.

91. Hofmann T, Elbelt U, Stengel A. Irisin as a muscle-derived hormone stimulating thermogenesis--a critical update. *Peptides*. 2014;54:89–100. doi:10.1016/j.peptides.2014.01.016.

92. Gessner C. *Conradi Gesneri medici Tigurini Historiae animalium lib. I de Quadrupedibus uiuiparis*. Zurich, Switzerland: Froschauer; 1551.

93. Velsch GH. No Title. *Ephemer Acad Nat Cur Ann*. 1670;1(160):298.

94. Jacobson L. Ueber die Thymus der Winterschläfer. *Dtsch Arch für die Physiol*. 1817;3:151–152.

95. RASMUSSEN AT. THE GLANDULAR STATUS OF BROWN MULTILOCULAR ADIPOSE TISSUE. *Endocrinology*. 1922;6(6):760–770. doi:10.1210/endo-6-6-760.

96. Bonnot E. The Interscapular Gland. *J Anat Physiol*. 1908;1(3):43–58.

97. Inglis K. The So-called Interscapular Gland and Tumours Arising Therein. *J Anat*. 1927;61(Pt 4):452–466.11.

98. SIMON HE. Posterior cervical tumor of brown fat in man; its relationship to the interscapular gland of hibernating animals. *Am J Surg*. 1950;80(1):127–30.

99. Tanuma Y, Tamamoto M, Ito T, Yokochi C. The occurrence of brown adipose tissue in perirenal fat in Japanese. *Arch Histol Jpn*. 1975;38(1):43–70.

100. Minor JG, Folk GE, Dryer RL. Changes in triglyceride composition of white and brown adipose tissues during developing cold acclimation of the golden hamster Mesocricetus auratus. *Comp Biochem Physiol B*. 1973;46(2):375–85.

101. Nedergaard J, Cannon B. Preferential utilization of brown adipose tissue lipids during arousal from hibernation in hamsters. *Am J Physiol*. 1984;247(3 Pt 2):R506–12.

102. Som P, Atkins HL, Bandoypadhyay D, et al. A fluorinated glucose analog, 2-fluoro-2-deoxy-D-glucose (F-18): nontoxic tracer for rapid tumor detection. *J Nucl Med*. 1980;21(7):670–675. doi:10.1097/00004728-198012000-00045.

103. Engel H, Steinert H, Buck A, Berthold T, Huch Böni R a, von Schulthess GK. Whole-body PET: physiological and artifactual fluorodeoxyglucose accumulations. *J Nucl Med*. 1996;37(3):441–446.

104. Barrington SF, Maisey MN. Skeletal muscle uptake of fluorine-18-FDG: effect of oral diazepam. *J Nucl Med*. 1996;37(7):1127–1129.

105. Townsend DW. Combined PET / CT : the historical perspective. *Semin Ultrasound, CT, MRI*. 2009;29(4):232–235. doi:10.1053/j.sult.2008.05.006.Combined.

106. Hany TF, Gharehpapagh E, Kamel EM, Buck A, Himms-Hagen J, Von Schulthess GK. Brown adipose tissue: A factor to consider in symmetrical tracer uptake in the neck and upper chest region. *Eur J Nucl Med*. 2002;29(10):1393–1398. doi:10.1007/s00259-002-0902-6.

107. Cohade C, Osman M, Pannu HK, Wahl RL. Uptake in supraclavicular area fat ("USA-

Fat"): description on 18F-FDG PET/CT. *J Nucl Med*. 2003;44(2):170–6.

108. Yeung HWD, Grewal RK, Gonen M, Schöder H, Larson SM. Patterns of (18)F-FDG uptake in adipose tissue and muscle: a potential source of false-positives for PET. *J Nucl Med*. 2003;44(11):1789–96.

109. Bar-Shalom R, Gaitini D, Keidar Z, Israel O. Non-malignant FDG uptake in infradiaphragmatic adipose tissue: a new site of physiological tracer biodistribution characterised by PET/CT. *Eur J Nucl Med Mol Imaging*. 2004;31(8):1105–1113. doi:10.1016/S1040-1741(08)70025-3.

110. Lee P, Zhao JT, Swarbrick MM, et al. High prevalence of brown adipose tissue in adult humans. *J Clin Endocrinol Metab*. 2011;96(8):2450–2455. doi:10.1210/jc.2011-0487.

111. Lee P, Swarbrick MM, Zhao JT, Ho KKY. Inducible brown adipogenesis of supraclavicular fat in adult humans. *Endocrinology*. 2011;152(10):3597–602. doi:10.1210/en.2011-1349.

112. Lidell ME, Betz MJ, Leinhard OD, et al. Evidence for two types of brown adipose tissue in humans. *Nat Med*. 2013;19(5):631–635. doi:10.1038/nm.3017.

113. Cypess AM, White AP, Vernochet C, et al. Anatomical localization, gene expression profiling and functional characterization of adult human neck brown fat. *Nat Med*. 2013;19(5):635–640. doi:10.1038/nm.3112.

114. Nedergaard J, Cannon B. How brown is brown fat? It depends where you look. *Nat Med*. 2013;19(5):540–1. doi:10.1038/nm.3187.

115. Cypess AM, Chen Y, Sze C, et al. Cold but not sympathomimetics activates human brown adipose tissue in vivo. *Proc Natl Acad Sci U S A*. 2012;109(25):10001–5. doi:10.1073/pnas.1207911109.

116. Muzik O, Mangner TJ, Granneman JG. Assessment of oxidative metabolism in brown fat using PET imaging. *Front Endocrinol (Lausanne)*. 2012;3(FEB):1–7. doi:10.3389/fendo.2012.00015.

117. Yoneshiro T, Aita S, Kawai Y, Iwanaga T, Saito M. Nonpungent capsaicin analogs (capsinoids) increase energy expenditure through the activation of brown adipose tissue in humans. *Am J Clin Nutr*. 2012;95(4):845–50. doi:10.3945/ajcn.111.018606.

118. Yoneshiro T, Aita S, Matsushita M, et al. Brown adipose tissue, whole-body energy expenditure, and thermogenesis in healthy adult men. *Obesity (Silver Spring)*. 2011;19(1):13–6. doi:10.1038/oby.2010.105.

119. Silva JE. Thermogenic mechanisms and their hormonal regulation. *Physiol Rev*. 2006;86(2):435–464. doi:10.1152/physrev.00009.2005.

120. Celi FS, Le TN, Ni B. Physiology and relevance of human adaptive thermogenesis response. *Trends Endocrinol Metab*. 2015;26(5):238–47. doi:10.1016/j.tem.2015.03.003.

121. Ma SW, Foster DO. Uptake of glucose and release of fatty acids and glycerol by rat brown adipose tissue in vivo. *Can J Physiol Pharmacol*. 1986;64(5):609–14.

122. Hill JO. Understanding and addressing the epidemic of obesity: An energy balance

perspective. *Endocr Rev*. 2006;27(7):750–761. doi:10.1210/er.2006-0032.

123. Swinburn B a, Jolley D, Kremer PJ, Salbe AD, Ravussin E. Estimating the effects of energy imbalance on changes in body weight in children. *Am J Clin Nutr*. 2006;83(4):859–863.

124. Cypess AM, Haft CR, Laughlin MR, Hu HH. Brown fat in humans: consensus points and experimental guidelines. *Cell Metab*. 2014;20(3):408–415. doi:10.1016/j.cmet.2014.07.025.

125. Ido T, Wan C-N, Casella V, et al. Labeled 2-deoxy-D-glucose analogs. 18F-labeled 2-deoxy-2-fluoro-D-glucose, 2-deoxy-2-fluoro-D-mannose and 14C-2-deoxy-2-fluoro-D-glucose. *J Label Compd Radiopharm*. 1978;14(2):175–183. doi:10.1002/jlcr.2580140204.

126. Jadvar H, Parker JA. *Clinical PET and PET/CT*. London: Springer-Verlag; 2005. doi:10.1007/b138777.

127. Kinahan PE, Fletcher JW. Positron emission tomography-computed tomography standardized uptake values in clinical practice and assessing response to therapy. *Semin Ultrasound, CT MRI*. 2010;31(6):496–505. doi:10.1053/j.sult.2010.10.001.

128. Kumar V, Nath K, Berman CG, et al. Variance of SUVs for FDG-PET/CT is greater in clinical practice than under ideal study settings. *Clin Nucl Med*. 2013;38(3):175–82. doi:10.1097/RLU.0b013e318279ffdf.

129. Heusch P, Buchbender C, Beiderwellen K, et al. Standardized uptake values for [^{18}F] FDG in normal organ tissues: comparison of whole-body PET/CT and PET/MRI. *Eur J Radiol*. 2013;82(5):870–6. doi:10.1016/j.ejrad.2013.01.008.

130. Kapoor V, McCook BM, Torok FS. An introduction to PET-CT imaging. *Radiographics*. 2004;24(2):523–543. doi:10.1148/rg.242025724.

131. Goldman LW. Principles of CT and CT technology. *J Nucl Med Technol*. 2007;35(3):115–28; quiz 129–30. doi:10.2967/jnmt.107.042978.

132. Muzik O, Mangner TJ, Leonard WR, Kumar A, Janisse J, Granneman JG. 15O PET Measurement of Blood Flow and Oxygen Consumption in Cold-Activated Human Brown Fat. *J Nucl Med*. 2013;54(4):523–31. doi:10.2967/jnumed.112.111336.

133. Baron DM, Clerte M, Brouckaert P, et al. In vivo noninvasive characterization of brown adipose tissue blood flow by contrast ultrasound in mice. *Circ Cardiovasc Imaging*. 2012;5(5):652–659. doi:10.1161/CIRCIMAGING.112.975607.

134. Osculati F, Leclercq F, Sbarbati A, Zancanaro C, Cinti S, Antonakis K. Morphological identification of brown adipose tissue by magnetic resonance imaging in the rat. *Eur J Radiol*. 1989;9(2):112–4.

135. Osculati F, Sbarbati A, Leclercq F, et al. The correlation between magnetic resonance imaging and ultrastructural patterns of brown adipose tissue. *J Submicrosc Cytol Pathol*. 1991;23(1):167–74.

136. Sbarbati a, Baldassarri a M, Zancanaro C, Boicelli A, Osculati F. In vivo morphometry and functional morphology of brown adipose tissue by magnetic resonance imaging. *Anat*

Rec. 1991;231(3):293–7. doi:10.1002/ar.1092310302.

137. Sbarbati a, Guerrini U, Marzola P, Asperio R, Osculati F. Chemical shift imaging at 4.7 tesla of brown adipose tissue. *J Lipid Res*. 1997;38(2):343–7.

138. Dixon WT. Simple proton spectroscopic imaging. *Radiology*. 1984;153(1):189–194. doi:10.1148/radiology.153.1.6089263.

139. Kim YS, Mun CW, Cho ZH. Chemical-shift imaging with large magnetic field inhomogeneity. *Magn Reson Med*. 1987;4(5):452–460.

140. Yeung HN, Kormos DW. Separation of true fat and water images by correcting magnetic field inhomogeneity in situ. *Radiology*. 1986;159(3):783–786. doi:10.1148/radiology.159.3.3704157.

141. Meisamy S, Hines CDG, Hamilton G, et al. Quantification of hepatic steatosis with T1-independent, T2-corrected MR imaging with spectral modeling of fat: blinded comparison with MR spectroscopy. *Radiology*. 2011;258(3):767–75. doi:10.1148/radiol.10100708.

142. Tsao J, Samsonov A, Hu HH, et al. 2012 ISMRM challenge on water-fat reconstruction judging. *Int Soc Magn Reson Med*. 2012. Available at: http://www.ismrm.org/challenge/node/17 Archived by WebCite at http://www.webcitation.org/6bxPUKgNR. Accessed October 1, 2015.

143. Welch EB, Smith DS, Avison MJ, Berglund J, Kullberg J, Ahlström H. 2012 ISMRM challenge on water-fat reconstruction final team standings. *Int Soc Magn Reson Med*. 2012. Available at: http://www.ismrm.org/challenge/node/18 Archived by WebCite at http://www.webcitation.org/6bxOBP0Ql. Accessed October 1, 2015.

144. Hamilton G, Yokoo T, Bydder M, et al. In vivo characterization of the liver fat ^{1}H MR spectrum. *NMR Biomed*. 2011;24(7):784–90. doi:10.1002/nbm.1622.

145. Liu C-Y, McKenzie C a, Yu H, Brittain JH, Reeder SB. Fat quantification with IDEAL gradient echo imaging: correction of bias from T(1) and noise. *Magn Reson Med*. 2007;58(2):354–64. doi:10.1002/mrm.21301.

146. Buxton RB, Wismer GL, Brady TJ, Rosen BR. Quantitative proton chemical-shift imaging. *Magn Reson Med*. 1986;3(6):881–900. doi:10.1016/0022-2364(88)90041-8.

147. Hu HH, Smith DL, Nayak KS, Goran MI, Nagy TR. Identification of brown adipose tissue in mice with fat-water IDEAL-MRI. *J Magn Reson Imaging*. 2010;31(5):1195–202. doi:10.1002/jmri.22162.

148. Hu HH, Perkins TG, Chia JM, Gilsanz V. Characterization of human brown adipose tissue by chemical-shift water-fat MRI. *AJR Am J Roentgenol*. 2013;200(1):177–83. doi:10.2214/AJR.12.8996.

149. Foster DO, Frydman ML. Tissue distribution of cold-induced thermogenesis in conscious warm- or cold-acclimated rats reevaluated from changes in tissue blood flow: the dominant role of brown adipose tissue in the replacement of shivering by nonshivering thermogenesis. *Can J Physiol Pharmacol*. 1979;57(3):257–70.

150. Ordidge RJ, Gorell JM, Deniau JC, Knight RA, Helpern JA. Assessment of relative brain

iron concentrations using T2-weighted and T2*-weighted MRI at 3 Tesla. *Magn Reson Med*. 1994;32(3):335–341. doi:10.1002/mrm.1910320309.

151. Ledermann H-P, Schulte A-C, Heidecker H-G, et al. Blood oxygenation level-dependent magnetic resonance imaging of the skeletal muscle in patients with peripheral arterial occlusive disease. *Circulation*. 2006;113(25):2929–2935. doi:10.1161/CIRCULATIONAHA.105.605717.

152. Khanna A, Branca RT. Detecting brown adipose tissue activity with BOLD MRI in mice. *Magn Reson Med*. 2012;68(4):1285–90. doi:10.1002/mrm.24118.

153. Wood JC, Enriquez C, Ghugre N, et al. MRI R2 and R2* mapping accurately estimates hepatic iron concentration in transfusion-dependent thalassemia and sickle cell disease patients. *Blood*. 2005;106(4):1460–1465. doi:10.1182/blood-2004-10-3982.

154. Khalil M, Enzinger C, Langkammer C, et al. Quantitative assessment of brain iron by R(2)* relaxometry in patients with clinically isolated syndrome and relapsing-remitting multiple sclerosis. *Mult Scler*. 2009;15(9):1048–54. doi:10.1177/1352458509106609.

155. Aschermann Z, Perlaki G, Orsi G, et al. Quantitative assessment of brain iron by R2* relaxometry in patients with cervical dystonia. *Mov Disord*. 2015;30(10):1422–6. doi:10.1002/mds.26306.

156. Hu HH, Yin L, Aggabao PC, Perkins TG, Chia JM, Gilsanz V. Comparison of brown and white adipose tissues in infants and children with chemical-shift-encoded water-fat MRI. *J Magn Reson Imaging*. 2013;38(4):885–96. doi:10.1002/jmri.24053.

157. Cypess AM, Lehman S, Williams G, et al. Identification and importance of brown adipose tissue in adult humans. *N Engl J Med*. 2009;360(15):1509–1517. doi:10.1097/OGX.0b013e3181ac8aa2.

158. Ouellet V, Routhier-Labadie A, Bellemare W, et al. Outdoor temperature, age, sex, body mass index, and diabetic status determine the prevalence, mass, and glucose-uptake activity of 18F-FDG-detected BAT in humans. *J Clin Endocrinol Metab*. 2011;96(1):192–9. doi:10.1210/jc.2010-0989.

159. Wei H, Chiba S, Moriwaki C, et al. A Clinical Approach to Brown Adipose Tissue in the Para-Aortic Area of the Human Thorax. *PLoS One*. 2015;10(4):e0122594. doi:10.1371/journal.pone.0122594.

160. Nirengi S, Yoneshiro T, Sugie H, Saito M, Hamaoka T. Human brown adipose tissue assessed by simple, noninvasive near-infrared time-resolved spectroscopy. *Obesity (Silver Spring)*. 2015;23(5):973–80. doi:10.1002/oby.21012.

161. Bligh J, Johnson KG. Glossary of terms for thermal physiology. *J Appl Physiol*. 1973;35(6):941–961. doi:10.1016/S0306-4565(02)00055-4.

162. Hernando D, Hines CDG, Yu H, Reeder SB. Addressing phase errors in fat-water imaging using a mixed magnitude/complex fitting method. *Magn Reson Med*. 2012;67(3):638–44. doi:10.1002/mrm.23044.

163. Berglund J, Kullberg J. Three-dimensional water/fat separation and T 2 * estimation based on whole-image optimization-Application in breathhold liver imaging at 1.5 T. *Magn*

Reson Med. 2012;67(6):1684–1693. doi:10.1002/mrm.23185.

164. Yu H, Shimakawa A, Hines CDG, et al. Combination of complex-based and magnitude-based multiecho water-fat separation for accurate quantification of fat-fraction. *Magn Reson Med*. 2011;66(1):199–206. doi:10.1002/mrm.22840.

165. Middleton MS, Hamilton G, Bydder M, Sirlin CB. How Much Fat is Under the Water Peak in Liver Fat MR Spectroscopy? In: *17th annual meeting of ISMRM, Honolulu, Hawaii*.; 2009:4331.

166. Hernando D, Kramer JH, Reeder SB. Multipeak fat-corrected complex R2* relaxometry: Theory, optimization, and clinical validation. *Magn Reson Med*. 2013;70(5):1319–1331. doi:10.1002/mrm.24593.

167. Maes F, Collignon a, Vandermeulen D, Marchal G, Suetens P. Multimodality image registration by maximization of mutual information. *IEEE Trans Med Imaging*. 1997;16(2):187–98. doi:10.1109/42.563664.

168. Eckel RH, Alberti KGMM, Grundy SM, Zimmet PZ. The metabolic syndrome. *Lancet*. 2010;375(9710):181–3. doi:10.1016/S0140-6736(09)61794-3.

169. Wang H, Chen YE, Eitzman DT. Imaging body fat: techniques and cardiometabolic implications. *Arterioscler Thromb Vasc Biol*. 2014;34(10):2217–23. doi:10.1161/ATVBAHA.114.303036.

170. Baba S, Jacene H a, Engles JM, Honda H, Wahl RL. CT Hounsfield units of brown adipose tissue increase with activation: preclinical and clinical studies. *J Nucl Med*. 2010;51(2):246–50. doi:10.2967/jnumed.109.068775.

171. McEvoy FJ, Madsen MT, Strathe AB, Svalastoga E. Hounsfield Unit dynamics of adipose tissue and non-adipose soft tissues in growing pigs. *Res Vet Sci*. 2008;84(2):300–4. doi:10.1016/j.rvsc.2007.05.005.

172. Bydder M, Yokoo T, Hamilton G, et al. Relaxation effects in the quantification of fat using gradient echo imaging. *Magn Reson Imaging*. 2008;26(3):347–59. doi:10.1016/j.mri.2007.08.012.

173. Bydder M, Yokoo T, Yu H, Carl M, Reeder SB, Sirlin CB. Constraining the initial phase in water-fat separation. *Magn Reson Imaging*. 2011;29(2):216–21. doi:10.1016/j.mri.2010.08.011.

174. Brodsky EK, Holmes JH, Yu H, Reeder SB. Generalized k-space decomposition with chemical shift correction for non-Cartesian water-fat imaging. *Magn Reson Med*. 2008;59(5):1151–64. doi:10.1002/mrm.21580.

175. Yu H, Shimakawa A, McKenzie C a, Brodsky E, Brittain JH, Reeder SB. Multiecho water-fat separation and simultaneous R2* estimation with multifrequency fat spectrum modeling. *Magn Reson Med*. 2008;60(5):1122–34. doi:10.1002/mrm.21737.

176. Grauer WO, Moss AA, Cann CE, Goldberg HI. Quantification of body fat distribution in the abdomen using computed tomography. *Am J Clin Nutr*. 1984;39(4):631–7.

177. Kvist H, Chowdhury B, Grangård U, Tylén U, Sjöström L. Total and visceral adipose-

tissue volumes derived from measurements with computed tomography in adult men and women: predictive equations. *Am J Clin Nutr*. 1988;48(6):1351–61.

178. Maurovich-Horvat P, Massaro J, Fox CS, Moselewski F, O'Donnell CJ, Hoffmann U. Comparison of anthropometric, area- and volume-based assessment of abdominal subcutaneous and visceral adipose tissue volumes using multi-detector computed tomography. *Int J Obes (Lond)*. 2007;31:500–506. doi:10.1038/sj.ijo.0803454.

179. Smith SR, Lovejoy JC, Greenway F, et al. Contributions of total body fat, abdominal subcutaneous adipose tissue compartments, and visceral adipose tissue to the metabolic complications of obesity. *Metabolism*. 2001;50:425–435. doi:10.1053/meta.2001.21693.

180. Lee K, Lee S, Kim YJ, Kim YJ. Waist circumference, dual-energy X-ray absortiometrically measured abdominal adiposity, and computed tomographically derived intra-abdominal fat area on detecting metabolic risk factors in obese women. *Nutrition*. 2008;24:625–631. doi:10.1016/j.nut.2008.03.004.

181. Park BJ, Kim YJ, Kim DH, et al. Visceral adipose tissue area is an independent risk factor for hepatic steatosis. *J Gastroenterol Hepatol*. 2008;23:900–907. doi:10.1111/j.1440-1746.2007.05212.x.

182. Sarin S, Wenger C, Marwaha A, et al. Clinical Significance of Epicardial Fat Measured Using Cardiac Multislice Computed Tomography. *Am J Cardiol*. 2008;102:767–771. doi:10.1016/j.amjcard.2008.04.058.

183. Rosenquist KJ, Pedley A, Massaro JM, et al. Visceral and subcutaneous fat quality and cardiometabolic risk. *JACC Cardiovasc Imaging*. 2013;6(7):762–771. doi:10.1016/j.jcmg.2012.11.021.

184. Alvey NJ, Pedley A, Rosenquist KJ, et al. Association of Fat Density With Subclinical Atherosclerosis. *J Am Heart Assoc*. 2014;3(4). doi:10.1161/JAHA.114.000788.

185. Reeder SB, Sirlin CB. Quantification of liver fat with magnetic resonance imaging. *Magn Reson Imaging Clin N Am*. 2010;18(3):337–57, ix. doi:10.1016/j.mric.2010.08.013.

186. Bydder M, Shiehmorteza M, Yokoo T, et al. Assessment of liver fat quantification in the presence of iron. *Magn Reson Imaging*. 2010;28(6):767–76. doi:10.1016/j.mri.2010.03.017.

187. Seidell JC, Bakker CJ, van der Kooy K. Imaging techniques for measuring adipose-tissue distribution--a comparison between computed tomography and 1.5-T magnetic resonance. *Am J Clin Nutr*. 1990;51(6):953–7.

188. Kullberg J, Brandberg J, Angelhed JE, et al. Whole-body adipose tissue analysis: Comparison of MRI, CT and dual energy X-ray absorptiometry. *Br J Radiol*. 2009;82(February):123–130. doi:10.1259/bjr/80083156.

189. Yoshizumi T, Nakamura T, Yamane M, et al. Abdominal fat: standardized technique for measurement at CT. *Radiology*. 1999;211(1):283–6. doi:10.1148/radiology.211.1.r99ap15283.

190. Gifford A, Towse TF, Walker RC, Avison MJ, Welch EB. Human brown adipose tissue depots automatically segmented by positron emission tomography/computed tomography

and registered magnetic resonance images. *J Vis Exp*. 2015;(96):e52415. doi:10.3791/52415.

191. Kim S, Lee GH, Lee S, Park SH, Pyo HB, Cho JS. Body fat measurement in computed tomography image. *Biomed Sci Instrum*. 1999;35:303–8.

192. Hu HH, Hines CDG, Smith DL, Reeder SB. Variations in T(2)* and fat content of murine brown and white adipose tissues by chemical-shift MRI. *Magn Reson Imaging*. 2012;30(3):323–9. doi:10.1016/j.mri.2011.12.004.

193. Aubrey J, Esfandiari N, Baracos VE, et al. Measurement of skeletal muscle radiation attenuation and basis of its biological variation. *Acta Physiol*. 2014;210(3):489–497. doi:10.1111/apha.12224.

194. Wijers SLJ, Saris WHM, van Marken Lichtenbelt WD. Cold-induced adaptive thermogenesis in lean and obese. *Obesity (Silver Spring)*. 2010;18(6):1092–1099. doi:10.1038/oby.2010.74.

195. Kern P a, Finlin BS, Zhu B, et al. The effects of temperature and seasons on subcutaneous white adipose tissue in humans: evidence for thermogenic gene induction. *J Clin Endocrinol Metab*. 2014;99(12):E2772–9. doi:10.1210/jc.2014-2440.

196. Weyer C, Foley JE, Bogardus C, Tataranni P a., Pratley RE. Enlarged subcutaneous abdominal adipocyte size, but not obesity itself, predicts type II diabetes independent of insulin resistance. *Diabetologia*. 2000;43(12):1498–1506. doi:10.1007/s001250051560.

197. Hames KC, Koutsari C, Santosa S, Bush NC, Jensen MD. Adipose tissue fatty acid storage factors: effects of depot, sex and fat cell size. *Int J Obes (Lond)*. 2015;39(6):884–7. doi:10.1038/ijo.2015.10.

198. Spalding KL, Arner E, Westermark PO, et al. Dynamics of fat cell turnover in humans. *Nature*. 2008;453(7196):783–787. doi:10.1097/01.ogx.0000325910.81966.ac.

199. Gunawardana SC, Piston DW. Reversal of type 1 diabetes in mice by brown adipose tissue transplant. *Diabetes*. 2012;61(3):674–82. doi:10.2337/db11-0510.

200. Sacks H, Symonds ME. Anatomical locations of human brown adipose tissue: functional relevance and implications in obesity and type 2 diabetes. *Diabetes*. 2013;62(6):1783–90. doi:10.2337/db12-1430.

201. Frühbeck G, Becerril S, Sáinz N, Garrastachu P, García-Velloso MJ. BAT: a new target for human obesity? *Trends Pharmacol Sci*. 2009;30(8):387–96. doi:10.1016/j.tips.2009.05.003.

202. Yoneshiro T, Saito M. Activation and recruitment of brown adipose tissue as anti-obesity regimens in humans. *Ann Med*. 2014;(March):1–9. doi:10.3109/07853890.2014.911595.

203. Chen Y-CI, Cypess AM, Chen Y-C, et al. Measurement of human brown adipose tissue volume and activity using anatomic MR imaging and functional MR imaging. *J Nucl Med*. 2013;54(9):1584–7. doi:10.2967/jnumed.112.117275.

204. Rasmussen JM, Entringer S, Nguyen A, et al. Brown adipose tissue quantification in human neonates using water-fat separated MRI. *PLoS One*. 2013;8(10).

doi:10.1371/journal.pone.0077907.

205. van Rooijen BD, van der Lans AAJJ, Brans B, et al. Imaging Cold-Activated Brown Adipose Tissue Using Dynamic T2*-Weighted Magnetic Resonance Imaging and 2-Deoxy-2-[18F]fluoro-D-glucose Positron Emission Tomography. *Invest Radiol*. 2013;48(10):1–7. doi:10.1097/RLI.0b013e31829363b8.

206. Reddy NL, Jones T a, Wayte SC, et al. Identification of brown adipose tissue using MR imaging in a human adult with histological and immunohistochemical confirmation. *J Clin Endocrinol Metab*. 2014;99(1):E117–21. doi:10.1210/jc.2013-2036.

207. Borga M, Virtanen K a, Romu T, et al. Brown Adipose Tissue in Humans. In: *Methods in Enzymology*.Vol 537.; 2014:141–159. doi:10.1016/B978-0-12-411619-1.00008-2.

208. Huttunen P, Hirvonen J, Kinnula V. The occurrence of brown adipose tissue in outdoor workers. *Eur J Appl Physiol Occup Physiol*. 1981;46(4):339–345. doi:10.1007/BF00422121.

209. Hu HH, Chung S a, Nayak KS, Jackson H a, Gilsanz V. Differential computed tomographic attenuation of metabolically active and inactive adipose tissues: preliminary findings. *J Comput Assist Tomogr*. 2011;35(1):65–71. doi:10.1097/RCT.0b013e3181fc2150.

210. Lundström E, Strand R, Johansson L, Bergsten P, Ahlström H, Kullberg J. Magnetic Resonance Imaging Cooling-Reheating Protocol Indicates Decreased Fat Fraction via Lipid Consumption in Suspected Brown Adipose Tissue. *PLoS One*. 2015;10(4):e0126705. doi:10.1371/journal.pone.0126705.

211. Hamilton G, Smith DL, Bydder M, Nayak KS, Hu HH. MR properties of brown and white adipose tissues. *J Magn Reson Imaging*. 2011;34(2):468–473. doi:10.1002/jmri.22623.

212. Leporq B, Lambert S a, Ronot M, Vilgrain V, VanBeers BE. Quantification of the triglyceride fatty acid composition with 3.0 T MRI. *NMR Biomed*. 2014;27(10):1211–1221. doi:10.1002/nbm.3175.

213. Chen YI, Cypess AM, Sass C a., et al. Anatomical and Functional Assessment of Brown Adipose Tissue by Magnetic Resonance Imaging. *Obesity*. 2012;20(7):1519–1526. doi:10.1038/oby.2012.22.

214. Vijgen GHEJ, Bouvy ND, Teule GJJ, Brans B, Schrauwen P, van Marken Lichtenbelt WD. Brown adipose tissue in morbidly obese subjects. *PLoS One*. 2011;6(2):e17247. doi:10.1371/journal.pone.0017247.

215. Breiman L. Random forests. *Mach Learn*. 2001:5–32. doi:10.1023/A:1010933404324.

216. Field CJ, Angel a, Clandinin MT. Relationship of diet to the fatt acid composition of human adipose tissue structural and stored lipids. *Am J Clin Nutr*. 1985;42(December):1206–1220.

217. Lin DS, Connor WE, Spenler CW. Are dietary saturated, monounsaturated, and polyunsaturated fatty acids deposited to the same extent in adipose tissue of rabbits? *Am J Clin Nutr*. 1993;58(2):174–179.

218. Sadurskis A, Dicker A, Cannon B, Nedergaard J. Polyunsaturated fatty acids recruit brown adipose tissue: increased UCP content and NST capacity. *Am J Physiol*. 1995;269(2 Pt 1):E351–E360.

219. Raclot T, Groscolas R, Leray C. Composition and structure of triacylglycerols in brown adipose tissue of rats fed fish oil. *Lipids*. 1994;29(11):759–764. doi:10.1007/BF02536697.

220. Avram MM, Avram AS, James WD. Subcutaneous fat in normal and diseased states 3. Adipogenesis: from stem cell to fat cell. *J Am Acad Dermatol*. 2007;56(3):472–92. doi:10.1016/j.jaad.2006.06.022.

221. Zancanaro C, Nano R, Marchioro C, Sbarbati A, Boicelli A, Osculati F. Magnetic resonance spectroscopy investigations of brown adipose tissue and isolated brown adipocytes. *J Lipid Res*. 1994;35(12):2191–9.

222. Bydder M, Girard O, Hamilton G. Mapping the double bonds in triglycerides. *Magn Reson Imaging*. 2011;29(8):1041–6. doi:10.1016/j.mri.2011.07.004.

223. Berglund J, Ahlström H, Kullberg J. Model-based mapping of fat unsaturation and chain length by chemical shift imaging-phantom validation and in vivo feasibility. *Magn Reson Med*. 2012;68(6):1815–1827. doi:10.1002/mrm.24196.

224. Hernando D. FAT-WATER TOOLBOX: CODE. *ISMRM Fat-Water Sep Work*. Available at: URL:http://ismrm.org/workshops/FatWater12/data.htm. (Archived by WebCite® at http://www.webcitation.org/6cIgt4twD). Accessed October 15, 2015.

225. Soher BJ, Wyatt C, Reeder SB, MacFall JR. Noninvasive temperature mapping with MRI using chemical shift water-fat separation. *Magn Reson Med*. 2010;63(5):1238–46. doi:10.1002/mrm.22310.

226. Sprinkhuizen SM, Bakker CJG, Bartels LW. Absolute MR thermometry using time-domain analysis of multi-gradient-echo magnitude images. *Magn Reson Med*. 2010;64(1):239–48. doi:10.1002/mrm.22429.

227. Pan X, Li C, Ying K, Weng D, Qin W, Li K. Model-based PRFS thermometry using fat as the internal reference and the extended Prony algorithm for model fitting. *Magn Reson Imaging*. 2010;28(3):418–26. doi:10.1016/j.mri.2009.11.002.

228. Jenista ER, Branca RT, Warren WS. Absolute temperature imaging using intermolecular multiple quantum MRI. *Int J Hyperthermia*. 2010;26(7):725–34. doi:10.3109/02656736.2010.499527.

229. Branca RT, He T, Zhang L, et al. Detection of brown adipose tissue and thermogenic activity in mice by hyperpolarized xenon MRI. *Proc Natl Acad Sci U S A*. 2014;111(50):18001–6. doi:10.1073/pnas.1403697111.

230. Osawa K, Miyoshi T, Yamauchi K, et al. Nonalcoholic Hepatic Steatosis Is a Strong Predictor of High-Risk Coronary-Artery Plaques as Determined by Multidetector CT. *PLoS One*. 2015;10(6):e0131138. doi:10.1371/journal.pone.0131138.

231. Goutelle S, Maurin M, Rougier F, et al. The Hill equation: a review of its capabilities in pharmacological modelling. *Fundam Clin Pharmacol*. 2008;22(6):633–48. doi:10.1111/j.1472-8206.2008.00633.x.

232. Federau C, O'Brien K, Meuli R, Hagmann P, Maeder P. Measuring brain perfusion with intravoxel incoherent motion (IVIM): Initial clinical experience. *J Magn Reson Imaging*. 2014;39(3):624–632. doi:10.1002/jmri.24195.

233. Rossi C, Artunc F, Martirosian P, Schlemmer H-P, Schick F, Boss A. Histogram analysis of renal arterial spin labeling perfusion data reveals differences between volunteers and patients with mild chronic kidney disease. *Invest Radiol*. 2012;47(8):490–6. doi:10.1097/RLI.0b013e318257063a.

234. Hartkamp NS, Petersen ET, De Vis JB, Bokkers RPH, Hendrikse J. Mapping of cerebral perfusion territories using territorial arterial spin labeling: techniques and clinical application. *NMR Biomed*. 2012;(March):n/a–n/a. doi:10.1002/nbm.2836.

235. Lau a Z, Chen a P, Gu Y, Ladouceur-Wodzak M, Nayak KS, Cunningham CH. Noninvasive identification and assessment of functional brown adipose tissue in rodents using hyperpolarized (13)C imaging. *Int J Obes*. 2014;38(1):126–31. doi:10.1038/ijo.2013.58.

236. Branca RT, Warren WS. In vivo brown adipose tissue detection and characterization using water-lipid intermolecular zero-quantum coherences. *Magn Reson Med*. 2011;65(2):313–9. doi:10.1002/mrm.22622.

237. Branca RT, Zhang L, Warren WS, et al. In vivo noninvasive detection of Brown Adipose Tissue through intermolecular zero-quantum MRI. *PLoS One*. 2013;8(9):e74206. doi:10.1371/journal.pone.0074206.

238. Gifford A, Berglund J, Kullberg J, Towse TF, Avison MJ, Welch EB. T1 and Fat-Water Fraction Measurements in an Adult Human: Possible Markers for Brown Adipose Tissue? In: *Proceedings of the International Society for Magnetic Resonance in Medicine: Workshop on Fat-Water Separation*.; 2012:1:13.

239. Madar I, Ravert HT, Du Y, et al. Characterization of uptake of the new PET imaging compound 18F-fluorobenzyl triphenyl phosphonium in dog myocardium. *J Nucl Med*. 2006;47(8):1359–1366. doi:47/8/1359 [pii].

240. Hadi M, Chen CC, Whatley M, Pacak K, Carrasquillo J a. Brown fat imaging with (18)F-6-fluorodopamine PET/CT, (18)F-FDG PET/CT, and (123)I-MIBG SPECT: a study of patients being evaluated for pheochromocytoma. *J Nucl Med*. 2007;48(7):1077–1083. doi:10.2967/jnumed.106.035915.

241. Bauwens M, Wierts R, Van Royen B, et al. Molecular imaging of brown adipose tissue in health and disease. *Eur J Nucl Med Mol Imaging*. 2014;41(4):776–791. doi:10.1007/s00259-013-2611-8.

242. Mori H, Isobe S, Sakai S, et al. Microvascular obstruction on delayed enhancement cardiac magnetic resonance imaging after acute myocardial infarction, compared with myocardial 201Tl and 123I-BMIPP dual SPECT findings. *Eur J Radiol*. 2015;84(8):1516–1524. doi:10.1016/j.ejrad.2015.05.002.

243. Goetze S, Lavely WC, Ziessman H a, Wahl RL. Visualization of brown adipose tissue with 99mTc-methoxyisobutylisonitrile on SPECT/CT. *J Nucl Med*. 2008;49(5):752–756. doi:10.2967/jnumed.107.048074.

244. Fukuchi K, Ono Y, Nakahata Y, Okada Y, Hayashida K, Ishida Y. Visualization of interscapular brown adipose tissue using (99m)Tc-tetrofosmin in pediatric patients. *J Nucl Med*. 2003;44(10):1582–1585.

245. Clerte M, Baron DM, Brouckaert P, et al. Brown adipose tissue blood flow and mass in obesity: a contrast ultrasound study in mice. *J Am Soc Echocardiogr*. 2013;26(12):1465–73. doi:10.1016/j.echo.2013.07.015.

246. Nightingale K, Soo MS, Nightingale R, et al. Acoustic radiation force impulse imaging: remote palpation of the mechanical properties of tissue. In: *2002 IEEE Ultrasonics Symposium, 2002. Proceedings.*Vol 2. IEEE; :1821–1830. doi:10.1109/ULTSYM.2002.1192652.

247. Goddi A, Bonardi M, Alessi S. Breast elastography: A literature review. *J Ultrasound*. 2012;15(3):192–198. doi:10.1016/j.jus.2012.06.009.

248. Abdennour M, Reggio S, Le Naour G, et al. Association of adipose tissue and liver fibrosis with tissue stiffness in morbid obesity: links with diabetes and BMI loss after gastric bypass. *J Clin Endocrinol Metab*. 2014;99(3):898–907. doi:10.1210/jc.2013-3253.

249. Sasso M, Abdennour M, Liu Y, et al. Relevance of Adipose Tissue Stiffness Evaluated by Transient Elastography (AdipoScan^{TM}) in Morbidly Obese Patients before Bariatric Surgery. *Phys Procedia*. 2015;70:1264–1268. doi:10.1016/j.phpro.2015.08.281.

250. Stauffer PR, Rodrigues D, Salahi S, et al. Stable Microwave Radiometry System for Long Term Monitoring of Deep Tissue Temperature. *Proc SPIE*. 2013;8584(6):1–11. doi:10.1117/12.2003976.

251. Rodrigues D, Maccarini PF, Salahi S, et al. Numerical 3D modeling of heat transfer in human tissues for microwave radiometry monitoring of brown fat metabolism. *Proc SPIE*. 2013;8584(6):1–12. doi:10.1117/12.2004931.